Elastic and Viscous Anisotropy in Earth's mantle – Observations and Implications

by

Einat Lev

Submitted to the Department of Earth, Atmospheric and Planetary Science
in partial fulfillment of the requirements for the degree of

Doctor of Philosophy

at the

MASSACHUSETTS INSTITUTE OF TECHNOLOGY

June 2009

Author .....
Department of Earth, Atmospheric and Planetary Science
May 18, 2009

Certified by .....
Bradford H. Hager
Ida and Cecil Green Professor of Earth Sciences
Thesis Supervisor

Accepted by .....
Maria T. Zuber
E.A. Griswold Professor of Geophysics
Head, Department of Earth, Atmospheric and Planetary Sciences

Elastic and Viscous Anisotropy in Earth's mantle – Observations and Implications

by

Einat Lev

Submitted to the Department of Earth, Atmospheric and Planetary Science
on May 18, 2009, in partial fulfillment of the
requirements for the degree of
Doctor of Philosophy

Abstract

In this thesis I address the topic of anisotropy – the directional dependence of physical properties of rocks – from two complementary angles: I use seismic anisotropy to detect deformation in the mantle, and I demonstrate the importance of accounting for rheological anisotropy in mantle flow models.

The observations of seismic anisotropy in the Earth's interior allow geophysicists to probe the direction and mechanism of deformation, through the detection of lattice- and shape-preferred orientation and the derived elastic anisotropy. I capitalized upon this property when I investigated the deformation of the mantle underneath Eastern Tibet and compared it to the surface and crustal deformation. This work revealed an intriguing regional variation, hinting a change from north to south in the processes controlling the deformation of this complex region.

Preferred orientations in rocks can change the rheology and lead to anisotropy of viscosity, a property often ignored in geodynamical modeling. I included anisotropic viscosity in a number of test flow models, including a model of shear in the upper mantle due to plate motion, a model of buoyancy-driven instabilities, and a model of flow in the mantle wedge of subduction zones. My models revealed that anisotropic viscosity leads to substantial changes in all the flows I examined. In the upper mantle beneath a moving plate, anisotropic viscosity can lead to localization of the strain and the extend of power-law creep in the upper mantle. In the presence of anisotropic viscosity, the wavelength of density instabilities varies by the orientation of the anisotropy. The thermal structure and melt production of the subduction zone mantle wedge changes when anisotropic viscosity is accounted for. It is thus crucial that geodynamical flow models are self consistent and account for anisotropic viscosity.

Thesis Supervisor: Bradford H. Hager
Title: Ida and Cecil Green Professor of Earth Sciences

Acknowledgments

Some say it takes a village to raise a child. To make this thesis a reality, it took a lot more than a village. It took a department, a city, a family. I am grateful to them all, the many listed below, and the many more kept in my heart forever.

My advisor, Brad Hager, played the most significant role influencing my MIT experience. Brad – you are one of the smartest and kindest people I have ever met. By "smart" I don't refer only to your obvious scientific brilliance, but also to what a clever mentor you are – able to balance between allowing me to learn from my own mistakes and keeping me from straying too far. Your patience is unparalleled. I really appreciate your honesty and your willingness to discuss basically anything that was on my mind.

Rob van der Hilst, the chair of my thesis committee and supervisor of my second generals project, was just the perfect co-advisor. Rob – thank you so much for always having an open door for me to come and share the pains (and joys!) of grad school, for "adopting" me to your group, for sharing with me your experience in publishing, editing and general scientific behavior, and, of course, for convincing me to come here in the first place!

Stephane Rondenay and Lindy Elkins-Tanton, two other co-conspirators in bringing me to MIT six years ago, took on their two-fold roles as cheerleaders and emergency seismology/petrology consultants, very seriously. Stephane, Lindy – I met both of you when you were still post-docs at Brown. We have all gone a long way since, and I am so happy that our relationships go far beyond a student-committee member relation. You have both given me a helping hand and an ear when I needed. Thank you Stephane also for taking me out to dig holes in Cascadia – it was a great fun.

Last but not least member of my thesis committee is Greg Hirth. Greg – thank you for teaching me so much about rocks, for making rock rheology a real thing, more than an equation or the abstraction of a model. Your enthusiasm is contagious!

The software I used for the many numerical models included in this thesis was developed by Louis Moresi at Monash University and the excellent team of developers at VPAC. The folks down under – Alan Lo, Patrick Sunter, Steve Quenette, Julian Giordani – have been extremely helpful and responsive, always willing to help me out and solve technical

difficulties.

Many member of the EAPS faculty contributed to making my experience here so enjoyable. These include Tim Grove (generals committee member, paper co-author and an all-around melting advisor), Wiki Royden (Tibet inspiration), Clark Burchfiel (geology guru), Alison Malcolm (a living proof that things will be OK), and Bill Durham (in-house rheology consultant). A wonderful group of staff members supported my journey at EAPS: Roberta Allard, Jacqui Taylor, Vicki McKenna, Carol Sprague, Terri Macloon, and Beth MacEachran are all super-administrators who keep this place in order and in a good mood; Joe Hankins is probably the world's nicest librarian; Linda Meinke, Chris Hill, Greg Shomo and Scott Blomquist provided much needed IT services and cluster support. Thank you all!

It is common knowledge, however, that it is the graduate students upon which everything really stands. This is certainly true with respect to the grueling mission of bringing me and this thesis to the finish line. It would be impossible to list here all the students that helped me during my time here, but I'll try anyway: Maureen Long – a true friend and the one that got me into this whole "anisotropy" business to begin with; Christy Till – a beautiful person who was always there to listen and encourage and explain the solidus; Chin-wu Chen, James Dennedy-Frank and Erwan Mazarico (Go Team 521!) – devoted office-mates who shared this path with me since day 1, quietly suffering through sharing of an office with me and my "stuff."

As so many prospective students visiting our department heard me preach, the EAPS student body is what really makes it so special. Over the last 6 years, numerous EAPS students and ex-students took the time to offer me their knowledge, advice, and sometimes a shoulder to cry on. These include Kristen Cook, Emily van Ark, Eric Hetland, Brendan Meade, Clint Conrad, Krystle Catalli, Neil de la Plante, Jessica Warren, Chris Studinski-Ginzburg, Kate Ruhl, Taylor Schildgen, Alison Cohen, Jay Barr, Mike Krawczynski, Kyle Bradley, Will Ouimet, Nick Austin, Caroline Beghein, Jeremy Boyce, Ping Wang, Chang Li, Huajian Yao and Jiangning Lu. EAPS students – you rock!

My Cambridge friends Edya, Shay, Dana, Zachi and Yoel have always been there for me, from bike rides and gym workouts to lunch breaks and holiday gatherings. My Israel friends

Avigail, Ronnie, Roni, Uri, Ilan and Oran made me happy by sending beautiful photos from back home and reading my sometimes whiny emails. Rachel, Leslie and Tasha from Apple Valley Farm and Shan and Willy from Wadsworth Farm provided a peaceful haven where I could just forget and relax. My MentorNet mentors Lisa Rossbacher and Linda Stathoplos listened, answered many difficult questions, and loyally served as role models. Special thanks go to MIT's mental health service.

My family, while geographically far, have supported me infinitely along the way. The morning IM chats with my awesome sisters Idit and Galia were a great way to start the day with a smile. My mom's "Just finish this one chapter/project/paper, and then see if you still want to quit" proved critical in many occasions. My dad's voice of calm and reason, as well as grandma Ruth's weekly emails of family updates and political grunts, kept me on track. I greatly appreciate the support of my family-in-law – Etty, Shaul, Maya, Shani and Adi, and the home-away-from-home that family members living in Boston gave us.

I know it may sound a bit strange to thank a city, but I find that Cambridge, with its unique academic atmosphere, diverse and open-minded population, inspiring local cafés full of studious people with laptops, was simply the perfect environment for me to enter the world of scientific research. Leaving Cambridge is the hardest part of graduating.

The last person I wish to thank here is my husband Yossi, who simply cannot be put into any one category. All at once my best friend, a part of my family, and my very own debugger-on-call – Yossi, my love, I couldn't have done this without you. Thank you. Thank you tons. For everything. Hibuki!

Contents

1 Introduction **17**

2 Seismic Anisotropy in Eastern Tibet from Shear-Wave Splitting **21**

2.1 Abstract 21

2.2 Introduction 22

2.3 Data and Methods 25

2.3.1 The Cross-Correlation method 26

2.3.2 Multichannel method 26

2.4 Results 27

2.4.1 Splitting parameters for a single-layer model 27

2.4.2 Evidence for multiple layers of anisotropy? 28

2.5 Discussion 30

2.5.1 Arguments for an upper mantle source of the splitting signal 30

2.5.2 Anisotropy in Yunnan province and near the Red River Fault 31

2.5.3 Implications for lithosphere mechanics 32

2.6 Summary 33

2.7 Electronic supplement 34

2.8 Figures 34

3 Rayleigh-Taylor instabilities with anisotropic lithospheric viscosity **41**

3.1 Abstract 41

3.2 Introduction 42

3.3 Anisotropic viscosity and the wavelength of instabilities 44
3.3.1 Governing equations 45
3.3.2 Analytical solution 46
3.3.3 Numerical experiments 46
3.3.4 Results - a homogeneous but anisotropic upper layer 48
3.4 Laterally-varying anisotropy 50
3.4.1 Model setup 50
3.4.2 Results - a heterogeneous upper layer 50
3.5 Discussion 51
3.6 Summary 54
3.7 Appendix A: Derivation of analytical solution 56

4 Anisotropic viscosity changes the thermal structure of the mantle wedge at subduction zones 65
4.1 Abstract 65
4.2 Introduction 66
4.3 Modeling methodology 68
4.3.1 Model setup and solution 68
4.3.2 Calculation of melt production 69
4.3.3 Deformation mechanisms partitioning 71
4.4 Results and Discussion 71
4.5 Future directions 74
4.6 Summary 74
4.7 Acknowledgements 75

5 Influence of grain size and anisotropic viscosity on the development of an anisotropic layer in the upper mantle 83
5.1 Introduction 83
5.2 Methods 85
5.2.1 Model setup 85

5.2.2 Numerical tools . . . 87
5.2.3 Analysis of flow models output . . . 88
5.3 Results . . . 90
5.4 Discussion . . . 90
5.5 Conclusion . . . 92

6 Prediction of anisotropy from flow models – a comparison of three methods 97

6.1 abstract . . . 97
6.2 Introduction . . . 98
6.3 Methods . . . 99
6.3.1 Tracking of the finite strain ellipse . . . 100
6.3.2 FedRex, the Forward Evolution D-Rex . . . 101
6.3.3 Directors evolution . . . 102
6.4 Tests and Results . . . 103
6.4.1 Simple Shear . . . 104
6.4.2 Steady-state 1x1 “convection cell” . . . 104
6.4.3 Time-dependent layered-density instability . . . 105
6.5 Discussion . . . 106
6.5.1 Infinite Strain Axis vs. Directors . . . 106
6.5.2 Computation cost and availability of the methods . . . 107
6.5.3 Relating director orientations and olivine seismic anisotropy . . . 109
6.6 Summary . . . 111
6.7 Appendix – Codes used in this chapter . . . 111

List of Figures

2-1 Location of the seismic stations used in this study 35
2-2 Epicenters of events used in the study 36
2-3 Splitting measurements in eastern Tibet 37
2-4 Results for station MC04, MC08, and MC13 38
2-5 Correlation of fast polarization directions with surface features 39
2-6 Fast directions histograms for the North and South sub-regions 39

3-1 Analytical growth-rate curves for models with varying orientations and degrees of anisotropy 60
3-2 Growth-rate curves for models with varying orientations and degrees of anisotropy obtained from numerical experiments 61
3-3 Material distribution for models with horizontal and dipping initial fabric . 62
3-4 Laterally-varying anisotropy – model setup and initial conditions 62
3-5 Laterally-varying anisotropy – snapshots of resulting material distribution . . 63
3-1 Analytical growth-rate curves for a model with dipping anisotropy in both layers 64

4-1 Rayleigh-Taylor instabilities – model configuration 76
4-2 Comparing thermal quantities of isotropic and anisotropic models 77
4-3 Comparing the thermal field and melting regions of isotropic and anisotropic model 78
4-4 Strain rate and flow lines 79
4-5 Direction and strength of wedge LPO 80

4-6 Deformation mechanism boundary in the wedge 81

5-1 Viscosity profiles 93
5-2 Strain rate profiles for varying η_s/η_N 94
5-3 Thickness of layer of sufficient shear vs. grain size and viscosity ratio 94
5-4 SKS split times vs. grain size and viscosity ratio 95

6-1 The relationship between directors, olivine LPO and seismic anisotropy . . . 112
6-2 Schematic diagrams of the three flow fields tested 113
6-3 Results of the simple-shear test 114
6-4 Results of a convection cell test 115
6-5 Time-dependent particle paths in a "drip" model 115
6-6 Results for a steady-state Rayleigh-Taylor instability test 116
6-7 Time evolution of the anisotropy in a Rayleigh-Taylor instability model, using Directors 117
6-8 Execution time as a function of the number of directors 118
6-9 Execution time as a function of aggregates 119
6-10 Types of olivine LPO as a function of water content and stress and their relationship to Directors 120
6-11 The proportions of the symmetry components in the total anisotropy of a deformed aggregate in simple shear and drip tests 121

List of Tables

2.1 Preferred shear-wave splitting results for MIT array in eastern Tibet 34

5.1 Values of constants used in viscosity calculation 86

Chapter 1

Introduction

Geodynamics is a subfield of geophysics aimed at revealing and explaining the internal deformation processes shaping the solid Earth. Since we cannot make direct observations of the deformation taking place in Earth's interior, geophysicists are limited to using proxies and remote sensing techniques. One especially powerful family of tools is the observation of seismic anisotropy, or the direction-dependence of seismic wave velocities. These tools are capable of probing the deformation processes in the Earth's interior. In my PhD research, summarized in this thesis, I combined geodynamical modeling with seismic observations to investigate deformation processes in the Earth's upper mantle.

Anisotropy, the dependence of physical properties on the measuring direction, is often a direct outcome of the deformation of rocks. When rocks deform, they can develop a fabric, which results in the anisotropy of properties such as elasticity, viscosity and conductivity. This fabric records the history of deformation and can thus serve as a constraint for models of mantle flow and geodynamic evolution.

My initial investigation of anisotropy was through observations of seismic anisotropy in Eastern Tibet. I measured shear-wave splitting in a data set recorded by an array of seismometers deployed by MIT in Eastern Tibet for 2 years, in order to probe seismic anisotropy in the lithosphere beneath the region. The purpose of the project was to map deformation in the mantle lithosphere and compare it with observed deformation in the crust, in order to constrain the rheology of the lithosphere in the region. Such constraints

are necessary in order to settle some longstanding debates, for example the one regarding the coupling of the crust and the mantle and the strength of the lower crust. Furthermore, only a couple of years after we concluded our investigation in Eastern Tibet, the very same region was hit by the devastating Wenchuan earthquake (M8.0), a terrible disaster that pointed out again the importance of improving our understanding of this region and the forces controlling it. My observations, though, revealed a regional heterogeneity, which demonstrated that the discussion of the deformation history of Eastern Tibet needs to include a larger scope of regional processes. My work in Eastern Tibet, including details about the data and the methods I used, is described in chapter 2.

When rocks develop a fabric or a preferred orientation, their mechanical properties also become direction-dependent, similar to their elastic/seismic properties. Until recently, the vast majority of geodynamical models for the mantle neglected this fact, and assumed the material had isotropic viscosity. Even models used for predicting seismic anisotropy, thus inherently assuming the developing of preferred orientations, usually failed to account for the anisotropy of viscosity. In my thesis, I revisited this assumption by comparing models with and without anisotropic viscosity for several fluid dynamics situations.

First, I looked at Rayleigh-Taylor instabilities, a classic fluid dynamics problem describing the flow occurring when a layer of a dense fluid is placed over a layer of a more buoyant fluid. This situation is relevant to geodynamics on many scales, from magma fingering, through diapirs to lithosphere instability. Through a combination of analytical solutions and numerical finite-element experiments I found that the wavelength of Rayleigh-Taylor instabilities strongly depends on the orientation of the pre-existing anisotropy. My numerical experiments also demonstrated that contact locations between regions with different anisotropy orientations are particularly prone to develop instability. The results and some of their interesting implications are presented in Chapter 3.

Next, I included anisotropic viscosity in models of slab subduction. Anisotropic viscosity led to a change in the thermal structure of subduction zone wedges, resulting in time variability and a decrease in melt production in the wedge, without requiring any changes in subduction speed or angle. The anisotropic viscosity leads to smaller melt fluxes and

partial-melting region in the wedge and to widening of the region dominated by power-law creep.

Lastly, I examined the influence of the degree of anisotropic viscosity and of grain size, two important rheological parameters that are generally poorly constrained, on the development of the confined layer of anisotropy at the top of the convecting upper mantle. I found that the plate velocity and the derived strain rate do not have a large influence on the localization of shear and power-law creep. The grain size and the degree of anisotropic viscosity, on the other hand, are important. I found that a grain size larger than 10mm gives the best fit to the seismic observations; The ratio of shear viscosity to normal viscosity needs to be 0.3 or more, depending on grain size.

During my modeling efforts, I had to ensure that the numerical method I employed to track the anisotropy in the models – the directors method - was accurate and loyal to natural processes of fabric development. I conducted a rigorous comparison of this method with two other popular methods for fabric prediction, as well as with laboratory measurements. The findings are described in chapter 6. I estimated the trade-offs between accuracy and computational efficiency, and concluded that, after some calibration and adjustment, the directors method provides an appropriate solution for fabric prediction in applications where calculation speed is important. This kind of benchmarking is an essential part of the world of numerical modeling. For geodynamical models to be relevant, one must ensure that approximations are made carefully and are appropriate. Open communication between geodynamicists and the rock mechanics and mineral physics communities are required for achieving this goal, as we demonstrated in the efforts that have gone into this thesis with respect to fabric development and anisotropy. In addition, great progress can be made by adapting tools developed in other disciplines. An example are the tools developed by glaciologists to model deformation of anisotropic ice, which may be adapted for the mantle.

To summarize, the work presented in this thesis describes a step forward in the on-going effort to harness the power of anisotropy, through a combination of geodynamical modeling and seismic observations, in order to improve our understanding of deformation and flow in the Earth's interior. Chapter 2 gives an example of how observations of seismic anisotropy

has changed our view of the tectonic forces controlling deformation in one particular area – Eastern Tibet. This thesis proves that such self-consistency in the prediction of and accounting for anisotropy is crucial, by showing the dramatic effect of anisotropic viscosity on the development of the upper mantle layered anisotropy structure 5, Rayleigh-Taylor instabilities (Chapter 3), and the thermal structure of the subduction zone mantle wedge (chapter 4). The technique we use in our models is discussed in detail in chapter 6.

Chapter 2

Seismic Anisotropy in Eastern Tibet from Shear-Wave Splitting

2.1 Abstract

Knowledge about seismic anisotropy can provide important insight into the deformation of the crust and upper mantle beneath tectonically active regions. Here we focus on the southeastern part of the Tibetan plateau, in Sichuan and Yunnan provinces, SW China. We measured shear wave splitting of core-refracted phases (SKS and $SKKS$) at a temporary array of 25 IRIS-PASSCAL stations. We calculated splitting parameters using a multichannel and a single-channel cross-correlation method. Multiple layers of anisotropy cannot be ruled out but are not required by the data. A Fresnel zone analysis suggests that the shallow mantle (between 60-160 km depth) is the most likely source of anisotropy. The fast polarization directions do not correlate well with known surface features, such as faults, geologic units, and geodetic estimates of the crustal displacement fields, in particular in the southern part of the study region. Indeed, despite evidence from GPS campaigns for North-South crustal flow across the Red River Fault, the pattern of anisotropy argues against such flow in the upper mantle. While these observations support models of mechanical crust-mantle

[0]Published as: Lev, E., M. D. Long and R.D. van der Hilst, Seismic anisotropy in eastern Tibet from shear wave splitting reveals changes in lithospheric deformation, Earth. Planet. Sci. Lett. 251 (2006), p. 293-304.

decoupling, coherent deformation of the lithosphere cannot be excluded on the basis of the shear wave splitting results alone. The polarization directions reveal a pronounced transition from primarily North-South in the north (Sichuan) to mostly East-West orientations in the south (Yunnan). The interpretation of the shear wave splitting results is non-unique, but it is probable that the observed transition reflects a fundamental change in deformation regime. This may involve lateral variations in lithosphere rheology (that is, the level of crust-mantle coupling), and a southward transition from the direct impact of the continental collision to dominance of the far-field strain field associated with regional subduction processes. Understanding the nature of the lateral change in deformation regime may prove critical for our understanding the geotectonic evolution of eastern Tibet, in particular, and, perhaps, of the Tibetan plateau and Indochina, in general.

2.2 Introduction

The Tibetan plateau is the result of the collision between India and Eurasia, which started approximately 50 million years ago and which has produced at least 2000 km of convergence. Since the collision the Tibetan crust has doubled in thickness, and the plateau surface has been elevated to 4-5 km (Molnar and Tapponnier, 1978).

Distinctly different mechanisms have been suggested to explain the evolution of the Tibetan plateau and adjacent regions. Molnar and Tapponnier (1975), and many later studies, place significant relative motion along major strike-slip faults to facilitate eastward extrusion of crustal material out of Tibet. Other interpretations, in contrast, focus on modes of crustal thickening. England and Houseman (1986) used numerical models of a thick viscous sheet, in which the Asian crust is thickened by collision of an indentor. These models predict significant shortening in the eastern margin of Tibet. However, despite the high elevation in the area, no evidence for significant upper crustal shortening has been found (Burchfiel et al., 1995). This led researchers to develop a model which invokes ductile flow of the lower crust and mechanical decoupling of the upper crust and mantle (Royden et al., 1997). According to this model, which is supported by geodetic studies (e.g., Chen et al. (2000), Zhang et al.

(2004) - see Figure 2-1), material extruded from Tibet flows clockwise around the eastern Himalayan syntaxis into southeastern Tibet and Yunnan province, and across the Red River Fault zone.

Because pervasive deformation of rock may produce anisotropy on the scale of seismic wavelengths (e.g., Zhang and Karato, 1995; Tommasi et al., 2000; Kaminski and Ribe, 2001) we may be able to discriminate between competing tectonic models by analyzing the style of seismic anisotropy that they would produce. Ductile flow in the lower crust requires that it is weak, and the implied mechanical decoupling between the shallow crust and the upper mantle may produce a complex anisotropic structure. In contrast, a crust and mantle that are strongly coupled would deform coherently so that the associated anisotropy is likely to be more homogeneous.

Seismic anisotropy can be probed using a variety of seismological tools, including surface waves (e.g. Montagner and Nataf, 1986; Simons and van der Hilst, 2003), anisotropic receiver functions (Levin and Park, 1998), Pn travel times (e.g. Hess, 1964; McNamara et al., 1997), and shear wave splitting (e.g Silver and Chan, 1991). Shear wave splitting is an unambiguous indicator of anisotropy, but it is often difficult to determine the depth of the anisotropy that produces the observed signals.

Several seismic studies performed on or near the Tibetan plateau have attempted to determine the level of mechanical coupling between the crust and the mantle. McNamara et al. (1994) found systematic variations of anisotropy from the center of the plateau northward that were in agreement with surface geologic features. They concluded that the deformation resulting from the continental collision extends well into the upper mantle. Holt et al. (2000) compared results from shear-wave splitting studies with models of finite mantle strain in Tibet. Based on the alignment of the fast directions of shear-wave polarization with the direction of shear in the crust, they inferred that the present day direction of shear in the mantle is similar to that in the crust. A similar conclusion was reached by Griot et al. (1998), who found a strong correlation between azimuthal seismic anisotropy inferred from surface waves and the anisotropy predicted from a "homogeneous" model, in which the crust and the mantle deform coherently to a depth of at least 200 km. In contrast, using anisotropy of

the surface waves recorded at the INDEPTH-III array, Shapiro et al. (2004) found evidence for thinning of and flow in the lower crust in Tibet. Ozacar and Zandt (2004) used receiver functions to study crustal anisotropy, and also concluded that the middle crust in Tibet is likely to be weak and deform ductily. Recently, Flesch et al. (2005) combined shear-wave splitting measurements and geodynamical modeling to argue that the crust and the upper mantle are coupled in central Tibet but decoupled in Yunnan. Finally, shear-wave splitting measurements at an array north of the eastern Himalayan syntaxis (Figure 2-1, pink dots) are consistent with crust-mantle coupling in much of eastern Tibet (Sol et al., 2005).

We report measurements of shear wave splitting at a temporary seismograph array deployed in Sichuan and Yunnan provinces (Figure 2-1). Because our study region is located in the proximity of the presumed transition between the deformation regime of Tibet and that of Yunnan and south China (Flesch et al., 2005), our data may yield important insight into the style of deformation in eastern Tibet. Indeed, the region's oblique position to the direction of convergence may enhance three-dimensional processes, which might be harder to detect in the center of the plateau. Moreover, the unique structural features of eastern Tibet, specifically the abundance of strike-slip faulting, provide us with a range of surface observables that can be used to test proposed models.

Our analysis provides convincing evidence for anisotropy and shows that the source of the inferred anisotropy is most likely located between 60 and 160 km depth (that is, in the lower crust and the continental upper mantle), that the inferred orientation of strain in this depth range differs from structural trends observed at the surface, in particular on the SE flank of the plateau in Yunnan province, and that there is a distinct change in anisotropy across the array from North-South orientations in the north to East-West in the south. The latter may present evidence for a profound transition in lithosphere deformation regime, which may have important implications for our understanding of the geotectonic evolution of the Tibetan plateau.

2.3 Data and Methods

The data used here were recorded by a seismograph array operated by MIT and the Chengdu Institute of Geology and Mineral Resources (CIGMR) between September 2003 and October 2004. The array consisted of 25 broadband seismometers (20 STS2 + 5 Güralp 3ESP) from the IRIS-PASSCAL pool, deployed between latitudes 24°N-32°N and longitudes 99°E-101°E (Figure 2-1). We also used data from the Global Seismograph Network (GSN) station KMI, located in Kunming, Yunnan Province. In operation since 1992, and located within our temporary array, KMI is an important source of data and an ideal reference for the measurements made from our array.

With a deployment period of only 13 months, our array recorded SKS and SKKS data from a relatively narrow range of back azimuths. Furthermore, most of the sources are at an epicentral distance from which these core phases arrive within a time window shorter than the wave-length, making the signal too complex for measuring splitting with the methods used here. To increase the number of splitting measurements we also considered direct S arrivals from events that are sufficiently deep that source-side anisotropy can reasonably be ignored. There are several regions in the appropriate distance for such phases, including the deep seismicity beneath the northwest Pacific island arcs, but none of them provided high-quality splitting measurements.

Close to 3,000 SKS and SKKS phase arrivals from ∼350 teleseismic events ($\Delta = 85° - 180°$) and a body-wave magnitude greater than 5.7 were recorded during the period of deployment. From these, 300 records from a total of 41 events were selected through visual inspection based on their signal-to-noise ratio and waveform clarity. Figure 2-2 depicts locations of events used in the study. We used the cross-correlation method (e.g. Fukao, 1984; Levin et al., 1999) and the multichannel method (Chevrot, 2000) to calculate the splitting parameters, that is, the azimuth of the fast polarization direction ϕ and the delay time between the split phase arrivals, δt.

2.3.1 The Cross-Correlation method

A shear wave traveling through an anisotropic medium splits into orthogonally polarized fast and slow components. The cross-correlation method attempts to maximize the similarity in pulse shapes of these two components, which should ideally be identical, one delayed with respect to the other. Following Levin et al. (1999), we estimate errors for individual records assuming stochastic uncorrelated noise and applying a statistical F-test. With the individual measurements thus obtained, we perform a grid search over possible values for ϕ and δt to find the values that maximize the cross-correlation (Fukao, 1984). We search over a range of ϕ from 0 to 180° and δt between 0.1 to 2.5 s to find a $(\phi, \delta t)$ that produces the smallest root-mean-square misfit to the individual measurements. We estimate the error of the best fitting parameters using the width of the minimal misfit region in the grid search. For several stations the cross-correlation measurements vary widely (Figure 2-3), and estimating an average fast direction was difficult. For the stations presented we estimate that the error in the average ϕ is ±20° and the error in δt is ±0.2 s.

2.3.2 Multichannel method

The technique developed by Chevrot (2000) simultaneously utilizes phase arrivals from different back-azimuths. The amplitude of the transverse component for records with various incoming polarizations is measured, and the azimuthal variation is compared with the predicted variation for an assumed anisotropic medium. Provided that a broad range of incoming polarizations is available, this method is convenient to use with phases of known polarization, such as the core refracted SKS and SKKS. For a vertically incident shear wave traveling through a single horizontal layer of transverse anisotropy, and under the condition that δt is small compared to the dominant period of the signal, the radial (R) and transverse (T) time series are given by the following expressions:

$$
\begin{aligned}
R(t) &= w(t) \\
T(t) &= -\frac{1}{2}\,\delta t \sin(2\beta)\,\dot{w}(t),
\end{aligned}
\tag{2.1}
$$

where $w(t)$ is the original waveform of the pulse, $\dot{w}(t)$ is the time derivative of $w(t)$, and β is the angle between the fast direction ϕ and the initial polarization of the pulse. The splitting parameters can, therefore, be found by searching for the best fitting $\sin(2\theta)$ curve to the measured splitting vector. We calculate the error of individual splitting intensity measurements using the correlation between the transverse component and the time derivative of the radial component, as described in the appendix to Chevrot (2000). The error for the splitting parameters estimated for each station may be large.

2.4 Results

2.4.1 Splitting parameters for a single-layer model

The average splitting parameters that best fit the data are listed in Table A1 (electronic supplement) and illustrated in Figures 2-1 and 2-3. Figure 2-3a shows rose diagrams (angular histograms) of the fast polarization directions (FPDs) calculated by the cross-correlation method, as well as the estimate of the average fast direction under each of the stations. For stations at which we were able to estimate splitting parameters with the multichannel method, those measurements are also indicated. Figure 2-3b summarizes the best-fitting FPDs for stations that are well constrained, along with major regional faults and surface displacement field measured by GPS. As representative examples, we will describe below the results for stations *MC04* and *MC08*. At stations *MC19* and *MC20* not enough records showed measurable splitting due to a low signal-to-noise ratio, and hence no results are reported for them.

Station MC08 - located near the town of Jiulong, in the central part of the array (Figure 2-3). The cross-correlation method yielded a wide range of fast directions and delay

times. Searching for the average value in this case is problematic (Figure 2-4 e,f). The multichannel fit is better constrained, however, and hence this is the value illustrated in our maps.

Figure 2-3 reveals a complicated pattern of fast directions. (We note that for stations *MC05, MC08, MC22,* and *MC25* we used the splitting parameters from the multi-channel method.) First, for many of the stations the FPDs measured with the cross-correlation method vary strongly with back-azimuth. Second, at eight stations both methods yield good measurements, but the FPDs from them differ by 25° or more. Third, FPDs are quite different from the main trends in the surface geology and in the GPS displacement field (Figure 2-3b). Indeed, the correlation between the FPDs and the direction of faults is rather poor (Figure 2-5a), although visual inspection suggests that it is better in the north than in the south of the array. Furthermore, Figure 2-5b indicates that, in general, the FPDs do not correlate with the directions of σ_{SH} as inferred from the World Stress Map project (Reinecker et al., 2004).

Despite the scatter at individual stations, however, the measurements reveal a conspicuous transition from mostly North-South oriented fast directions in the northern part of the array (Figures 2-3 and 2-6a) to fast directions oriented mostly East-West in the southern part of the array (Figures 2-3 and 2-6b). Interestingly, the fast polarization directions in the South are – within error – parallel to the absolute plate motion (APM) in the region, which is $\sim$ N100°E according to NUVEL-1 (DeMets et al., 1994) (Figure 2-6).

2.4.2 Evidence for multiple layers of anisotropy?

It has been suggested, for instance by Levin et al. (2004) and Long and van der Hilst (2005), that the kind of variability observed in some stations of our array (Figure 2-3) indicates an anisotropic structure that is more complex than the single layer assumed initially. Also the relationship between the FPD pattern and the main trends in the surface geology and in the GPS displacement field (Figure 2-3) suggests significant complexity. Therefore, we tested whether a model consisting of two horizontal anisotropic layers could explain the data better. Since the two analysis methods described above assume a single anisotropic layer

with a horizontal fast axis, some modifications are necessary when a double-layer structure is considered.

For a two-layer model, the splitting parameters measured with the cross-correlation method are expected to depend strongly on the initial polarization of the waves (Silver and Savage, 1994). For a vertical incidence the "apparent" splitting parameters vary with back-azimuth with a $\pi/2$ periodicity (e.g. Rumpker and Silver, 1998). In this study we use the algorithm due to Savage and Silver (1993) for predicting apparent splitting parameters for a given double-layer model. We try to find a set of two pairs of splitting parameters $[(\phi_1, \delta t_1), (\phi_2, \delta t_2)]$, for the bottom and top layers respectively, that would give the best fit to the measured apparent splitting parameters.

For the multichannel method the splitting intensity is the integration over depth of the intensity caused by each of the layers through which the wave travels. Mathematically this is equivalent to a summation of sinusoids, which is a sinusoid with a different phase and amplitude. With this method it is, therefore, difficult to discriminate visually between a case of multiple horizontal layers or a single layer. We performed a grid search over a range of fast directions and delay times for a two layer model. The step size was 10° for direction and 0.1 s for delay time. The misfit was calculated using the root-mean-square of the difference between the data and the model predictions, weighted by the individual errors.

Because of the limited azimuthal coverage, constraining a complex structure was difficult. While the FPDs of the lower model layer could in most cases be constrained within ±10°, the upper layer was mostly unconstrained. Figure 2-4c,d and 2-4g,h display results for stations *MC04* and *MC08*. We find that, in general, a double-layer model does not significantly improve the fit to the data. In some cases, however, using a double-layer model reduces the disagreement between the results from analysis methods, which we regard as an improvement. At station *MC13*, for instance, whereas the single-layer estimates of the two methods differ by 42° (Figure 2-4i,j), the double-layer solution is within error for both of them (Figure 2-4k,l). We conclude that while a two layer model may be consistent with our observations, the data considered thus far do not require it.

2.5 Discussion

One of the main results of our analysis is the clear north-to-south transition in the orientation of the FPDs (Figures 2-3 and 2-6). Exceptions to the trends, such as stations *MC04, MC05, MC13*, and *MC17*, may be affected by local, near-station structure. Interestingly, this transition appears to connect the trends inferred from studies in neighboring areas; Sol et al. (2005) measure NW-SE trending FPDs to the northwest of our array (Figure 2-1, pink dots), whereas Flesch et al. (2005) report East-West FPDs for Yunnan province, south of our study region (Figure 2-1, orange dots).

2.5.1 Arguments for an upper mantle source of the splitting signal

An inherent limitation of using core-refracted waves such as SKS and $SKKS$ to study anisotropy is the path-integration of the signal, which makes it difficult to determine the depth of anisotropy. However, the following observations give some insight about the depth of the anisotropy. First, at many stations the inferred splitting time is > 0.6 s, which is generally considered too large to be all of crustal origin (Barruol and Mainprice, 1993). However, with a crustal thickness of 50-70 km this by itself is not a strong argument for a sub-crustal origin. Second, the approximate width of the Fresnel zones of the recorded phases help estimate the maximum and minimum depth of the anisotropy. For example, the neighboring stations *MC04* and *MC08*, separated by 117 km, show different splitting. This suggests that the anisotropy has a fairly shallow source. Using a quarter-wavelength approximation for the Fresnel zone width (Alsina and Snieder, 1995), we estimate that most of the anisotropic signal probably originates above 160 km depth. On the other hand, the comparison of the splitting of two events from opposing back-azimuths recorded at a single station suggests a minimum depth of the anisotropy of 65 km.

Also the comparison with independent observations makes it unlikely that the anisotropy inferred here has a near-surface origin. The regional strike-slip faults and the surface stress field presumably reflect upper crustal processes. If the cause of anisotropy is the alignment of crustal minerals by extensive shearing, or if the shear in the upper mantle is strongly

connected to that in the crust, we would expect the FPDs to align with strike-slip faults. If, however, the source of anisotropy is the alignment of micro-cracks in the shallow crust, the FPDs would align with the direction of the most compressive stress, σ_{SH} (e.g. Leary et al., 1990; Peng and Ben-Zion, 2004). Figure 2-5 suggests that, in general, the FPDs in the region under study correlate neither with the strikes of faults nor with the directions of the most compressive stress, which suggests that the main source of anisotropy is unlikely to be crustal.

2.5.2 Anisotropy in Yunnan province and near the Red River Fault

The fast directions just north of the Red River fault zone are particularly intriguing, as they suggest that the uppermost mantle is deforming in East-West direction, in contrast with models that suggest that near-surface deformation is in North-South direction and continuous across the fault (e.g. King et al., 1997). The situation in this part of our array may, however, be more ambiguous than it may appear at first glance.

Strike-slip faults are the most prominent structural features in this part of our array. In general, the strikes of these shear zones are approximately North-South, which is almost perpendicular to the direction of the anisotropic fabric in the upper mantle as inferred from shear wave splitting. It appears, however, that this area is actually undergoing rather significant East-West extension (e.g. Wang and Burchfiel, 1997; Wang et al., 1998). The driving force for this transtensional tectonics is not well known. It could be related to distant subduction processes, including slab roll back, to the west (Andaman system) and south-east (e.g., Philippines and Indonesia). Alternatively, it could reflect East-West strain in the crust as it spreads out when it slides off the flanks of the plateau. The latter would be consistent with the divergence in the directions of near-surface displacement inferred from GPS measurements.

If the crust is indeed extending in that fashion, then the East-West trending fast directions we observe in the south would, in fact, align with surface processes, even if there is substantial mechanical decoupling between the crust and the uppermost mantle. However,

the crust contribution to the splitting signal is probably minor (see previous section) and an explanation must still be sought for the dramatic southward change in the deformation of the uppermost mantle revealed by our splitting measurements.

2.5.3 Implications for lithosphere mechanics

The observations presented here give a first-order estimation of anisotropy in eastern Tibet and have implications for our understanding of lithospheric deformation, including, perhaps, the level of crust and mantle coupling in the region.

The splitting measurements suggest that the uppermost mantle is the most likely source of the anisotropy measured here, and that its deformation geometry is different from that in the crust. The anisotropy may be either a result of recent deformation, representing present-day processes, or a fossilized fabric resulting of an older process. If we take the anisotropy to represent the current deformation regime in the uppermost mantle beneath eastern Tibet, then our observations and inferences are suggestive of mechanical decoupling of the upper crust from the mantle, in particular in the south. We stress, however, that with the data presented here we cannot rule out the contrary, and in the northern region within the plateau such decoupling may not be required to explain the observations discussed here.

Irrespective of the level of crust-mantle decoupling, our results suggest a profound change in deformation regime. Further studies are needed to establish the nature of transition in more detail, but we postulate that it reflects a transition from collision controlled deformation in the North and Northwest, including the Tibetan plateau itself, to deformation influenced by other forces further to the South. The vertical resolution, limited when using teleseismic shear-wave splitting, may be improved by using anisotropic receiver functions or through the analysis of splitting in (P-S) conversions at the Moho or at intra-crustal interfaces. Unfortunately, our array may not provide sufficient data for such detailed analysis. A more promising approach toward constraining the radial variations of anisotropy would be the tomographic inversion of relatively short-period surface wave dispersion (Yao et al., 2006).

2.6 Summary

We used shear-wave splitting to investigate seismic anisotropy and deformation in Eastern Tibet. Even though there is significant scatter, the measurements based on the assumption of a single layer of anisotropy reveal a conspicuous change in the fast direction pattern from mostly North-South orientations in the north to mostly East-West in the south. Based on the magnitude of delay times, the size of Fresnel zones, and the poor correlation between directions of fast polarization on the one hand, and near-surface geology and geodetically inferred surface displacement patterns, on the other hand, we argue that the anisotropy is most likely located in the lower part of the thick crust and in uppermost mantle.

Distinguishing between different rheological models may be difficult based solely on the shear-wave splitting measurements we present here. In the northern part of the array the data may be consistent both with coherent deformation of the shallow crust and the uppermost mantle and with mechanical decoupling between them. However, in Yunnan province and the SE flank of the Tibetan plateau, the observations suggest differences in the deformation patterns of the crust and mantle, and hence mechanical decoupling. The implied transition between the northern and southern parts of our study region may reflect lateral variations in lithosphere rheology, or a change in the tectonic regime, with the impact of the collision weakening and that of far-field forces related to distant subduction processes strengthening as we go southward. If corroborated by further study, this transition should be accounted for in geodynamical models for the evolution of the Tibetan plateau.

2.7 Electronic supplement

Station	**Latitude**	**Longitude**	$\phi(^\circ)$	$\delta_t(s)$	Number of Records	Method
MC01	30.9998	102.3469	140	0.45	9	Cross-corr.
MC02	30.3830	103.4273	160	0.50	4	Cross-corr.
MC03	30.0086	102.4891	150	0.55	14	Cross-corr.
MC04	30.0550	101.4805	60	1.05	20	Cross-corr.
MC05	29.9921	100.2207	110	1.05	10	Multichannel
MC06	28.9378	99.7942	150	0.70	9	Cross-corr.
MC07	29.0401	100.4215	30	0.95	9	Cross-corr.
MC08	28.9959	101.5118	0	1.00	11	Multichannel
MC09	28.9592	102.7641	140	0.45	7	Cross-corr.
MC10	28.9761	103.8705	140	0.80	4	Cross-corr.
MC11	28.3315	103.1239	160	0.65	10	Cross-corr.
MC12	27.6629	102.2084	170	0.45	7	Cross-corr.
MC13	27.7415	100.7564	70	0.45	5	Cross-corr.
MC14	27.8646	99.7352	0	0.40	7	Cross-corr.
MC15	26.7588	99.9883	160	0.30	4	Cross-corr.
MC16	27.1824	103.6330	110	1.50	7	Cross-corr.
MC17	26.4706	101.7437	100	0.40	4	Cross-corr.
MC18	26.0598	103.1968	150	0.80	8	Cross-corr.
MC21	25.4878	99.6433	97	0.95	8	Cross-corr.
MC22	24.5325	100.2400	95	0.50	6	Multichannel
MC23	24.9340	101.5104	90	0.45	4	Cross-corr.
MC24	24.1663	102.8304	100	0.25	5	Cross-corr.
MC25	24.8862	103.6712	85	0.75	4	Multichannel
KMI	25.1233	102.7400	85	0.6	22	Cross-corr.

Table 2.1: Preferred model results for all the stations. ϕ and δt are the fast direction and the delay time estimated, respectively.

2.8 Figures

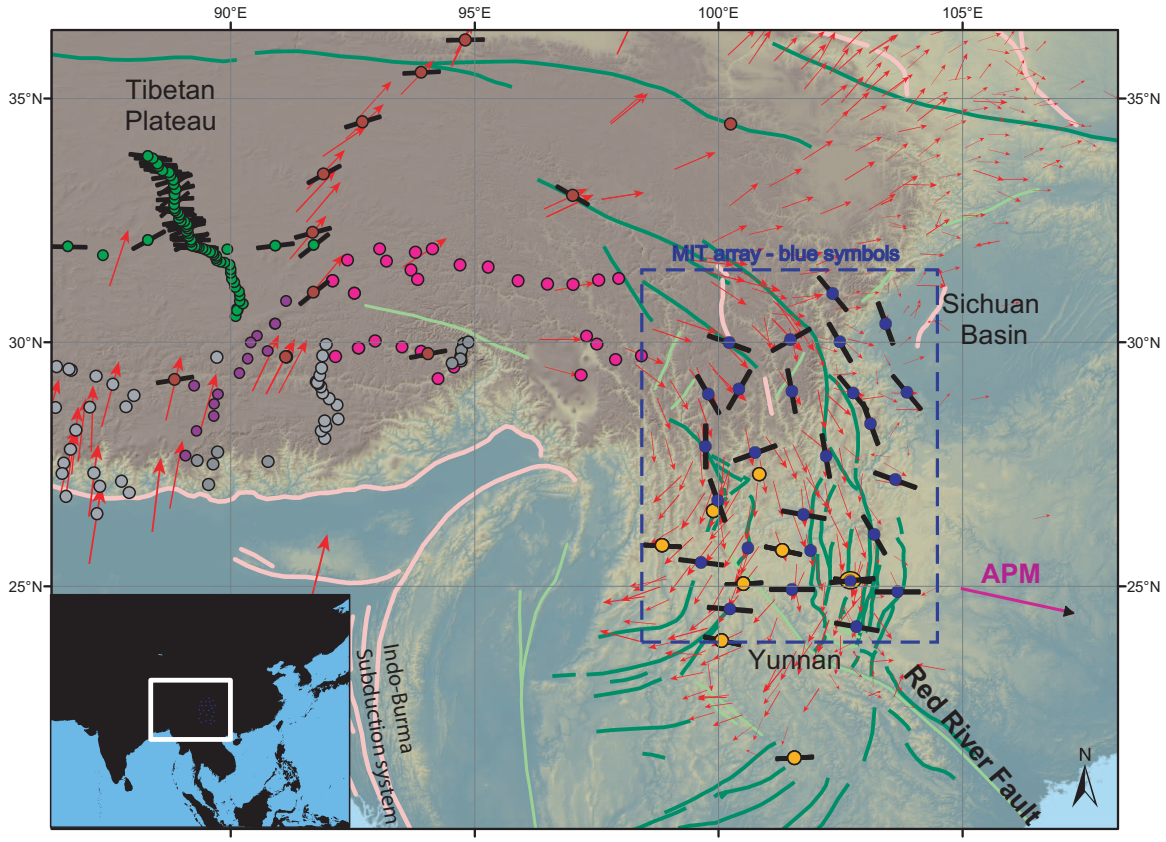

Figure 2-1: Location of the seismic stations used in this study (blue dots) and the fast polarization direction estimated for them. The background shows the topography of East Asia and the regional faults (dark green - left-lateral strike-slip faults, light green - right-lateral strike slip faults, pink - thrust faults). RRF = Red River Fault. APM = the local absolute plate motion direction, NUVEL-1 (DeMets et al., 1994). Previous shear waves splitting results are also shown: Green dots - Huang et al. (2000); Red dots - McNamara et al. (1994); Orange dots - Flesch et al. (2005). Pink dots depict the location of the seismic stations used by Sol et al. (2005). Red arrows denote geodetically measured surface velocities relative to the South China block (after Chen et al., 2000; Zhang et al., 2004).

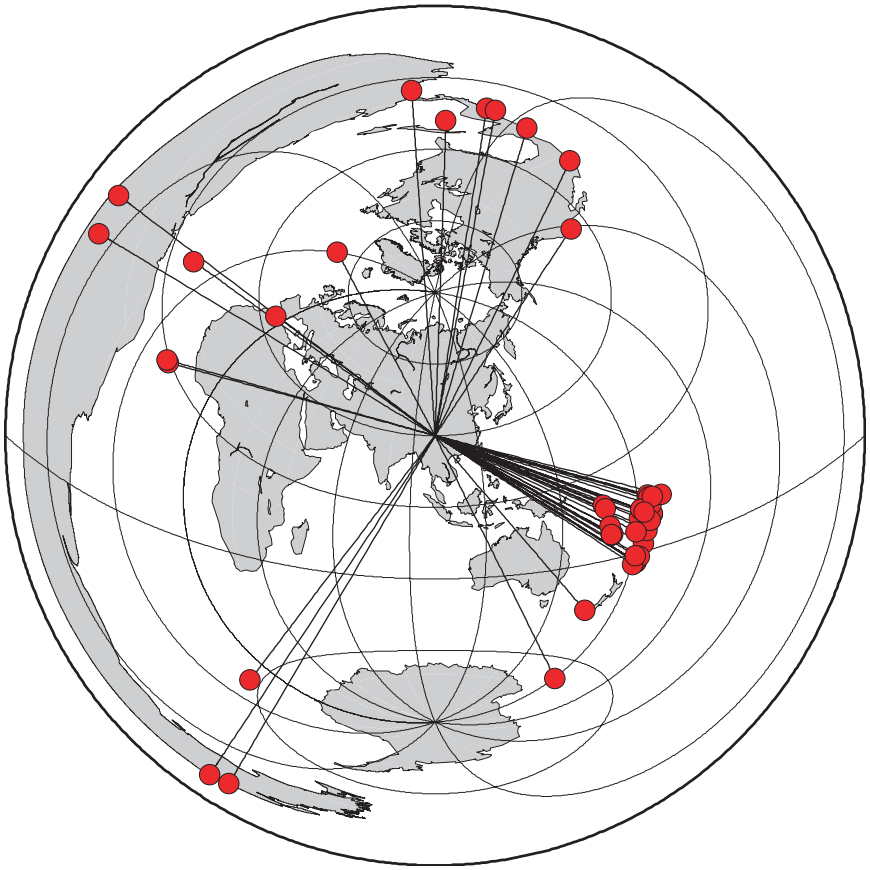

Figure 2-2: Epicenters of events used in the study (red dots). We use a total of 41 events of magnitude 5.7 and above.

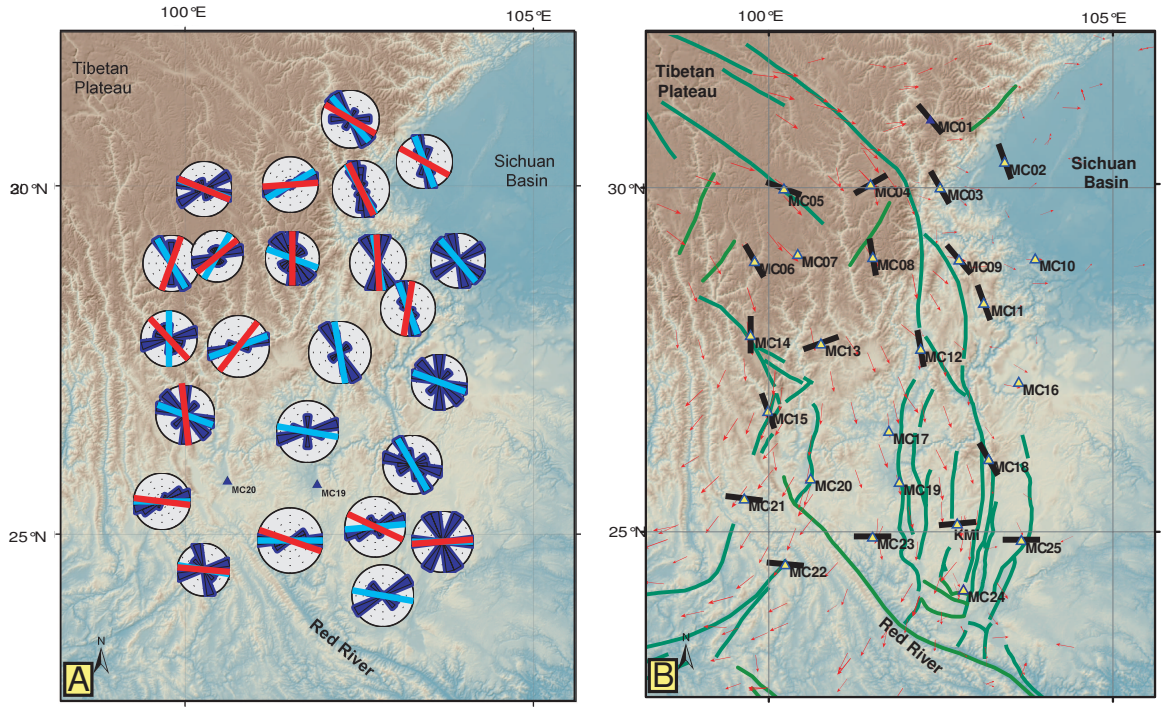

Figure 2-3: Splitting measurements in eastern Tibet (assuming a single-layer). (a) For each station, we show an angular histogram of the measurements obtained using the cross-correlation method (blue). Cyan lines show the angular average. Where applicable, red lines in the histograms give the fast direction obtained using the multichannel method. RRF - Red River Fault; (b)Average fast directions for well-constrained stations (black lines). Red arrows denote surface displacement vectors from Chen et al. (2000) and Zhang et al. (2004). Green lines show the major regional strike-slip faults.

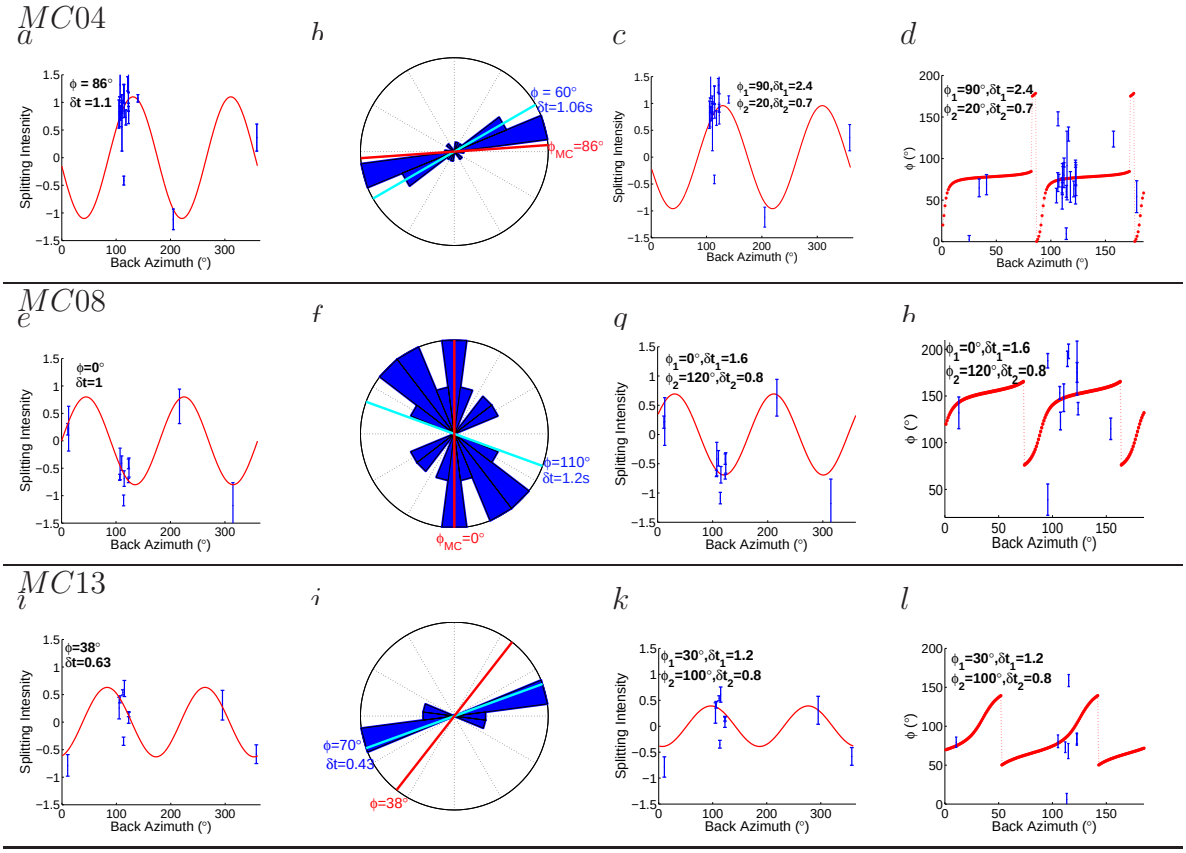

Figure 2-4: Results for station MC04, MC08, and MC13. Shown are 2σ error bars. From the left:
a,e,i - Splitting intensity measurements from the multichannel method (blue), with the red curve the fit assuming a single layer of anisotropy; b,f,j - rose diagram of FPD measurements from the cross-correlation method (blue), with mean direction indicated in cyan; c,g,k - Splitting intensity measurements, with a fit based on a double layer of anisotropy; $\phi_1, \delta t_1$ are splitting parameters for the bottom model layer, sampled first, and $\phi_2, \delta t_2$ are the splitting parameters for the model top layer, sampled second; d,h,l - Measured fast directions vs. back-azimuth (blue) and the predicted fast direction assuming a double layer model (red);

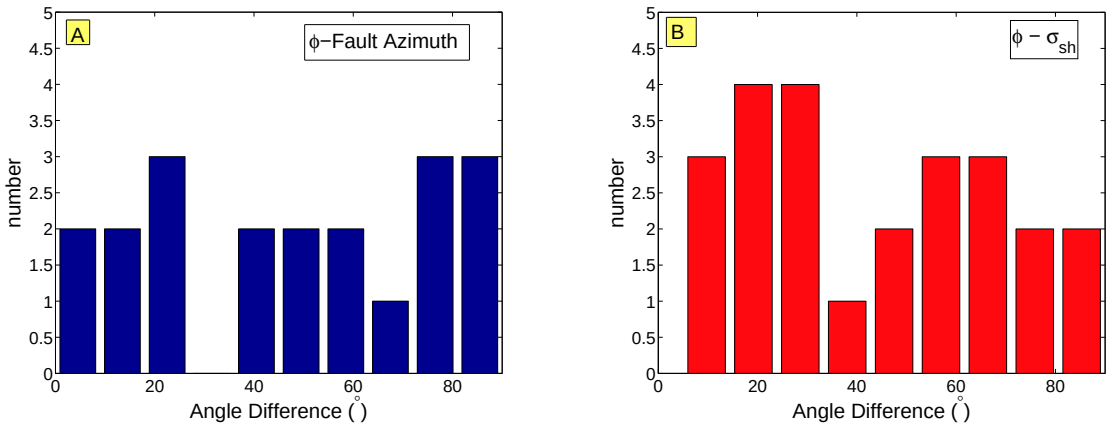

Figure 2-5: Testing the correlation of fast polarization directions with surface features: Histogram of angular difference between measured FPDs and nearest fault strike (a) and local most compressive stress direction σ_{SH} as estimated from the world stress map. (b). We note that FPDs of stations *MC02, MC07, MC10* and *MC13* are not compared to faults because they are too far from mapped strike-slip faults. No fast directions were calculated for *MC19* and *MC20*, due to insufficient data.

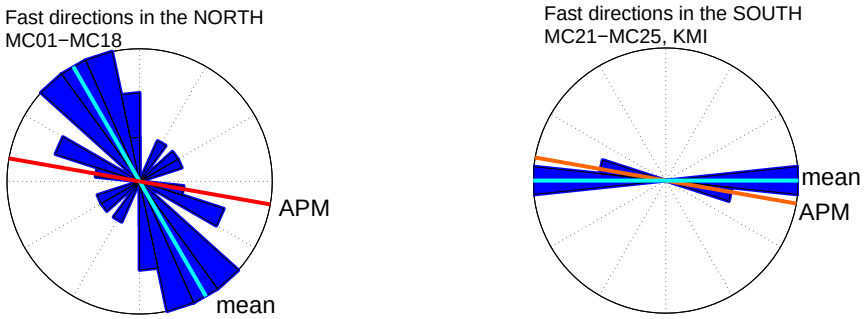

Figure 2-6: Rose diagram for the average FPDs of the stations in the northern and central parts of the array (left) and in the south (right). Average FPDs for stations *MC01* through *MC18* are included in the northern and central region. Average FPDs for stations *MC21* through *MC25* and KMI are included in the southern region. The mean direction and the NUVEL-1 absolute plate motion (APM) direction are indicated. These summary diagrams demonstrate that there is a transition from a NNW-SSE trend in the north and center to an E-W trend in the south.

Chapter 3

Rayleigh-Taylor instabilities with anisotropic lithospheric viscosity

3.1 Abstract

Rocks often develop fabric when subject to deformation, and this fabric causes anisotropy of physical properties such as viscosity and seismic velocities. We employ two-dimensional analytical solutions and numerical flow models to investigate the effect of anisotropic viscosity on the development of Rayleigh-Taylor instabilities, a process strongly connected to lithospheric instabilities. Our results demonstrate a dramatic effect of anisotropic viscosity on the development of instabilities - their timing, location, and, most notably, their wavelength are strongly affected by the initial fabric. Specifically, we find a significant increase in the wavelength of instability in the presence of anisotropic viscosity which favors horizontal shear. We also find that an interplay between regions with different initial fabric gives rise to striking irregularities in the downwellings. Our study shows that for investigations of lithospheric instabilities, and likely of other mantle processes, the approximation of isotropic viscosity may not be adequate, and that anisotropic viscosity should be included.

[0]Published as: Lev, E. and B.H. Hager, Rayleigh-Taylor Instabilities with anisotropy lithospheric viscosity, Geophys. J. Int. 173 (2008), p. 806-814.

3.2 Introduction

The response of anisotropic materials to stress depends on the orientation of the stress relative to the orientation of the anisotropy. Anisotropy of seismic wave speed in rocks has been studied vigorously in the last decades, both in experimental (e.g. Zhang and Karato, 1995) and theoretical work (e.g. Kaminski and Ribe, 2001). It has been shown that the deformation of rocks and minerals leads to development of crystallographic preferred orientation (CPO), which leads to seismic anisotropy (Karato et al., 1998). In addition, rotation of grains and inclusions, alignment of micro-cracks or melt lenses, and layering of different phases all lead to the development of shape preferred orientation (SPO), an important source for seismic anisotropy (e.g. Crampin, 1978; Holtzman et al., 2003; Maupin et al., 2005).

The anisotropic viscosity (AV) of earth materials has received less attention, but its effects are dramatic. Using laboratory experiments, Durham and Goetze (1977) showed that the strain rate of creeping olivine with preexisting fabric depends on the orientation of the sample and can vary by up to a factor of 50. This is because the orientation of the sample relative to the applied stress determines which slip systems are activated. In the experiments of Bai and Kohlstedt (1992) on high-temperature creep of olivine and those of Wendt et al. (1998) on peridotites, the measured strain rate depended strongly on the relative orientation of the applied stress to the sample crystallographic axis. Honda (1986) calculated the long-wavelength constitutive relations for a transversely isotropic material, and concluded that these can be characterized by two viscosities - a normal viscosity (η_N), associated with principal stresses normal to the easy-shear planes, and a shear viscosity (η_S), associated with shearing parallel to the easy-shear planes. More theoretical work (e.g. Weijermars, 1992; Mandal et al., 2000; Treagus, 2003) was done to assess the AV of composite materials, depending on the geometry and the relative strength of each component. These studies imply that regions of the earth that are not likely to become anisotropic by means of dislocation creep and LPO development may exhibit AV due to the deformation of composite materials, such as most natural rocks, and two-phase materials, such as partially-molten rocks. Recently, Pouilloux et al. (2007) discussed the anisotropic rheology of cubic materials and the consequences for geologic materials.

A few geodynamical studies have examined the effect of AV on mantle flow. Richter and Daly (1978) and Saito and Abe (1984) used analytical solution methods to investigate the development of Rayleigh-Bénard instabilities in a viscously anisotropic medium with specified easy-shear geometry, and found a connection between the anisotropy of the fluid and the length-scales of the convection cells. In a very instructive study a few years later, Christensen (1987) showed that the inclusion of AV affects two important mantle flows - postglacial rebound and thermal convection. For example, Christensen (1987) pointed out a spatial offset between mass anomalies and the resulting geoid signal in the presence of AV, which may help to reconcile the argued mismatch between observed uplift history near ice sheet margins and models of strong viscosity stratification in the mantle. AV also leads to channeling of flow into low viscosity region such as hot rising plumes. Nonetheless, Christensen concluded that the actual effect of AV in the earth's mantle would be much smaller, as the fabric required for creating AV would be obliterated by the highly time-dependent flow. However, the abundant evidence for seismic anisotropy in the earth and its strong correlation with tectonic processes and features suggest that large parts of the mantle maintain fabric for long times. Pre-existing mechanical anisotropy in the lithosphere was shown to have an effect in various tectonic settings such as oceanic shear zones (Michibayashi and Mainprice, 2004) and continental break-up parallel to ancient orogens (Vauchez et al., 1998).

Recently, Moresi, Mühlhaus and co-workers (e.g. Moresi et al., 2002, 2003) presented an efficient algorithm for including an AV that evolves with the flow in geodynamical models. They demonstrated the new algorithm in a series of papers, looking at various geological problems, including folding of a layered medium and thermal convection. We employ this technique here to investigate lithospheric instabilities in the presence of AV.

The lithosphere is often identified as the cold upper thermal boundary layer of Earth's convecting mantle. The colder temperature of the lithosphere makes it more dense than the asthenosphere underneath, and leads to an unstable density layering (Houseman et al., 1981). This density instability may be further enhanced by thickening of the lithosphere due to convergence (Molnar et al., 1998) or emplacement of dense material (eclogite) at

the base of the lithosphere (Elkins-Tanton and Hager, 2000). Lithospheric instabilities and removal of the lower lithosphere have been invoked to explain observations in the New England Appalachians (Robinson, 1993), the Canadian Appalachians (Murphy et al., 1999), Europe (Wenzel et al., 1997), Argentina (Kay et al., 1994), the North China craton (Fan et al., 2000; Wu et al., 2005) and Tibet (England and Houseman, 1989). Regions of high seismic velocity underneath southern California (Humphreys and Clayton, 1990; Kohler, 1999; Yang and Forsyth, 2006) are also interpreted as cold material sinking from the bottom of the lithosphere, probably as part of three-dimensional small-scale convection in the region (Humphreys and Hager, 1990) or Rayleigh-Taylor instabilities (Billen and Houseman, 2004). Upwelling of hot asthenospheric material following removal of the lower lithosphere has been suggested to explain, for instance, the massive flood basalts in Siberia (Elkins-Tanton and Hager, 2000).

The removal of the bottom of the lithosphere due to a density instability can be approximated as a Rayleigh-Taylor instability (Conrad and Molnar, 1997). Previous studies of Rayleigh-Taylor instabilities addressed the effect of the density structure, the wavelength of the density perturbation between the layers, and the rheology of the layers, on the timing and location of instability onset (e.g. Whitehead, 1986; Conrad and Molnar, 1999; Houseman and Molnar, 1997; Billen and Houseman, 2004). Here we demonstrate the significance of pre-existing and evolving fabric.

3.3 Anisotropic viscosity and the wavelength of instabilities

We begin our investigation with a simple conceptual setup: a dense anisotropic layer laying over a more buoyant isotropic half-space. All of the models in this study are two-dimensional. The interface between the two layers is perturbed by a small initial displacement $w(x) = w_0 \cos(kx)$, where x is the horizontal direction, and k is the wave number of the interface perturbation. Our goal in this section is to examine the dependence of the growth rate of instabilities on the wave number of the perturbation, the initial orientation - horizontal or

dipping - of the easy-shear planes, and the ratio between the shear and normal viscosities. We use both an analytical solution and numerical experiments for this purpose.

3.3.1 Governing equations

We treat the mantle as an incompressible fluid, an approximation valid for slow viscous deformation in the upper mantle (e.g. Schubert et al., 2001). The main equation to be solved is conservation of momentum:

$$\frac{\partial \sigma_{ij}}{\partial x_j} - \frac{\partial p}{\partial x_i} + f_i = 0 \tag{3.1}$$

where σ_{ij} is the deviatoric stress tensor, p is the pressure, f_i is the force acting in the i-th direction, and inertia is neglected. For our case, $f_z = \rho g \hat{z}$, where z is the vertical coordinate.

The flow also has to fulfill the continuity requirement for an incompressible material:

$$\frac{\partial v_i}{\partial x_i} = 0 \tag{3.2}$$

where $\mathbf{v}$ is the velocity.

A central equation for any flow model is the constitutive law, relating stress and strain in the system. The constitutive law we use in this study reflects the anisotropic rheology of the materials. The simplest form of anisotropy is transverse isotropy (TI), as for a deck of cards. As shown by Honda (1986), a TI material can be characterized by two viscosities - a normal viscosity, η_N, and a shear viscosity, η_S. This form of anisotropy can describe both a layered medium, consisting of layers of different strength, or the crystallographic preferred orientation of anisotropic minerals with a dominant easy glide plane. The normal viscosity governs deformation when the two principle stresses are oriented normal and parallel to the glide plane, while the shear viscosity governs deformation when the principle stresses are oriented at 45° to the glide plane. The exact expressions we use for our analysis are given in equations (3.4) and (A1).

We note that in this formulation, materials with horizontal and vertical easy-shear directions are mathematically equivalent. This is similar to a stack of books on a shelf - it is easy

to shear the stack horizontally both when the books stand up (vertical easy-shear planes) and when they lay on top each other (horizontal easy-shear planes).We thus examine two end-member setups - in one the anisotropic dense layer initially has a horizontal easy-shear direction, and in the other the easy shear direction initially dips at 45°.

3.3.2 Analytical solution

In this analysis we use the propagator matrix technique (e.g. Hager and O'Connell, 1981) to calculate the growth rate of the instabilities as a function of the wavelength of a small perturbation in the interface between the two materials. The mean depth of the interface is at $z = 0$. The boundary conditions for our problem are no-slip at the top boundary ($z = 1$), which we take to be the base of the rigid part of the lithosphere, and vanishing of the velocities and stresses as $z \to -\infty$. By calculating the vertical velocity $v(z = 0)$ we are able to track the change in position of the boundary. The derivation is outlined in Appendix A, and an important outcome of it is that

$$v(z = 0) \equiv \frac{\partial w}{\partial t} \propto w \tag{3.3}$$

Because the velocity of the interface is proportional to the amplitude of the boundary topography (eqn. 3.3), the change in the interface depth follows an exponential growth rule: $w(z, t) = e^{\frac{t}{\tau}}$. τ, the growth rate, is a function of the wave number k of the perturbation w, and of the two viscosities η_N and η_S.

The results we present in section 3.3.4, as well as Appendix A, give insight into the relationship between the growth rate and a range of viscosities and wave numbers. We note here that this analysis is valid only for small interface perturbations, so we can assume that the orientation of the AV does not evolve.

3.3.3 Numerical experiments

To follow the instability to finite amplitude requires a numerical approach. We solve the flow equations using a finite element formulation on an Eulerian mesh embedded with Lagrangian

integration-points ("particles"), as described by Moresi et al. (2003). In this method, particles carry the material properties, and foremost their deformation history and the derived AV. Variables such as velocity and pressure are calculated at the location of the mesh nodes, which are fixed in space. We use the software package *Underworld* (Moresi et al., 2007) to solve the flow equations.

Including anisotropy in the flow equations

To include AV in our numerical experiments, we use the particle-in-cell formulation (Moresi et al., 2003). By this method, the anisotropy is represented by a set of *directors* advected through the model, analogous to particles (Mühlhaus et al., 2002b). The directors are vector-particles pointing normal to the easy-glide plane or layer, thus defining the directions associated with η_N and η_s. In each time step of the calculation, the directors are advected and rotated by the flow, and in return determine the viscosity structure for the next time step (Mühlhaus et al., 2004).

The AV enters the equation of momentum through a 'correction' term added to the isotropic part of the constitutive equation relating stress and strain rate (Mühlhaus et al., 2002b):

$$\sigma_{ij} = -p\delta_{ij} + 2\eta_N \dot{\epsilon}_{ij} - 2(\eta_N - \eta_S)\Lambda_{ijkl}\dot{\epsilon}_{kl} \tag{3.4}$$

where η_N, η_S are the normal and shear viscosities, respectively, σ is the deviatoric stress tensor, and $\dot{\epsilon}$ is the strain rate tensor. Λ reflects the orientation of the directors in space, denoted by $\mathbf{n}$:

$$\Lambda_{ijkl} = \frac{1}{2}(n_i n_k \delta_{lj} + n_j n_k \delta_{il} + n_i n_l \delta_{kj} + n_j n_l \delta_{ik}) - 2n_i n_j n_k n_l \tag{3.5}$$

The evolution of the orientation of directors in time is controlled by integration over time of

$$\dot{n}_i = -\frac{\partial v_i}{\partial x_j} n_j \tag{3.6}$$

(Belytschko et al., 2001). A more detailed description of how the anisotropy described by

the directors enters the equations of flow and how it is represented in the finite element formulation is given by Mühlhaus et al. (2002b).

Model setup

We carried out a suite of two-dimensional numerical experiments to investigate the development of instabilities in the presence of AV. The numerical models we use in this section consist of a dense layer with a uniform fabric throughout its width, overlying a more buoyant layer. The model domain is a rectangular box with an aspect ratio of 1:6.4, comprised of 240x32 elements. We place a dense layer in the top 15% of the box. Because the thickness of the lower layer is much greater than that of the upper layer, our analytical solution for a layer overlying a half-space should provide a reasonable approximation to the finite-depth domain. The interface between the layers is a cosine curve with an initial amplitude of 0.01. We compare the growth rate for models with an either horizontal or dipping initial easy-shear direction for a range of interface perturbation wavelengths. We measure the non-dimensional time that it takes to displace the interface by one element length, and define this time as the reciprocal of the growth rate. The ratio of the shear viscosity to the normal viscosity for the anisotropic material is 0.1 in all cases, in accordance with the theoretical estimations of Mandal et al. (2000) and Treagus (2003) and within the range of values measured in the experiments of Durham and Goetze (1977). The isotropic viscosity of the buoyant lower layer is equal to the normal viscosity (η_N) of the dense layer.

3.3.4 Results - a homogeneous but anisotropic upper layer

Both our numerical experiments and our analytical solution predict that the most unstable wavelength for a dense layer with a horizontal fabric is much longer than that for an isotropic layer or for a layer with a dipping fabric. From our analytical solution, we calculate the normalized values of τ for a range of wave-numbers and viscosity ratios, for both a horizontal fabric and a dipping fabric. The results are plotted in figure 3-1. For comparison, we also plot the growth-rate curves for models with an isotropic dense layer with a viscosity that equals the geometric and the arithmetic averages of the shear and normal viscosities of the

anisotropic material. Figure 3-1 clearly shows that the effect of anisotropy is dramatic, especially for a material with initially horizontal easy-shear direction. For such a fabric, the minimum point of the growth rate curve, which determines the most unstable wavelength, shifts to a longer wavelength as the viscosity ratio becomes smaller (blue curves in figure 3-1). For a case of a shear viscosity that is 10 times smaller than the normal viscosity, a fairly conservative estimate, the most unstable wavelength is twice as long as for the isotropic one; For $\eta_S/\eta_N = 0.01$, the increase is by a factor of 3.5. This increase in the most unstable wavelength is comparable to the effect of having an isotropic dense layer with a lower viscosity (green curves in figure 3-1). Also, the shape of the curve is changed compared to the isotropic case, and becomes flatter. For a dipping fabric (figure 3-1, red curves), the change is minor - the most unstable wavelength is equal to the isotropic and isoviscous one, and for long wavelengths the stability curves are almost identical for all degrees of anisotropy.

Figure 3-2 shows the results from our numerical experiments. We plot the growth rate versus the wave number of the density perturbation for each initial configuration of the dense anisotropic layer: horizontal fabric (blue line, squares), 45°-dipping fabric (red line, diamonds) and isotropic (black line, circles). The results agree with the predictions from the analytical solution presented above - the fastest growth rate for the horizontal fabric is at a longer wavelength than that for the dipping fabric or for an isotropic layer, and the curve is indeed flatter at longer wavelengths. The minimum growth rate for a dipping fabric is at almost the same wavelength as that for an isotropic material, again in agreement with the analytical predictions. Figure 3-3 shows the material distribution in the different model configurations after the fastest drips have sunk half of the box depth, as well as the approximate location of the initial perturbed interface (yellow curve). These snapshots demonstrate clearly that the wavelength of the instabilities developing in the initially horizontal models is greater than of those developing in the initially-dipping models. This emphasizes the advantage gained by using numerical experiments - the analytical solution gives insight into the behavior of instabilities at small amplitudes, while the numerical experiments are essential for predicting the behavior as the flow progresses and instabilities of finite-amplitude develop.

3.4 Laterally-varying anisotropy

Intrigued by the dramatic results for a simple model of a homogeneous anisotropic dense layer described above, we proceed and use numerical experiments to examine the effect of including lateral variations in the initial anisotropic fabric of the dense layer.

3.4.1 Model setup

Figure 3-4 depicts the model geometry and initial and boundary conditions. The model domain is again a rectangular box with an aspect ratio of 1:6.4. The location and amplitude of the interface between the layers is the same as in section 3.3. Following the findings of section 3.3, we perturb the interface with a wavelength long enough to allow deformation at a wide range of wavelengths to develop freely. The dense layer now contains two anisotropic regions in the center, each 1.6 wide, and two isotropic regions of the same high density near the edges. The anisotropic regions differ only by their initial fabric orientation - one (shown in red) initially has a horizontal easy shear direction, and the other has an easy shear direction initially dipping at 45° (shown in yellow). The viscosity of the buoyant layer is equal to the normal viscosity of the anisotropic layer. The shear viscosity of the anisotropic material is a factor of 10 less than its normal viscosity. We shift the anisotropic regions laterally in different models in order to change the phase between the viscosity structure and the density interface perturbation. We then examine the development of drips for each configuration.

3.4.2 Results - a heterogeneous upper layer

In figure 3-5 we show the instabilities that develop in our models. The different panels depict models with different configurations of the initial fabric domains, shown in red and yellow, as well as the results for an isotropic model for comparison (Fig. 3-5a). We also show the trace of the original density interface between the dense lithosphere and the underlying mantle (black horizontal curve) and the location of the deepest points of the initial perturbation of the density interface (dashed vertical lines).

Several first-order observations can be made in figure 3-5. First, there is a striking difference between the instabilities that develop in the two anisotropic domains. Most notably, the wavelengths of the downwellings that develop in the domain with easy horizontal shear are much longer than the wavelengths in the dipping-fabric domains or in the isotropic model (Fig. 3-5a). In addition, the domain which starts with easy horizontal shear (red) develops instabilities faster than the domain which starts with easy shear direction dipping at 45° (yellow). Next, for several situations, the fastest-growing downwelling does not coincide with the locations of maximum thickness of the dense layer, but is offset horizontally by up to 0.5 of the box depth (Fig. 3-5b,g). Finally, almost all of the fastest-growing instabilities occur near the edges of the domain of horizontal easy shear (excluding the case where the thickest part of the dense layer was exactly in the center of the domain of initial horizontal anisotorpy), but the instabilities that develop in the dipping easy shear domain develop in its interior. Evidently, the initial fabric and its lateral variations influence the flow significantly.

3.5 Discussion

Our models are set up in a non-dimensional manner, for generality. It is interesting, though, to re-scale the results to lithospheric dimensions. The dense layer (top 15% of the box) corresponds to the viscously-mobile part of the lithosphere, which is approximately its lowest 40 km. The viscosity of the lithosphere is temperature-dependent, and is believed to decrease exponentially with depth, with a reasonable decay length of about 10 km (Molnar et al., 1998). If we take the viscosity at the base of the lithosphere to be 10^{19} Pa s (Hager, 1991), then the average viscosity for a 40 km thick layer, calculated as $< \eta >= \exp(\frac{\log \eta_1 + \log \eta_2}{2})$, is $7.4 \cdot 10^{19}$ Pa s. Using the thickness of the lower lithosphere as the characteristic length scale, we can estimate the spacing between the isotropic instabilities as 130 km, and the wavelength of the longest anisotropic instabilities is close to 400 km. The lateral offset between the downwellings and the locations of maximum lithospheric thickness scales to a maximum of approximately 150 km. We re-scale velocities based on the the viscosity and density contrast, using the "Stokes Velocity" ($V_{Stokes} = \frac{\Delta\rho * g * h^2}{\eta}$, where η is the effective

viscosity of the dense layer, $\Delta\rho$ is the density contrast and h is the dense layer thickness). We estimate the difference between the density of the lower lithosphere and the density of the underlying asthenosphere as 40 kg/m^3 (Molnar et al., 1998). After substituting the above values we can now calculate the scaling of time. We estimate that the time it takes for the drips to sink to a depth of 160 km (the stage shown in Fig. 3-5) is approximately 12 Myrs. This duration is within the range of times estimated by Houseman and Molnar (1997) for removal of the base of an unstable thickened lithosphere. This time and distance of sinking imply an average sinking velocity of 14 mm/yr.

The models we present here are a preliminary attempt at this problem, and thus have some shortcomings when compared with the lithosphere. First, the fabric development rule we use is a simple rotational evolution law, and does not take into account factors such as temperature, strain rate, and recrystallization, all known to affect the development of CPO in rocks. Second, the rheology we use is a Newtonian creep law, while in fact anisotropy due to CPO requires deformation in the dislocation creep regime, which is a power-law creep process. Additionally, all our experiments are carried out in two dimensions. There may be interesting consequences when these effects are studied in a three-dimensional setup, especially given the three-dimensional nature of some observed mantle instabilities (e.g. Yang and Forsyth, 2006). A three-dimensional model would also be able to include orthorhombic symmetry and would not be constrained to the use of transverse isotropy. Hopefully future work would be able to assess the significance of these factors and their implications.

Both our analytical solution and the numerical flow models predict that the wavelength of Rayleigh-Taylor instabilities would be longer for an anisotropic material, most significantly for a fabric favoring horizontal flow. Some intuitive understanding of this can be gained if we imagine a horizontally layered medium - it is much easier for such a medium to flow sideways by simple shear, and not to develop vertical drips. Drips will eventually develop in locations where the horizontal flow encounters resistance - for instance in the form of a domain with a different fabric. This is likely the reason that the largest downwellings developed in the edges of the domains with initial horizontal easy shear direction (red domains in Fig. 3-5). If, on the other hand, the initial fabric is at an angle to the main acting force, it will be easier for

the instabilities to thicken by pure shear and 'break' the layering structure, and hence will be more likely to follow a wavelength closer to the isotropic one. This result is in agreement with the experiments of Richter and Daly (1978), who found that anisotropy leads, in general, to longer wavelengths of instabilities. Saito and Abe (1984) performed a marginal stability analysis for a related model setup (bottom-heated Rayleigh-Bénard convection with stress free boundaries and horizontal layering) and, similarly to our results, found that the stability curves flatten out and that the minimum shifts to a longer wavelength with lower viscosity ratio.

We emphasize at this point that numerical techniques such as the one we use here have several important advantages. Analytical solutions, while elegant, give insight into the behavior of instabilities only at small amplitudes, and thus numerical experiments are essential for predicting the flow as it progresses and instabilities of finite-amplitude develop. Additionally, the numerical technique we use is capable of modeling flows in which the fabric is evolving and the orientation of the anisotropy is not fixed in space, as opposed to the situation in our, as well as earlier (e.g. Richter and Daly, 1978; Honda, 1986), analytical solutions. It is also straightforward to include lateral variations of the anisotropy, a scenario highly relevant to tectonic processes in natural environments.

The strong effect of pre-existing fabric on the development of Rayleigh-Taylor instabilities may have important implications for the stability of the lithosphere. In our models, the fastest growing downwelling sometimes develops away from the initially deepest region of the density interface, due to the interaction between domains with different fabric orientation. This change in geometry may provide a simple explanation for the offset of the mantle drip beneath the Sierras (e.g. Saleeby and Forster, 2004). Our findings of the effect of AV on the wavelength of instabilities should also be considered in the context of other locations, for example Tibet. Conrad and Molnar (1997) argued that the wavelength of Rayleigh-Taylor instabilities predicted to arise from the collision between India and Eurasia is much shorter than the wavelength of the Tibetan plateau, and hence such instabilities are unlikely to be the cause of the rapid uplift of the plateau at 5-10 Myrs ago. If, however, the existing fabric in the collision zone was such that it leads to longer wavelengths, this possibility may need

to be reconsidered.

The points of contact between regions with different existing fabric appear to have unique significance. This hints that when tectonic units which have gone through a different evolution and developed different fabric are juxtaposed, this contact point may be particularly unstable. An example of such a situation may be the placing of a spreading center, which is characterized by horizontal easy-shear planes, next to a region that is more horizontally-resistant. When this combination is put under compression, the horizontal easy shear planes will be unstable at the contact point, which may lead to initiation of downwelling and perhaps even subduction. Subduction initiation at extinct spreading centers is likely the explanation for the subduction zone at the Macquirie region south of New-Zealand (Lebrun et al., 2003) and near the Oman ophiolite (Michibayashi and Mainprice, 2004). Our results clearly show that additional knowledge of the anisotropic fabric of the lithosphere, and, specifically, the orientation of dipping fabrics, can shed light on different tectonic problems, and highlights the importance of overcoming the difficulties in making such measurements (e.g. Chevrot and van der Hilst, 2003).

3.6 Summary

We show the dramatic effect of anisotropic viscosity on the development of Rayleigh-Taylor instabilities. The wavelength, timing and shape of the instabilities that develop in our models are strongly affected by the initial fabric prescribed. The most notable effect of anisotropic viscosity on Rayleigh-Taylor instabilities, demonstrated here both analytically and numerically, is the shift to longer wavelengths when the initial fabric of the dense material favors horizontal flow (horizontal or vertical fabric). The interplay between regions with different orientations of initial fabric gives rise to a variety of features, such as an offset of the main downwellings away from the deepest point of the perturbed interface, and demonstrates the importance of considering the deformation history of all the units participating in a tectonic setting. Our results show that for the study of lithospheric instabilities, and likely of other mantle processes, the common isotropic approximation may not be accurate, and

hence anisotropic viscosity should be included.

Acknowledgements. We are grateful for helpful discussions with Linda Elkins-Tanton, Ming Fang, Greg Hirth, Eduard Kaminski, Laurent Pouilloux, and Andrea Tommasi. A thoughtful review by Gregory Houseman helped greatly to improve this manuscript. The research presented here was supported by NSF under grants EAR-0337697 and EAR-0409564

3.7 Appendix A: Derivation of analytical solution

We begin by defining the following anisotropic constitutive relations, which describe a transversely isotropic (TI) material in the two special cases considered here of 1) easy-shear on horizontal/vertical planes and 2) easy-shear on planes dipping at 45°:

$$\sigma_{xx} = 2\eta_{ps}\dot{\epsilon}_{xx} \tag{A1a}$$

$$\sigma_{zz} = 2\eta_{ps}\dot{\epsilon}_{zz} \tag{A1b}$$

$$\sigma_{xz} = \eta_{ss}\dot{\epsilon}_{xz} \tag{A1c}$$

where η_{ps} is a viscosity corresponding to pure shear stresses, and η_{ss} corresponding to simple-shear. For a material with a horizontal easy-shear direction (horizontal layering, for instance) η_{ss} is equivalent to η_S defined in section 3.3.1, $\eta_{ps} \equiv \eta_N$, and $\eta_{ss} < \eta_{ps}$. For an anisotropic material with a dipping easy-shear direction, $\eta_S \equiv \eta_{ps} < \eta_{ss} \equiv \eta_N$. For an isotropic material, $\eta_{ps} = \eta_{ss}$. This constitutive relation can be derived from a matrix form similar to that in equation 3.4: $\sigma_{ij} = 2\eta_N\epsilon_{ij} - 2(\eta_N - \eta_S)\Lambda_{ijkl}\epsilon_{kl}$ where Λ is an alignment tensor reflecting the orientation of the symmetry axis. Then, the transformation from a horizontal symmetry anisotropy to a dipping symmetry can be achieved by a rotation of the 4th-order tensor Λ.

In our analytical solution, we employ the propagator matrix technique (e.g. Hager and O'Connell, 1981) to calculate the growth rate of Rayleigh-Taylor instabilities as a function of the wavelength of the density perturbation between the two materials. We set $z = 0$ at the interface between the layers, $z = 1$ at the top of the dense layer, and the initial location of the density interface as $w = w_0 \cos(kx)$. For the horizontal and 45°-dipping orientations we consider here, this definition of the interface perturbation leads to v_x, $\sigma_{zz} \propto \cos(kx)$, and v_z, $\sigma_{xz} \propto \sin(kx)$, where k is the wave number. For other orientations there may be a phase shift with depth (Christensen, 1987). Thanks to the orthogonality of the trigonometric basis functions, we can write a simplified set of equations for each wave number. We define a vector $\mathbf{u} = [v, u, \sigma_{zz}, \sigma_{xz}]$, where v is the vertical velocity, u is the horizontal velocity, σ_{zz} is the normal stress in the z direction, σ_{xz} is the shear stress, and x and z are the horizontal

and vertical coordinates. After some manipulation, this definition of $\mathbf{u}$ enables us to express the equations of flow in each layer for every k as

$$D\mathbf{u} = \mathbf{A}\mathbf{u} + \mathbf{b} \tag{A2}$$

where $D = \frac{\partial}{\partial z}$, and $\mathbf{b}$ is a forcing term. The matrix $\mathbf{A}$ is where the anisotropic viscosity is manifested.

The definition of the anisotropic constitutive relation above leads to a matrix $\mathbf{A}$ of the form:

$$\mathbf{A} = \begin{bmatrix} 0 & -k & 0 & 0 \\ k & 0 & 0 & \eta_{ss}^{-1} \\ 0 & 0 & 0 & -k \\ 0 & 4\eta_{ps}k^2 & k & 0 \end{bmatrix} \tag{A3}$$

When $\eta_{ps} = \eta_{ss}$ (isotropic material), the expression in (A3) is equal to the matrix $\mathbf{A}$ given by Hager and O'Connell (1981). Otherwise, it reflects the anisotropic viscosity of the material by including the two different viscosities.

The solution to equation (A2) is of the form

$$\mathbf{u}(z) = e^{\mathbf{A}(z-z_0)}\mathbf{u}(z_0) + \int_{z_0}^{z} e^{\mathbf{A}(z-\xi)}\mathbf{b}(\xi)d\xi \tag{A4}$$

We define the propagator matrix $\mathbf{P}(z, z_0) = e^{\mathbf{A}(z-z_0)}$, so that the velocities and stresses can be expressed as

$$\mathbf{u}(z) = P(z, z_0)\mathbf{u}(z_0) + \sum_{i=1}^{n} P(z, \xi_i)\mathbf{b}(\xi_i)\Delta\xi_i \tag{A5}$$

where ξ_i is the depth at the center of a the i-th layer and $\Delta\xi_i$ is the layer thickness. The propagator matrix for an anisotropic material will naturally be different than the propagator matrix for an isotropic material, given the difference in the corresponding $\mathbf{A}$ matrices. The boundary conditions for our problem are no-slip at the top boundary ($z = 1$), which we take to be the base of the rigid part of the lithosphere, and vanishing of the velocities and stresses

as $z \to -\infty$. We can express the boundary conditions using the vector $\mathbf{u}$ defined earlier:

$$\mathbf{u}(z=1) = [0,\ 0,\ \sigma^t_{zz},\ \sigma^t_{xz}], \qquad \mathbf{u}(z=-\infty) = [0,\ 0,\ 0,\ 0] \tag{A6}$$

In order to fulfill the boundary condition as $z \to -\infty$, $\mathbf{u}$ just below the interface has to be of the form $\mathbf{u}(z=0^-) = [C_1/2k,\ C_2/2k,\ C_1,\ C_2]$, where $C_1,\ C_2$ are the σ_{zz} and σ_{xz} at the interface. We add a normalized forcing term which here represents the gravitational forcing in the z direction. Thus $\mathbf{u}$ across the interface, at the bottom of the dense layer, becomes $\mathbf{u}(z=0^+) = [C_1/2k,\ C_2/2k,\ C_1+1,\ C_2]$. We propagate this $\mathbf{u}(z=0^+)$ upwards to the top interface using the anisotropic propagator matrix P_{ani}: $\mathbf{u}(z=1) = P_{ani}\mathbf{u}(z=0^+)$. From the no-slip boundary condition at the top, the first two components of the resulting vector are equal to zero. We now have two equations and two unknowns - C_1 and C_2. We solve for these two unknowns and use the result to calculate the vertical velocity at the interface.

The change in the interface location with time is equal to the vertical velocity at the interface - $v(z=0)$, where v is the vertical velocity. A result of the derivation described above is that the vertical velocity at the interface is proportional to the perturbation of the interface, that is:

$$v(z=0) \equiv \frac{\partial w}{\partial t} \propto w \tag{A7}$$

Therefore the change in the interface depth follows an exponential growth rule: $w(z,t) = e^{\frac{t}{\tau}}$, which gives the dependence of the growth rate τ on the model parameters:

$$\tau = \frac{1}{K(\eta_{ps}, \eta_{ss}, k)} \tag{A8}$$

K is a complicated function of the viscosities and the wave number, of the form $\Delta\rho g \times$*[a sum of exponents of powers of* $\eta_N, \eta_s,$ *and* k*]*. The exact expression is too long to give here explicitly, but can be obtained using the Matlab code in the electronic supplement. The resulting relationship between 1/K (τ) for a range of wave numbers and a set of viscosity ratios is demonstrated in figure 3-1; Figure S1 (Electronic Supplement) shows a similar calculation for a range of viscosity ratios and $k = 0.1$.

A careful inspection of the anisotropic matrix A_{ani} and the anisotropic propagator matrix P_{ani} reveals a very interesting phenomenon - an oscillatory behavior with depth for certain viscosity ratios. Let us define δ, the viscosity ratio, as $\delta = \frac{\eta_{ss}}{\eta_{ps}}$. As we noted earlier, for a material with a horizontal easy-shear direction $\eta_{ss} < \eta_{ps}$, and thus $\delta < 1$, while for a material with a dipping easy-shear direction $\eta_{ss} > \eta_{ps}$ and $\delta > 1$. The eigenvalues of the matrix $\mathbf{A}$ are used in the expression for the propagator matrix and control the behavior of the velocities and stresses in the medium. For an isotropic material, these eigenvalues are real and repeated, and the propagator matrix includes additional terms depending linearly on the depth — $P \propto (1 \pm kz)e^{\pm kz}$ (Hager and O'Connell, 1981). The anisotropic $\mathbf{A}$ matrix has, on the other hand, four distinct eigenvalues, of the form:

$$\lambda_i = \pm k \left(\frac{2 - \delta \pm 2\sqrt{1 - \delta}}{\delta} \right)^{\frac{1}{2}} \tag{A9}$$

All the eigenvalues for a material with horizontal fabric ($\delta < 1$) are real, leading to a propagator matrix (and thus velocities and stresses) that are proportional to $e^{\pm \lambda_i z}$. Anisotropy with a 45° dipping easy-shear direction ($\delta > 1$) implies that the four eigenvalues are complex, and thus the velocities and stresses are proportional to $\cos(Im(\lambda_i)z)e^{\pm Re(\lambda_i)z}$ and $\sin(Im(\lambda_i)z)e^{\pm Re(\lambda_i)z}$. This gives rise to a non-monotonic behavior of the velocity and stress fields with depth for dipping anisotropy, plotted in Figure 3-1. This oscillatory behavior is strongly enhanced when both the dense layer and the buoyant half-space underneath have an anisotropic, dipping fabric. The growth-rate curves for this case are given in Figure A1; the non-monotonic fluctuations are obvious, especially as δ becomes larger.

Figures

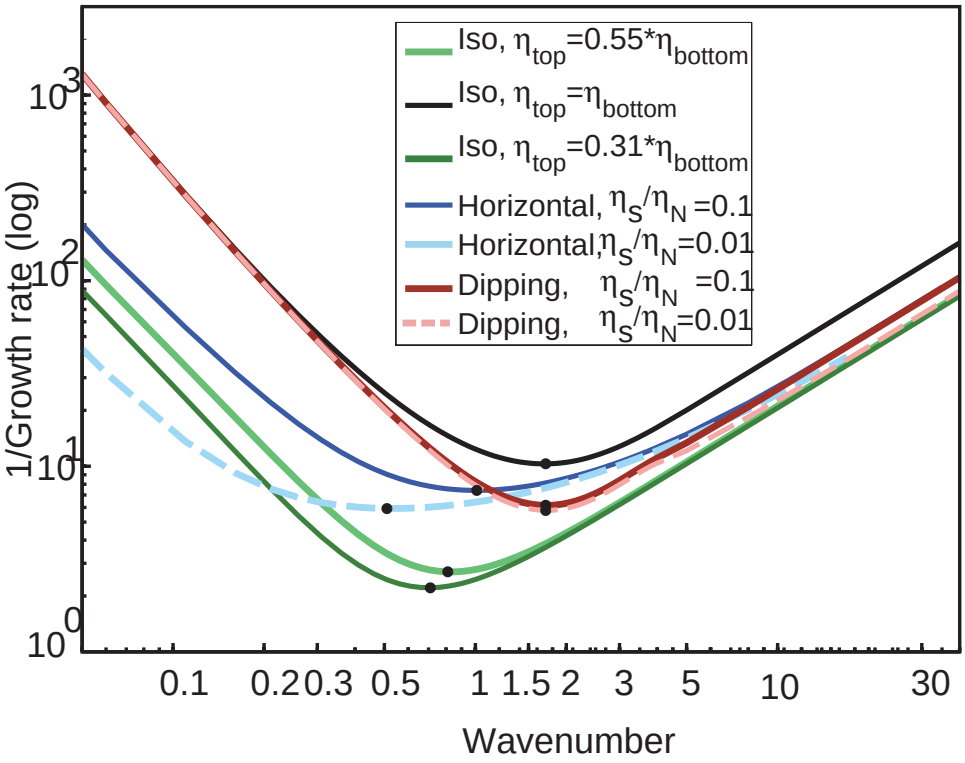

Figure 3-1: Growth-rate curves, plotting the growth rate of Rayleigh-Taylor instabilities versus the perturbation wave number, for models with varying degrees and orientations of anisotropy of a dense upper layer overlaying an isotropic half-space: black - isotropic upper layer with viscosity equal to the viscosity of the bottom half-space; green curves - isotropic dense layer with viscosity equal to the average of the normal and shear viscosities of the anisotropic cases (dark green - geometric average, light green - arithmetic average); blue curves - horizontal easy shear direction (dark blue - $\eta_s/\eta_N = 0.1$, dashed light blue - $\eta_s/\eta_N = 0.01$); red curves - easy shear direction dipping at 45° (maroon - $\eta_s/\eta_N = 0.1$, dashed pink - $\eta_s/\eta_N = 0.01$). For the anisotropic cases, $\eta_N = \eta_{bottom}$. The minimum point of each curve, indicating the most unstable wave number for each configuration, is also shown.

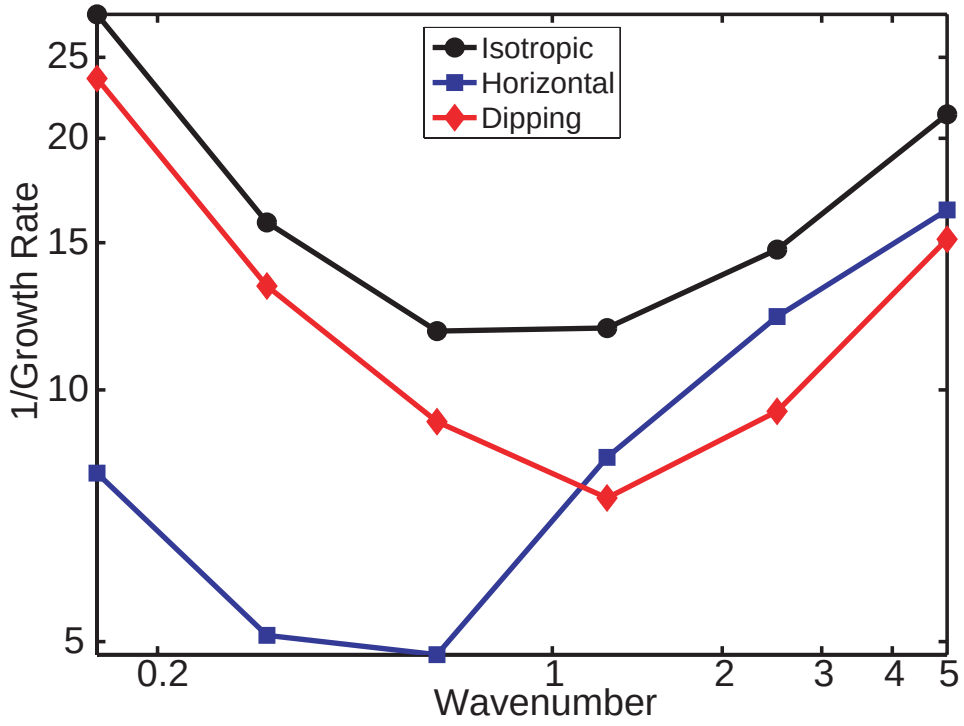

Figure 3-2: Growth-rate curves, plotting the non-dimensional growth rate versus perturbation wave number, for numerical experiments in which the anisotropic dense layer initially has a horizontal easy shear direction (blue line), a dipping easy shear direction (red line), or is isotropic (black line). The thickness of the dense layer is 0.15 of the box depth.

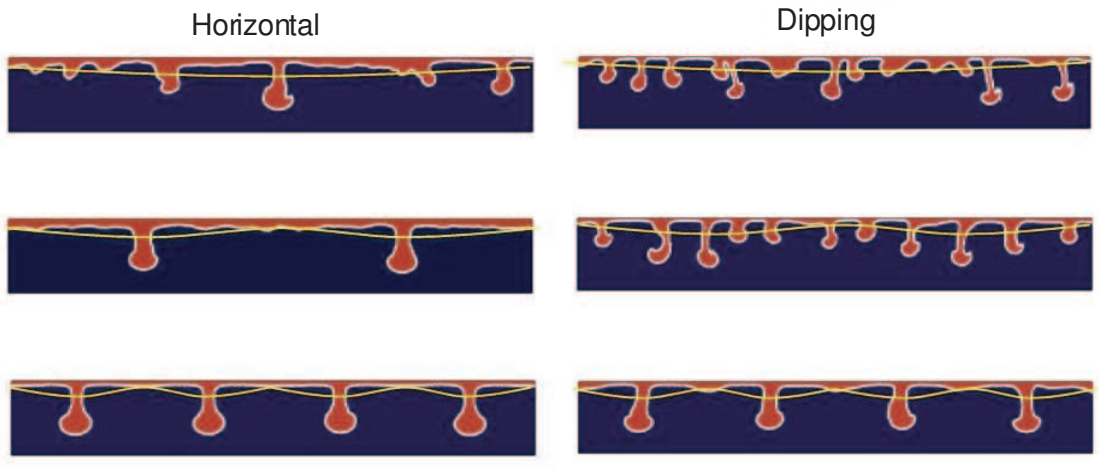

Figure 3-3: Material distribution for models with horizontal (left panels) and dipping (right panels) initial fabric of the dense top layer and various initial interface deflection wavelengths, taken after the fastest downwellings sink past half the box depth. Color denotes the materials - blue is the isotropic buoyant material and red is the anisotropic denser material. The yellow curves show the approximate location of the initial density interface, exaggerated vertically for visual clarity.

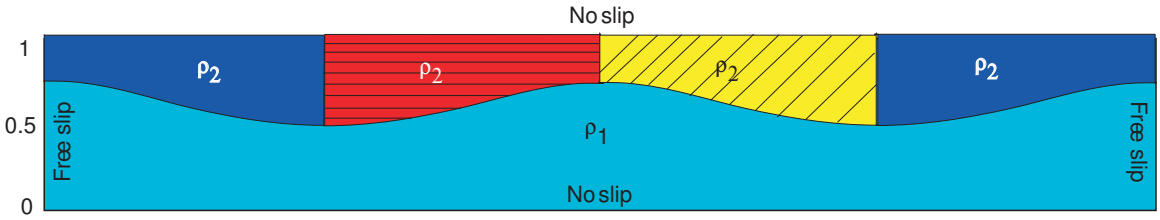

Figure 3-4: Laterally-varying anisotropy – a schematic description of the model geometry and initial conditions. The colors denote the densities and rheologies : blue - isotropic, $\rho = 1$, $\eta_{iso} = 1$, red - anisotropic with horizontal fabric, $\rho = 1$, $\delta = 0.1$, yellow - anisotropic with dipping fabric, $\rho = 1$, $\delta = 10$, cyan - isotropic, $\rho = 0$, $\eta_{iso} = 1$). There is no slip on the top and bottom boundaries, and free slip is allowed along the side walls. The thickness of the top layer and the amplitude of the interface perturbation were exaggerated for clarity.

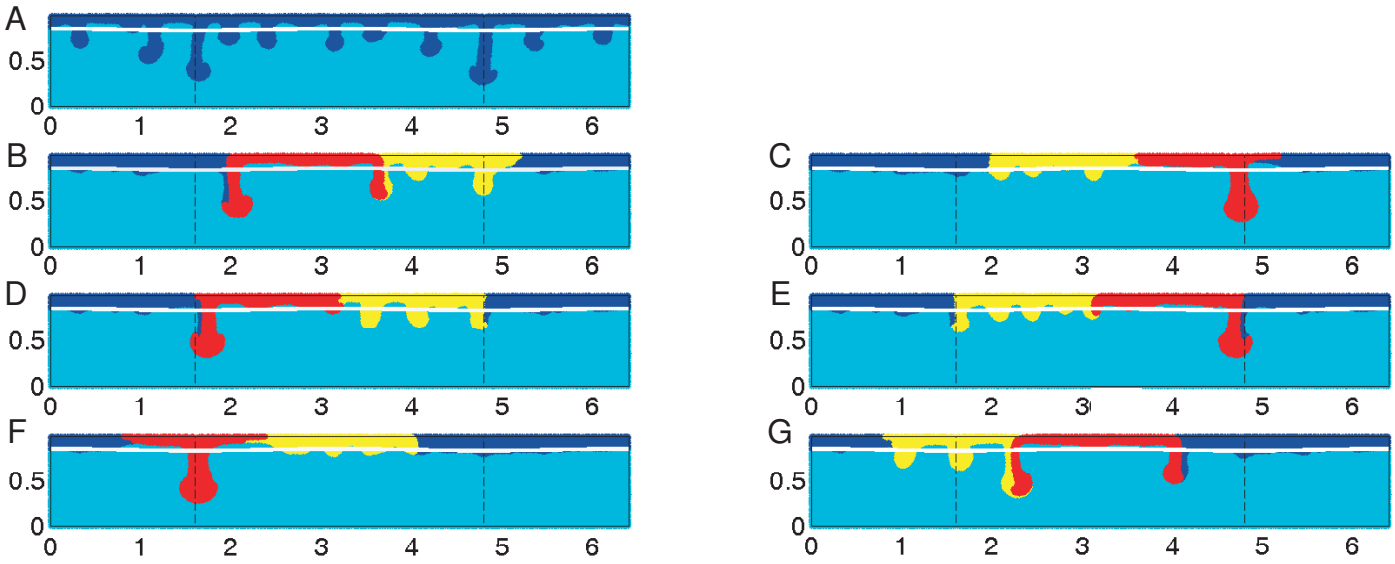

Figure 3-5: Material distribution in models with different configurations of initial anisotropic fabric taken after the fastest downwelling sinks over half the box depth. Panel A shows the results for an isotropic model. The black cosine curve at a depth of 0.15 marks the original interface between the dense and buoyant layers. The vertical dashed black lines show the deepest points of the original density interface, where the dense layer was thickest. Red material starts with a horizontal fabric; Yellow material starts with a fabric dipping at 45°. Blue materials are isotropic. Interestingly both panels 3-5B and 3-5G, which start with distinctly different material arrangements, show large downwellings comprised of both anisotropic materials, while others do not.

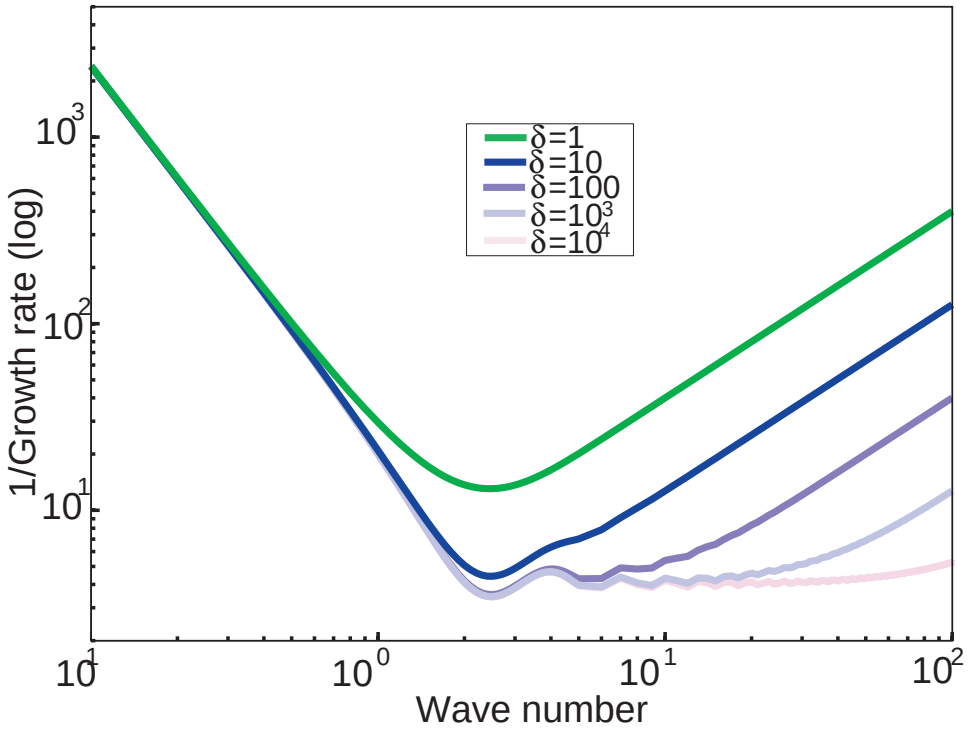

Figure A1.

Figure 3-1: Growth-rate curves, plotting the growth rate of Rayleigh-Taylor instabilities versus the perturbation wave number, for models of an anisotropic dense upper layer overlaying an anisotropic half-space, both with a dipping easy-shear direction. The colors denote different degrees of anisotropy: green - isotropic materials; blue to pink - increasing degrees of viscosity contrast between the shear and normal viscosities. The oscillatory behavior, characteristic of materials with dipping easy-shear directions, is apparent. As the viscosity contrast increases, the curves flatten for short wavelength.

Chapter 4

Anisotropic viscosity changes the thermal structure of the mantle wedge at subduction zones

4.1 Abstract

We examine the effect of anisotropic viscosity on the thermal structure of subduction zone mantle wedges. Abundant observations of seismic anisotropy in subduction zones suggest that the material in the mantle wedge has a strong fabric and may be mechanically anisotropic. Using two-dimensional (2D) finite-element kinematic models we find that anisotropic viscosity causes several substantial changes: (1) a hotter slab-wedge interface, (2) a smaller partially molten region, (3) time-variability of the melt production rate and excess temperatures, and (4) a much larger region of the wedge is deforming dominantly by dislocation creep.

A hotter slab-wedge interface can change the depth extent of the seismogenic zone, limit the depth to which hydrous minerals can carry water, and influence flux melting. Heterogeneity in material alignment can cause temporal changes in subduction zone magmatism

[0]In revision as: Lev, E. and B.H. Hager, Anisotropic viscosity changes the thermal structure and melt distribution in subduction zone mantle wedges, Geophys. Res. Lett.

without invoking a change in the wedge geometry, slab age or composition. We therefore recommend that anisotropic viscosity, as well as time-dependence, be considered in future models of wedge thermal structure.

4.2 Introduction

Observational constraints on the thermal structure of mantle wedges come mainly from petrology, which looks at the distribution and composition of arc magmas, and from seismic studies examining seismic velocities, phase conversions and attenuation in the wedge. Most arcs include a zone of low seismic velocity that connects the slab-wedge interface between 150 and 200 km depth to the volcanic front or back-arc basins (e.g. Iwamori and Zhao, 2000). High attenuation regions below the volcanic front which are generally in good agreement with regions of low seismic velocities (e.g. Flanagan and Wiens, 1994; Takenami et al., 2000). van Keken (2003) and Wiens and Conder (2008) summarize many different constraints on the thermal structure of subduction zones.

The thermal structure of the mantle wedge in subduction zones controls the distribution of melting and dehydration reactions. Physical parameters such as subduction geometry, velocity, and mantle rheology influence the thermal structure of wedges. For example, Peacock and Wang (1999) demonstrated that the differences in wedge temperatures, resulting from a colder slab subducting under NE Japan (compared to SW Japan), can be the source for differences volcanism in the Holocene. We focus here on the effect of anisotropic viscosity.

Extensive modeling work has previously shown how the assumed rheology of the mantle wedge changes observables such as dynamic topography (e.g. Gurnis, 1993; Billen et al., 2003a), seismic anisotropy (Long et al., 2007; Kneller et al., 2008), slab stagnation (Riedel and Karato, 1997; Torii and Yoshioka, 2007), post-seismic deformation (Katagi et al., 2008), deep earthquakes (Karato et al., 2001) and general dynamic behavior (e.g Kemp, 1992; Stein et al., 2004). Kelemen et al. (2003) proved that the temperature dependence of viscosity must be included in models of the mantle wedge in order to match the petrological properties of arc magmas. We demonstrate here that anisotropic viscosity, a factor likely very relevant

to the mantle, affects the outcome of our SUZs models by changing the flow in the mantle wedge and altering the thermal structure of the wedge.

Many subduction zones around the world exhibit strong seismic anisotropy, commonly attributed to the alignment of anisotropic minerals by flow in the mantle wedge or below the subducting slab (Savage, 1999; Hall et al., 2000; Long and Silver, 2008). An alternative source of seismic anisotropy is the alignment of melt inclusions or fluid-filled lenses (Holtzman et al., 2003). The abundance of observations of seismic anisotropy in subduction zones clearly indicates strong preferred orientation of minerals and heterogeneities on various length scales. The presence of these strong fabrics raises the question: how does the mechanical anisotropy associated with these strong fabrics influence the flow and resulting phenomena such as magmatism, in the mantle wedge?

Many minerals have inherent plastic anisotropy, a result of differences between the stresses required for slip along the different slip systems available for accommodating deformation at the crystal level. Olivine, the main constituent of Earth's upper mantle, is an example. Olivine deforms at least 10 times faster when its easy slip system (slip in the a direction in the b plane, or (010)[100]) is aligned with the direction of shear compared to less favorable orientations, which force activation of harder slip systems (e.g. Durham and Goetze, 1977; Drury et al., 1991). Alignment of weak phases such as melt or fluids can result in over an order of magnitude difference in the viscosity if shearing occurs parallel rather than in the direction orthogonal to the layers (e.g. Treagus, 2003).

The influence of anisotropic viscosity on geodynamical flows has been demonstrated in the past for thermal instabilities (Richter and Daly, 1978), thermal convection (Saito and Abe, 1984; Honda, 1986; Christensen, 1987), post-glacial rebound (Christensen, 1987; Wahr and Han, 1997), oceanic plate dynamics (Hearn et al., 1997) and lithospheric instabilities (Lev and Hager, 2008a). Here we address the case of subduction by describing results from a set of numerical experiments where subduction is driven kinematically. We find that anisotropic viscosity in the mantle wedge changes its thermal structure, leading to higher temperatures at the slab-wedge interface, a decrease in melt production, and time variability in the melting behavior.

4.3 Modeling methodology

Our subduction models are kinematic – the slab is driven by a constant velocity boundary condition. This boundary condition drives flow in the wedge between the slab and the stagnant overriding plate. Buoyancy is not included in our calculation. We constructed two models: one with isotropic viscosity in the mantle wedge material (IM hereafter), and one with anisotropic viscosity (AM hereafter). We calculate the flow and the temperature fields in the wedge in both configurations and compare the results. Our model design is similar to that used for the kinematic subduction community benchmark (van Keken et al., 2008) and those used by van Keken et al. (2002) and Kelemen et al. (2003).

4.3.1 Model setup and solution

Our model is confined in a 300 by 600 km box, discretized as a 256 by 128 regular finite-element grid (a resolution of 2.3 km per element). See Figure 4-1 for model setup and boundary conditions. The slab is kept at 45° dip and moves at a constant velocity of 100 mm/yr. The top of the overriding plate is held fixed. To avoid singularity at the wedge corner, we followed the technique used by van Keken et al. (2008) and added a small (15 km wide) rigid "nose" at the wedge tip and a short ramp of a linear increase in velocity immediately below the rigid nose.

The initial thermal profile in our models is an error function solution. The surface is kept at $0°C$ and the interior at $1380°C$. The top thermal boundary layer is 80 km thick, representing a 40 Myr old lithosphere. The sides of the box keep the error function profile as a boundary condition. Thus, slab material entering the box through the right-hand side has an error function profile as well.

We use a non-Newtonian viscosity with a stress exponent $n = 3.4$ (Hirth, 2002). While in early experiments we found, in agreement with Long et al. (2007), that the effect of including non-Newtonian viscosity on the flow fieldswas small, we include it for consistency: LPO developments requires deformation in the dislocation creep regime, which implies a power-law rheology. We also account for the dependence of viscosity on temperature, which

was shown to be crucial in similar kinematic models (Kelemen et al., 2003). We use an Arhenius relationship for the viscosity:

$$\eta = \left(\eta_0 e^{\frac{E^*}{RT}}\right)^{\frac{1}{n}} \times (2\dot{\epsilon})^{\frac{1-n}{n}} \tag{A0}$$

where η_0 is a reference viscosity, $E*$ is the activation energy, n is the power-law flow exponent which we take to be 3.4, R is the gas constant, T is the temperature in Kelvin, and $\dot{\epsilon}$ is the strain rate. The activation energy E^* is taken to be 480 KJ mol^{-1}, which is within the range of values reported by Hirth and Kohlstedt (2003), and gives a viscosity contrast of 4 orders of magnitude across the top thermal boundary layer. We solve the equations of conservation of mass, momentum and energy using the finite-element code *Underworld* (Moresi et al., 2007), which includes a formulation for anisotropic viscosity. We use a transverse isotropy symmetry for the viscosity of the material in the mantle wedge, corresponding to a rheology with one dominant easy glide plane. While this symmetry is not fully equivalent to the symmetry of mantle constituent minerals such as the orthorhombic olivine, in 2D this suffices. We use a ratio of 1:10 between the shear and the normal viscosities, in agreement with estimates for rocks and mantle minerals (Durham and Goetze, 1977; Castelnau et al., 2008).

The fabric we use for the anisotropic viscosity calculations is coupled with the flow. We track a set of over 1.6 million directors (oriented particles) distributed evenly throughout the mantle wedge. The directors represent normals to the plane of easy shear, and are rotated and stretched by the flow. New particles entering the model domain through the in-flow boundaries have random orientations. The orientation of the directors evolves according to the method described by Mühlhaus et al. (2002b).

4.3.2 Calculation of melt production

After solving for velocities and temperature evolution over time, we post-process the results and calculate the amount of partial melting predicted by the temperature field. We use the

parameterized solidus for anhydrous peridotite of Till et al. (2009):

$$T_s(P) = -3.3313P^2 + 104.05P + 1200 \quad \text{(A0)}$$

where T_s is the solidus temperature in $^\circ C$ at a pressure P given in GPa. We assume a lithostatic pressure $P = \rho g h$ with $\rho = 3300\ kg/m^3$. We only calculate partial melting at depths shallower than 200 km (6.5 GPa), since the solidus is not as well-constrained below that depth. For each model we calculate four quantities:

1. The total wedge area that has reached above-solidus temperature

2. The melt production rate (per trench length unit), calculated by multiplying the flux of material into the melting zone by excess temperature of each element times the factor 0.15 $wt\%/^\circ K$ (Elkins-Tanton and Hager, 2005)

3. The temperature at the center of the wedge thermal nose

4. The average excess temperature within the above-solidus region (a proxy for average melt fraction). Figure 4-2 summarizes the measured values.

We follow a similar scheme for flux melting, triggered by the release of water from hydrous minerals at the slab-wedge interface. We combine the parameterized Chlorite stability curve:

$$T_{cl} = -32P^2 + 155P + 688 \quad \text{(A0)}$$

and the vapor-saturated peridotite solidus:

$$T_s(P) = 1.9372P^4 - 28.396P^3 + 152.3P^2 - 374.3P + 1200 \quad \text{(A0)}$$

defined by Grove et al. (2006) and Till et al. (2009). Our flux-melting region is defined as locations warmer than the vapor-saturated solidus and colder than the chlorite breakdown temperature, similar to the technique used by Grove et al. (2009).

4.3.3 Deformation mechanisms partitioning

The two main mechanisms for deformation in the upper mantle are diffusion creep, which is Newtonian, and dislocation creep, which has a power-law dependence of strain-rate on stress. While we use only a power-law rheology for the wedge material, we use the resulting thermal structure to estimate the spatial extent of the regions dominated by each of these mechanisms in the mantle wedge. This estimation is important for our discussion of subduction zone anisotropy, as anisotropy is commonly thought to require deformation by dislocation creep. As a post-processing step, we calculate for each position in the wedge the viscosity arising from the local temperature, pressure and strain rate conditions. We use the constitutive relations and constants reported by Hirth and Kohlstedt (2003), for a grain sizes of 3mm, to investigate the influence of anisotropic viscosity on the partitioning of deformation mechanisms in the wedge.

4.4 Results and Discussion

We compare the thermal structure of a wedge with isotropic viscosity to that of a wedge with anisotropic viscosity by plotting the difference in temperature throughout the wedge (Figure 4-3). A clear difference between the fields is the much warmer – up to $200°C$ – slab-wedge interface in the AM. The AM is also warmer immediately beneath where a volcanic arc may be located. Warmer temperatures there may lead to higher heat flow, perhaps promoting secondary volcanism and back-arc spreading. The warmer regions result from the anisotropic viscosity and the strong alignment, which change the flow geometry by making it difficult to make the sharp turn at the wedge corner and by focusing the flow to a narrow layer thanks to the alignment of easy flow direction with the slab. The stream lines are then forced to make a wider turn around the wedge corner, pushing the isotherms away from the wedge tip so that the tip becomes colder. Further down-dip the isotherms are pushed closer against the slab, leading to a higher heat flow and warmer temperatures. The high strain rates along the shallow part of the slab-wedge interface (Figure 4-4) are an expression of this focusing of the flow.

The temperature difference between the two models at the center of the wedge is about 50 degrees (Figure 4-3). According to the relationship between temperature and attenuation given by Jackson et al. (1992):

$$Q^{-1}(T) = 5 \times 10^5 \exp[(-201kJ/mol)/RT] \tag{A0}$$

this difference in temperature can lead to a difference of 0.7% in Q^{-1}.

Our melt calculations clearly reveal the smaller melting region in the AM (Figure 4-2A and Figure 4-3). The total area that reaches above-solidus temperatures in the anisotropic model is smaller than in the isotropic model (Figure 4-2 A). Additionally, the overall average excess temperature within the melting region in the AM is lower (Figure 4-2D). The largest difference between the models is about three degrees, which may result in $0.3 * 3 = 0.9\ wt\%$ difference for batch melting (Elkins-Tanton and Hager, 2005). Such a small difference in melt fraction is probably too small to be detected by tools such as seismic attenuation (Berckhemer et al., 1982; Gribb and Cooper, 2000; Schmeling, 1985; Hammond and Humphreys, 2000).

This difference may be detected with tools such as observations of seismic attenuation.

Our calculated melt production rates (MPR) (Figure 4-2) are within the range of observations at modern subduction zones. The agreement in MPR is somewhat better for the AM. The MPR in the IM stabilizes at around 150 $km^3Ma^{-1}(\text{arc km})^{-1}$. The MPR in the AM varies over time, between 10 and 55 $km^3Ma^{-1}(\text{arc km})^{-1}$. MPR estimates for the Aleutians are 67 $km^3\ Ma^{-1}\ (\text{arc km})^{-1}$ (Holbrook et al., 1999; Lizarralde et al., 2002), and between 30 $km^3Ma^{-1}(\text{arc km})^{-1}$ (Reymer and Schubert, 1984) and 80 $km^3Ma^{-1}(\text{arc km})^{-1}$ (Taira et al., 2004) for Izu-Bonin. Although the MPR in the IM appears too high, our rates directly depend on the prescribed potential temperature, which we set to $1380°C$. The potential temperature of the mantle is not very well constrained, though, and estimates range between $1315°C$ (McKenzie et al., 2005) and $1450°C$ (Anderson, 2000). While there are many other factors that influence melt fluxes in subduction zones, we present this calculation to demonstrate the influence of the anisotropic viscosity.

One result of the AM is a strong time variability of all the thermal parameters measured (Figure 4-2, dashed red lines), as opposed to generally constant values in the IM (solid

blue lines). A characteristic transition period is between 3 and 5 Myrs. The source of the time variability in the AM is the heterogeneity in effective viscosity of the material flowing along the bottom of the overriding plate, caused by incomplete alignment of the anisotropic material. This heterogeneity leads to a noisier velocity field and, consequently, to a noisier thermal field.

An inherent part of our modeling technique is the tracking of the evolution of preferred orientations in the mantle wedge in great detail. Previous models have either used simplified techniques such as the tracking of finite-strain ellipses (Hall et al., 2000; Long et al., 2007), or limited their LPO modeling to a small region within the mantle wedge (Kneller et al., 2008). The LPO field resulting from our models, shown in Figure 4-5, is in general agreement with previous approximations (e.g. Long et al., 2007). It demonstrates that the strongest fabric resides immediately above the slab and below the overriding lithospheric lid, and that the fabric in the center of the wedge is weak. This information is useful for locating the source of anisotropic signals measured at SUZs by seismic techniques. The concentration of aligned material in the two boundary layers leaves the center of the wedge poorly aligned.

The anisotropy arising from the concentration of highly aligned material along the boundary layers between the wedge and the overriding plate or subducting slab will, in nature, be enhanced by the dominance of dislocation creep in the deformation of these regions. The anisotropic viscosity, in turn, encourages the deformation by dislocation creep through larger areas compared with isotropic viscosity, by keeping the core of the wedge cooler. This phenomena is demonstrated in Figure 4-6, where we plot and compare the spatial extent of mechanism partitioning for anisotropic and isotropic cases for two grain sizes. Therefore, our results point out an interesting positive feedback between deformation mechanism partitioning, anisotropy and flow in the wedge. Our findings put into question the validity of the conclusion of Katayama (2009), who used a thermal model obtained using isotropic viscosity to conclude that dislocation creep is confined to a thin layer along the top of the slab.

4.5 Future directions

As we mentioned in the introduction, anisotropic viscosity can arise from a variety of physical mechanisms. The degree of anisotropy, expressed in our models by the viscosity ratio parameter δ, may differ between mechanisms and sources. It will be interesting to examine models with a range of values for δ. In addition, the material entering the model box is assumed to have no prior alignment. In the mantle, this might not be the case, as mantle material flowing into a subduction wedge from underneath the overriding lithosphere may already have obtained an alignment. Possible influences of pre-existing fabric in the incoming material include suppressing of the time variability and enhancing the change in flow geometry around the wedge nose.

Our models are kinematic, driven solely by the velocity prescribed to the sinking slab. In this setup, the influence of anisotropic viscosity in the dynamics of the flow might be limited, similar to the limited effect a power-law viscosity has on kinematic models compared to dynamic models (compare, e.g., van Keken et al. (2008) with Billen et al. (2003b)). Our preliminary results from dynamic subduction models that account for anisotropic viscosity show drastic changes in slab rollback patterns, slab stagnation in the transition zone, and slab folding and buckling at viscosity interfaces (Lev and Hager, 2007). These promising models should be extended to include a realistic rheology for the upper mantle, including composition of multiple deformation mechanisms, depth dependence and grain-size evolution.

4.6 Summary

We include anisotropic viscosity in thermal kinematic models of subduction zone wedge flow. Our models have temperature-dependent viscosity, essential for getting dry melting in the wedge. Anisotropic viscosity leads to significant changes compared to an isotropic model – the slab-wedge interface becomes hotter, the partially-molten area is smaller, and the melt production rate and excess temperatures are lower and vary with time. The reason for the time-variability is fluctuation in the velocity field caused by the anisotropic viscosity. This time variability is on relatively short time scales and may provide an explanation for observed

time variations in melt extent without requiring large changes in subduction geometry or rate. The cooler center of the wedge in the anisotropic models leads to widening of the area of the wedge deforming dominantly by dislocation creep, enhancing the development of anisotropy. We conclude that anisotropic viscosity and the effective viscosity heterogeneity play an important role in determining the thermal structure of the mantle wedge and the melt produced in it.

4.7 Acknowledgements

The research presented here was supported by NSF grant EAR-0409564. The authors are grateful for advice from Christy Till, Tim Grove, Lindy Elkins-Tanton, Maureen Long, Greg Hirth, Phil Skemer, Peter van Keken and Mark Behn.

Figures

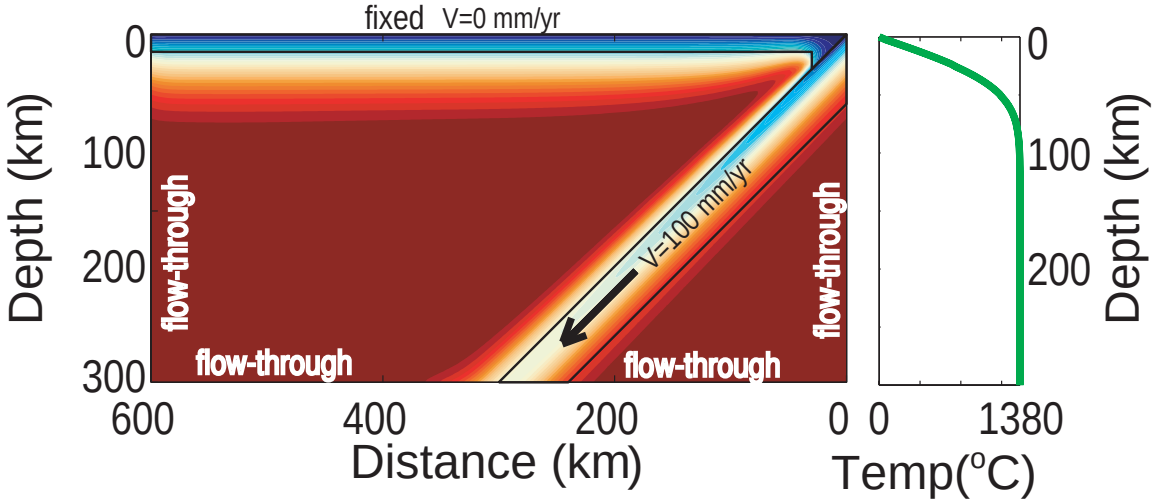

Figure 4-1: Model geometry, initial and boundary conditions. Background – the temperature distribution after the model reaches a steady-state. Right side panel – the temperature profile used as a boundary condition along the side walls. This is the profile throughout the box width at time=0.

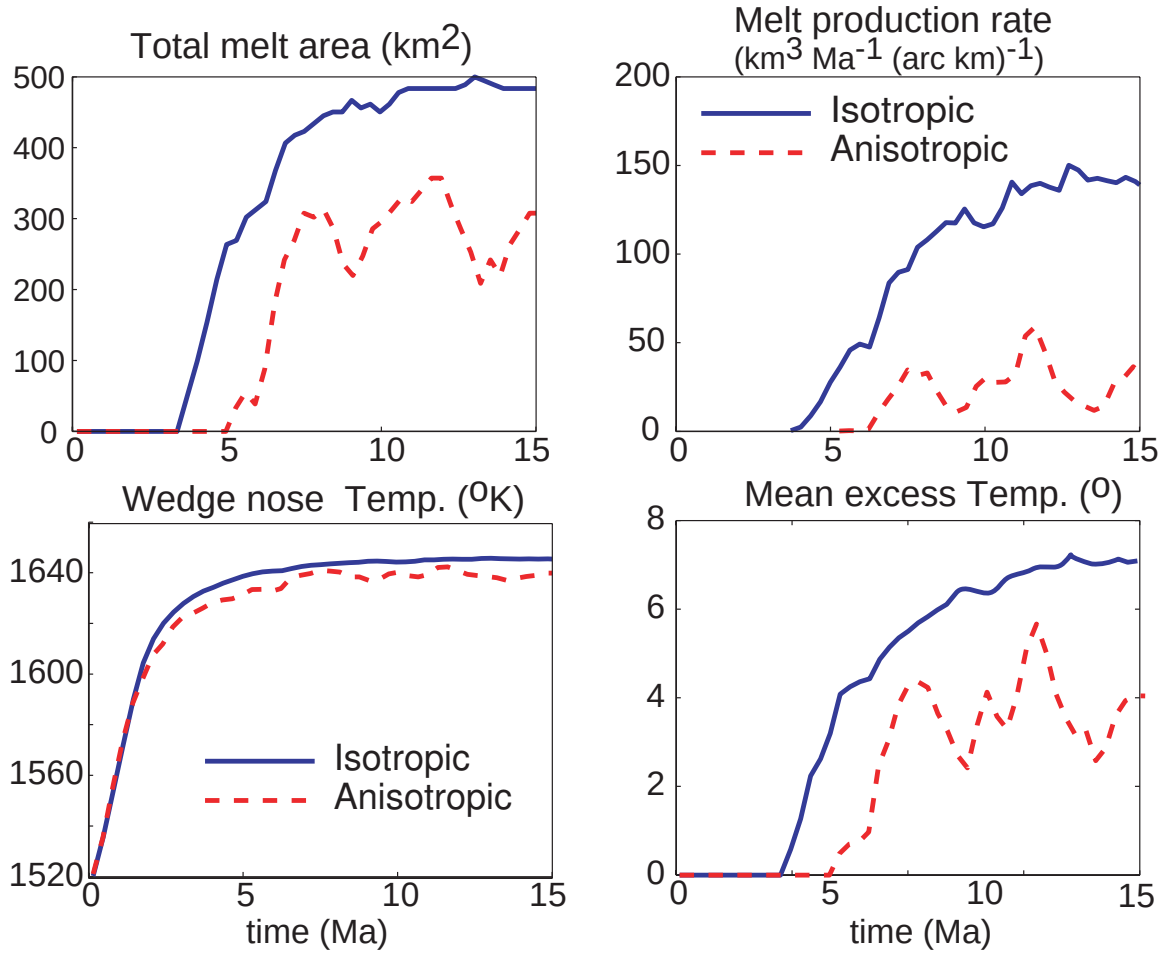

Figure 4-2: A comparison of thermal quantities from the isotropic (solid blue line) and anisotropic (dashed red line) models.

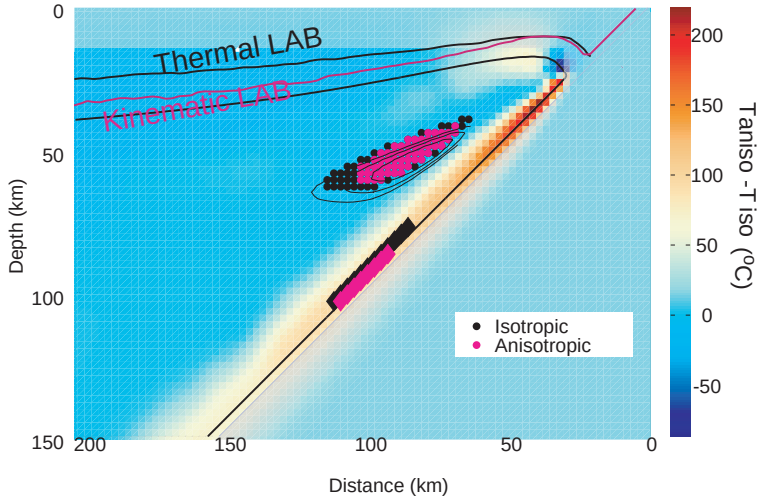

Figure 4-3: A comparison of the thermal fields and resulting melting regions for the isotropic and anisotropic models. The background color shows the difference in temperature (T_{aniso}-T_{iso}) at t=15 Ma. Circles mark elements that reach temperatures above the dry solidus (black=isotropic, pink=anisotropic). Diamonds along the slab interface show regions prone to wet melting – warmer than the vapor-saturated solidus but colder but still within the chlorite stability field. The solid curves show the boundary between the overriding lithosphere and the mantle wedge. The black line is a thermal definition of the lithosphere-asthenosphere boundary, using $T_{LAB} = 0.7T_{max}$. The pink line is a based on a mechanical definition of the LAB, marking the line of strain rate= $10^{-14}sec^{-1}$.

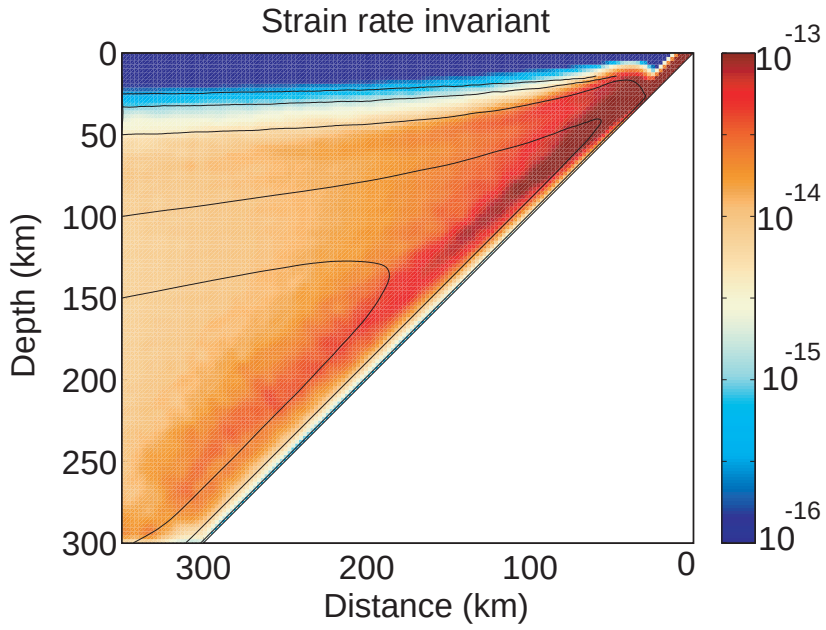

Figure 4-4: The background color shows the second invariant of the strain rate within the mantle wedge. As expected, the strain rate is low in the cold, stiff regions of the overriding plate and the subducting slab. The highest strain rates are in a narrow band the top of the slab, extending from the wedge corner to a depth of about 150 km. This strain field was obtained from a model with an anisotropic viscosity.

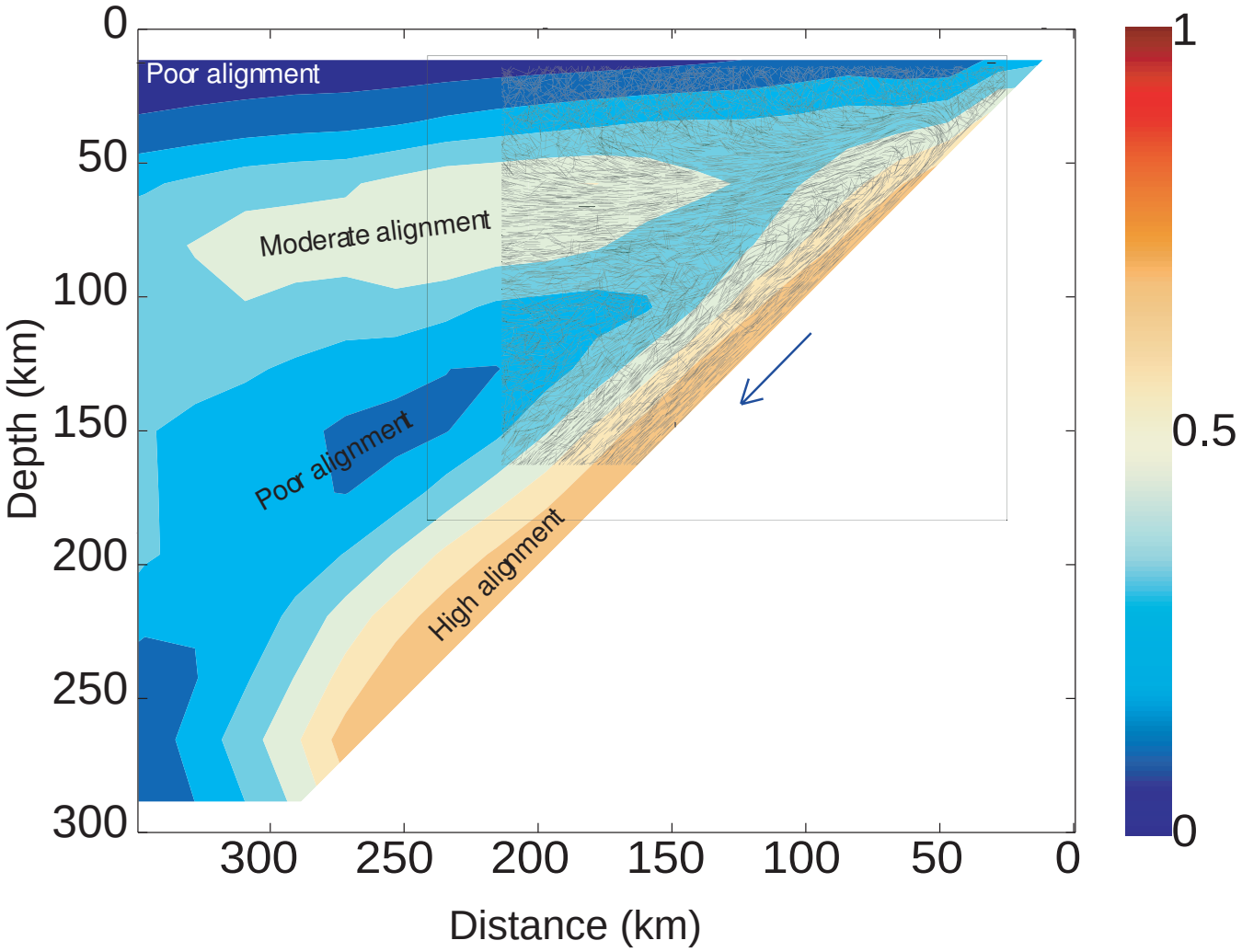

Figure 4-5: Directions and strength of the LPO that develops in the mantle wedge. The black sticks represent the orientation of olivine a-axis. The background color shows LPO saturation through misorientation index, indicating a region of high alignment adjacent to the slab-wedge interface, a moderate alignment region at the bottom of the overriding plate, and a poor alignment region at the core of the wedge.

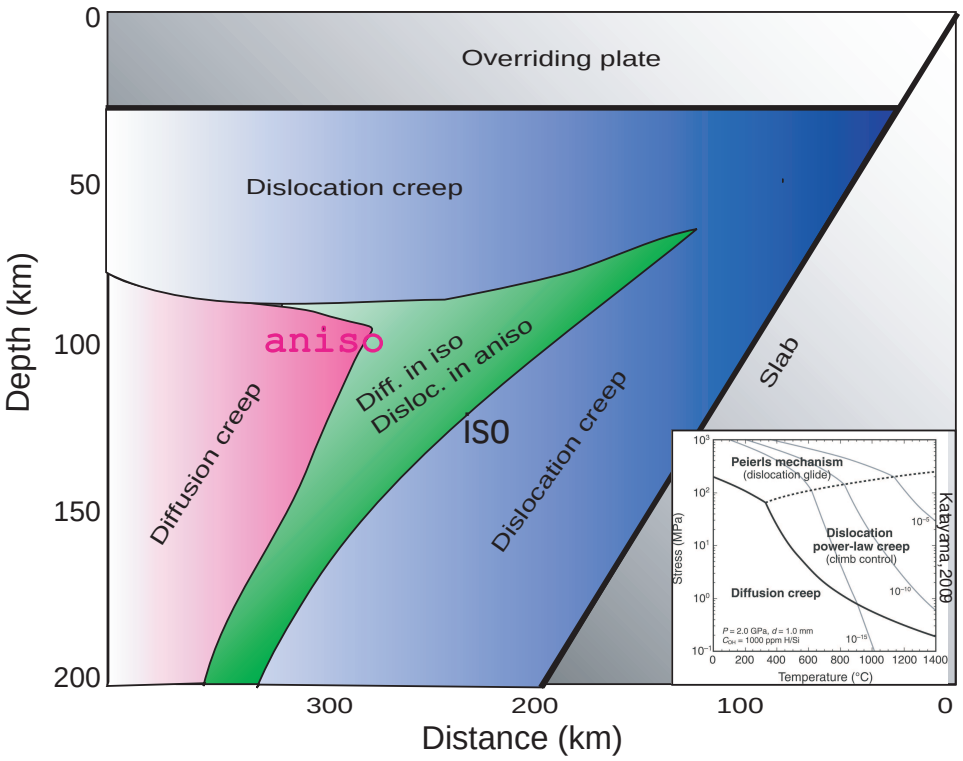

Figure 4-6: Influence of anisotropic viscosity on the spatial partitioning of deformation mechanism in the wedge. Plotted is the extent of areas where the deformation is dominated by dislocation power-law creep and areas dominated by diffusion creep, given a grain size of 3mm. The boundary between the deformation regimes was calculated using the equations and constants given by Hirth and Kohlstedt (2003) and the method described by Katayama (2009). The blue are is dominated by dislocation creep in both the isotropic and anisotropic models. The pink region is dominated by diffusion creep in both models. The green region is dominated by dislocation creep in the anisotropic model but by diffusion creep in the isotropic model. There is therefore a change of over 200km in the position of the boundary between the two deformation mechanisms depending on the anisotropy. The inset is the deformation map given by Katayama (2009), which we employ here too.

Chapter 5

Influence of grain size and anisotropic viscosity on the development of an anisotropic layer in the upper mantle

Abstract

The degree of anisotropic viscosity and the grain size of upper mantle minerals are two important rheological parameters that are generally poorly constrained. We use numerical models of asthenospheric flow to determine the grain size and anisotropic viscosity required to explain the observed confinement of seismic anisotropy to a layer at the top of the convecting upper mantle. We find that a grain size larger than 10 mm gives the best fit to the observations. The ratio of shear viscosity to normal viscosity is 0.3 or more, depending on grain size.

5.1 Introduction

Seismic anisotropy is the direction-dependence of seismic wave speeds. In the upper mantle below the oceans, radial seismic anisotropy appears to be confined within a layer extending from the base of the lithosphere to a depth of about 200 km (Dziewonski and Anderson, 1981; Gung et al., 2003; Smith et al., 2004; Beghein et al., 2006). The maximum anisotropy under the oceans is observed at a depth of about 120 km (Debayle et al., 2005; Nettles and Dziewonski, 2008), which is approximately 45 km below the 'Gutenberg discontinuity',

sometimes identified as the base of the lithosphere (Revenaugh and Jordan, 1991). If plate motion relative to the lower mantle is shearing the entire upper mantle, one would expect the anisotropy to extend further down, perhaps as far down as the olivine-spinel phase transition. The observation that the anisotropy is, instead, confined to the topmost part of the convecting mantle seems to require special conditions. We propose that a grain-size dependent and anisotropic composite rheology play an important role.

Strain in the mantle partitions among various microscopic deformation mechanisms by which mantle rocks deform. Laboratory studies on the deformation of olivine point to two main deformation mechanisms in action in the Earth's upper mantle: diffusion creep and dislocation creep (see Drury and FitzGerlad (2000) for a review). Diffusion creep (also knows as Cobble creep) takes place by the diffusion of atoms and vacancies primarily along grain boundaries. Diffusion creep is also sometimes referred to as "grain-size sensitive" creep, due to the strong dependence of the viscosity on grain size ($\eta \propto d^3$). Dislocation creep involves slip along a finite number of crystallographic glide planes and directions. "Power-law creep" is an alternative name for dislocation creep, emphasizing the strong dependence of the strain rate on the applied stress ($\dot{\varepsilon} \propto \sigma^{\sim 3.5}$). The development of lattice preferred orientation (LPO) is usually considered to require deformation by dislocation creep (e.g. Karato et al., 1995; Fliervoet and Drury, 1999; Warren and Hirth, 2006).

Preferred orientation leads to anisotropy not only of seismic wave speeds but also of material strength. Anisotropic viscosity has been shown to change flow in a range of mantle dynamics scenarios, from thermal convection (Richter and Daly, 1978; Moresi et al., 2003), Rayleigh-Taylor instabilities (Lev and Hager, 2008a) to continental break-up (Vauchez et al., 1997). Still, the strength of mechanical anisotropy in the mantle is poorly constrained. Using laboratory experiments, Durham and Goetze (1977) showed that the strain rate of creeping olivine with preexisting fabric depends on the orientation of the sample and can vary by up to a factor of 50. This is because the orientation of the sample relative to the applied stress determines which slip systems are activated. In the experiments of Bai and Kohlstedt (1992) on high-temperature creep of olivine, and those of Wendt et al. (1998) on peridotites, the measured strain rate depended strongly on the relative orientation of the applied stress to

the sample crystallographic axis. The effect of shape-preferred orientations on the strength in a deformed two-phase composite material has not yet been studied experimentally, and theoretical estimations rely on simple geometrical assumptions (Weijermars, 1992; Mandal et al., 2000; Treagus, 2003).

The characteristic grain size in the upper mantle is also poorly constrained, despite the strong dependence of the rheology on it. Samples from lithospheric xenoliths and ophiolites show a fractal distribution of grain sizes, with most grains smaller than 5mm but a substantial number between 5 and 20mm. Based on modeling of dehydration and grain size evolution, Eisenbeck (2009) and Behn et al. (2009) predict that the grain size in the oceanic upper mantle at a depth of 150km should be ∼11mm. Our goal in this paper is to constrain grain size and anisotropy using seismic observations and flow models.

5.2 Methods

We construct two-dimensional models of simple shear – approximating the flow beneath a moving rigid plate and a sluggish mantle at depth. We vary the plate velocity, the grain size and the degree of anisotropic viscosity assumed for the mantle material. We then calculate the depth and the width of the shear zone that develops at the base of the plate, as well as the depth and width of the region which deforms dominantly by dislocation creep.

5.2.1 Model setup

Our model domain is a two-dimensional box extending 900 km horizontally and 300 km vertically. The depth of the box represents the part of the upper mantle extending from the base of the lithosphere at a depth of 80 km down to 380 km, just above the transition of olivine to the spinel mineral phase.

We use a composite rheology to account for the combination of the dislocation creep and the diffusion creep deformation mechanisms. The effective viscosity of the composite is defined by its two constituents:

$$\frac{1}{\eta_{effective}} = \frac{1}{\eta_{diffusion}} + \frac{1}{\eta_{dislocation}} \tag{A0}$$

The viscosities of the two components are calculated using the constitutive equation and material constants reported by Hirth and Kohlstedt (2003) for olivine with a constant water content:

$$\eta = \left[A^{-1} d^p f H_2O^{-r} \exp\left(\frac{E^* + PV^*}{RT}\right)\right]^{1/n} \times (2\dot{\varepsilon})^{\frac{1-n}{n}} \tag{A0}$$

where the $\dot{\varepsilon}$ is the strain rate, R is the gas constant, T is the absolute temperature and P is the pressure. The parameters we use are listed in table 5.1.

Definition	Symbol	Units	Diffusion creep value	Dislocation creep value
Pre-exponent constant	A	–	10^6	90
grain size	d	μ m	varied	varied
grain size exponent	p	–	3	0
water content	fH_2O	$H/10^6Si$	1000	1000
water content exponent	r	–	1	1.2
activation energy	E^*	J/mol	335000	480000
activation volume	V^*	$10^{-6}m^3/mol$	4	11
stress exponent	n	–	1	3.5

Table 5.1: Values of constants used in viscosity calculation

Both the temperature and pressure are assumed to be solely a function of the depth z, where $P(z) = \rho g z$ and $T(z)$ is calculated as:

$$T(z) = T_0 + \frac{\Delta T}{\Delta z} z \tag{A0}$$

The geothermal gradient $\frac{\Delta T}{\Delta z}$ is taken as 0.3 $^\circ/km$ (Turcotte and Schubert, 2002). The resulting upper mantle viscosity profiles are plotted in Figure 5-1.

The dislocation creep component is allowed to develop anisotropic viscosity in order to model the mechanical anisotropy of rocks with strong lattice preferred orientations. We explore a range of values for the ratio between the shear and normal viscosities $\eta_s/\eta_N \equiv \delta$,

using $\delta \in \{0.1, 0.25, 0.5, 0.75, 1\}$, with $\delta = 1$ representing isotropic viscosity. This range of ratios is supported by lab experiments (Durham and Goetze, 1977; Bai and Kohlstedt, 1992) and field observations (Warren et al., 2008). The preferred orientation develops as described in chapter 6 (Lev and Hager, 2008b). The grain sizes in the models are $d \in \{1, 2, 5, 7.5, 10, 20\} mm$.

For the calculations shown here, we apply a constant velocity boundary condition of 80 mm/yr to the bottom of the box. The top surface is held fixed. The sides are free to move horizontally but not vertically. Material can leave and enter the box through the side walls. It is important to note here that the selected plate velocity has very little effect on the results. This is a direct outcome from the constitutive laws defining dislocation and diffusion creep used here. The partitioning of strain between the two components is controlled by the non-dimensional ratio of the viscosities. Let us write the constitutive laws for the isotropic case ($\delta = 1$) as:

$$\eta^{diff} = \eta_0^{diff} \times \left(\frac{d}{d_0}\right)^p \qquad \text{and} \qquad \eta^{disl} = \eta_0^{disl} \times \left(\frac{\dot{\varepsilon}_0}{\dot{\varepsilon}}\right)^{\frac{n-1}{n}}$$

where η_0 are reference viscosities, d_0 a reference grain size and $\dot{\varepsilon}_0$ a reference strain rate. For $p = 3,\ n = 3.5$, the viscosity ratio is proportional to $\frac{d^3}{\dot{\varepsilon}^{0.7}}$, which implies that a change of an order of magnitude in the imposed velocity or strain rate is equivalent to a change of the grain size by only a factor of 1.6.

5.2.2 Numerical tools

We solve the equations of flow, expressing the conservation of mass and momentum, using the finite-element method as implemented in the public-domain software package *Underworld* (Moresi et al., 2007). *Underworld* combines an Eulerian grid-based finite-element formulation with a particle-based Lagrangian integration point scheme. The material points in *Underworld* are used for tracking tracking material properties, in particular material orientation and anisotropy. The rectangular finite-elements in our grid all have a uniform size of 10 by 5 km.

To account for the anisotropic viscosity we use a simplified constitutive law that assumes a transversely isotropic (TI) material. This kind of anisotropy can be characterized by two

viscosities – a shear viscosity η_s and a normal viscosity η_N (Honda, 1986). Mühlhaus et al. (2002b) define the following constitutive law using the orientation tensor Λ_{ijkl}:

$$\sigma_{ij} = -p\delta_{ij} + 2\eta_N\dot{\varepsilon}_{ij} - 2(\eta_N - \eta_S)\Lambda_{ijkl}\dot{\varepsilon}_{kl} \tag{A0}$$

where σ is the stress tensor, $\dot{\varepsilon}$ is the strain rate tensor. The orientation of the TI material enters the constitutive law through the orientation tensor Λ. It is calculated by tracking of a large set of directors, oriented particles representing the normals to the easy glide planes of the TI material (Mühlhaus et al., 2002b). We use 60 directors for each of the $\approx$ 5400 finite-element cells, for a total of over 300,000 directors. To better represent the recrystallization that accompanies the development of lattice preferred orientation, we include the forced realignment technique described by Lev and Hager (2008a).

5.2.3 Analysis of flow models output

After a calculation reaches a steady state we calculate two values: the "strata with sufficient strain" (SWiSS) and the expected delay time from teleseismic shear-wave splitting. Combined, these parameters indicate where we can expect an anisotropic layer in the mantle.

Strata with sufficient strain (SWiSS)

We define the "strata with sufficient strain" as the region which, after the entire model has accumulated 70% engineering shear strain, has itself accumulated at least 70% strain. We use this cut-off value following the results of Zhang et al. (2000), who demonstrated alignment of olivine LPO with the shear direction experiments after 70% engineering shear strain. A finite shear strain of 0.7 occurs when the displacement across a layer is equal to the thickness of the layer. Given a velocity profile as a function of depth, $v(z)$, the relative displacement across a layer of thickness Δz after a time t is $t\frac{\partial v}{\partial z}\Delta z$. We can therefore define a criteria for sufficient straining of a layer: $t\frac{\partial v}{\partial z}\Delta z > \Delta z$. The time to accumulate 70% engineering shear strain across the entire model is $t = Z_0/V_p$, where Z_0 is the box depth and V_p is the plate velocity. In our simple shear model, $\frac{\partial v}{\partial z} = \dot{\varepsilon}$. We can define a normalized strain rate $\dot{\varepsilon}^* = \dot{\varepsilon}/V_p$ and

obtain the following criteria for sufficient shear strain: $\dot{\varepsilon}^* > 1/Z_0$.

SKS splitting times

To obtain a proxy of how the anisotropy obtained in our models would appear in seismic observations, To estimate the time delay that a split teleseismic shear wave will experience as it travels vertically through the model domain, we first need to calculate how much of the model material can develop a lattice preferred orientation. It is widely assumed that the development of LPO requires deformation by dislocation creep, and thus we need to examine the way in which strain rate in our model is partitioned between the two deformation mechanisms we considered – diffusion creep and dislocation creep. We calculate the viscosities of the two components ($\eta_{diffusion}$ and $\eta_{dislocation}$) and then assume that the strain rate fraction is inversely proportional to the relative viscosity of each component:

$$F_{dislocation} = \eta_{diffusion}/(\eta_{diffusion} + \eta_{dislocation}) \tag{A0}$$

SKS split time: Once we find the fraction of dislocation creep deformation as a function of depth, we convolve it with the SWiSS, and calculate the accumulated split time as follows:

$$dVs(z) = \begin{cases} 0 & z \notin SWiSS \\ 0.25 \times F_{dislocation}(z) & z \in SWiSS. \end{cases} \tag{A0}$$

which uses a 0.25 km/s difference between the fast and slow phases by taking $V_{slow} =$ 4.58 km/s and $V_{fast} = 4.75$ km/s (Savage, 1999). We also assume a linear relationship between the partitioning of diffusion and dislocation creep, the strength of the LPO and the resulting seismic anisotropy. The accumulated delay time is:

$$dt = \int_{bottom}^{top} \left(\frac{1}{V_0 - dVs(z)} - \frac{1}{V_0 + dVs(z)} \right) dz \tag{A0}$$

where V_0 is the average shear wave velocity.

5.3 Results

Depth profiles of the strain rate for models with a grain size of $d = 10mm$ and a range of δ values are shown in Figure 5-2. The figure also shows the cut-off value defining the SWiSS. The profiles demonstrate the relationship between anisotropic viscosity and localization of strain into a narrow zone.

The depth extent of the SWiSS as a function of the grain size d and the viscosity ratio δ is plotted in the contour map in Figure 5-3. The SKS splitting times are shown in Figure 5-4. Both plots reveal that a value of $\delta = 0.5$ for a grain size of 10mm, and $\delta > 0.3$ for grains larger than 15mm, are capable of reproducing the depth extent of the anisotropic layer in the upper mantle as observed by Debayle et al. (2005) and Nettles and Dziewonski (2008). a viscosity ration of 0.1 leads to a highly localized shear zone (only 10 km wide) at the top of the model domain. Such a narrow zone of aligned anisotropic material would result in mechanical decoupling of the lithosphere and the asthenosphere. It seems however that such localization is inconsistent with the seismic observations.

5.4 Discussion

As we mentioned earlier, constraints from seismic observations place most of the anisotropy in the upper mantle beneath the oceans to within a layer that reaches 200 km, with the maximal anisotropy observed at 120km depth (Debayle et al., 2005; Nettles and Dziewonski, 2008). The combination of parameters that gives us the best fit to this depth is $\delta = 0.3$ and d greater than 10mm. This result gives us a lower bound on anisotropic viscosity in the upper mantle, an important rheolgical parameter which is poorly constrained.

Our conclusion relies on the observations of seismic anisotropy. The observation of a strongly anisotropic layer beneath the oceans with a maximum anisotropy at 120km depth is shared by many studies, and appears to be robust (see a discussion by Kustowski et al. (2008)). We must keep in mind, though, that most of the constraints on the depth extent of anisotropy in the upper mantle come from the analysis of surface waves, and specifically of the difference in velocities of Rayleigh and Love waves. The depth region in which most of the

anisotropy is found is sometimes considered a problematic region for surface wave analysis, as the sensitivities of Love waves diminishes rapidly with depth at this exact range, while the sensitivity of Rayleigh waves extends deeper (e.g. Nettles and Dziewonski, 2008, Figure 1). These differences might be mapped to anisotropy, leading to overestimation of the depth extent of the anisotropy. If the depth of upper mantle anisotropy is indeed overestimated, the constraint we can place on δ and d would no longer be as tight. However, the results of studies using different techniques, for example normal modes (Beghein et al., 2006), do not differ significantly from those of studies using surface waves.

We find that the grains need to be larger than 10mm to explain the observed layer of seismic anisotropy in the upper mantle. Mercier and Nicolas (1975) suggest a grain size of 10mm for the xenoliths collected in the Alps and in Hawaii. A similar value is reported by Armienti and Tarquini (2002). Samples from ophiolites usually come from shallower depths in the mantle, closer to the Moho, but they too exhibit maximum grain sizes of 8-12mm (e.g. Dijkstra et al., 2002).

From the viscosities and strain rates in our model we can estimate the stress: taking mantle viscosity to be $10^{18} Pas$ (see Figure 5-1) and the strain rates to be on the order of $10^{-14} 1/sec$ (Figure 5-2), the stress is about 0.01MPa. Using the data of Karato (1980), plotting $d = 80\mu m$ against $\sigma = 100MPa$, a stress of 0.01MPa is in equilibrium with a grain size of over 1m (using the piezometer of Hall and Parmentier (2003), scaling $d \propto \sigma^{-n/p} = \sigma^{-}1.17$) or 0.8mm (using the paleowattmeter formulation of Austin and Evans (2007), scaling $d \propto \sigma^{-1/(1+p)} = \sigma^{-}0.25$). Our estimated grain size falls within this wide range, and is closer to the latter value, which uses an algorithm considered to be more robust (Behn et al., 2009). Eisenbeck (2009) and Behn et al. (2009) also find that grains at depth of 150km in the oceanic upper mantle should be $\sim$11mm large.

Some caution must be taken when using the experimentally-derived constitutive laws and constant to interpret the results of our models. There is a trade-off between uncertainty in the constant coefficients A in equation 5.2.1 for both diffusion creep and dislocation creep, and uncertainty in the calculated grain size. What is important in our kinematic models is the ratio of these two constants. Experimental uncertainty in the A ratio is estimated

to be a factor of 2. If A is in fact twice as small as the value we use, this translates to a change of 30% in the grain size. Since we predict grains that are larger than 10 mm, the uncertainty in grain size due to uncertainty in A is about 3 mm. In addition, the published values of the activation volumes V^* for olivine range between 0 to 30 cm^3/mol (Korenaga and Karato, 2008), with the activation volume of dislocation creep the least constrained value. If the V^*_{disl} is much higher (> 20 instead of 4 cm^3/mol), the zone in which deformation is accommodated by dislocation creep will be limited to shallow depth, unless the grains are much larger ($d > 20mm$). However, the overall viscosity profile for the upper mantle would then reach values on the order of $10^{22} Pas$, considerably higher than accepted estimates (e.g. Hager, 1991). Changing the geothermal gradient to $0.5°/km$ moves the depth of $\eta_{diffusion} = \eta_{dislocation}$ about 40 km shallower, but the composite viscosity profile and the relative viscosities of the two components at the at the uppermost part do not change much. We therefore believe that our results are not very sensitive to the selection of the geothermal gradient.

5.5 Conclusion

By successfully reproducing the observed confinement of seismic anisotropy to a 50km thick layer beneath the oceanic lithosphere, we are able to place a lower bound on the grain size and constrain the degree of anisotropic viscosity in the upper mantle. We find that anisotropic viscosity should be 0.5 for a grain size of 10mm. For larger grains ($d > 15$), the viscosity ratio can be between 0.3 and 1.

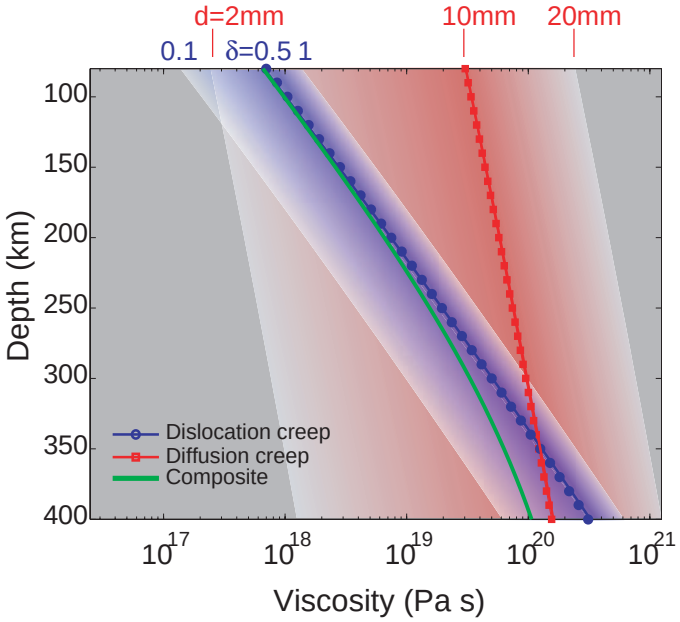

Figure 5-1: Depth profiles of the viscosity of the diffusion creep component (red), dislocation creep component (blue) and the composite material (green). The red shaded area shows the variation of diffusion creep viscosity for grain sizes ranging from 2 to 20mm. The blue shaded area shows the variation of dislocation creep viscosity multiplied by a range of δ values from 0.1 to 1.

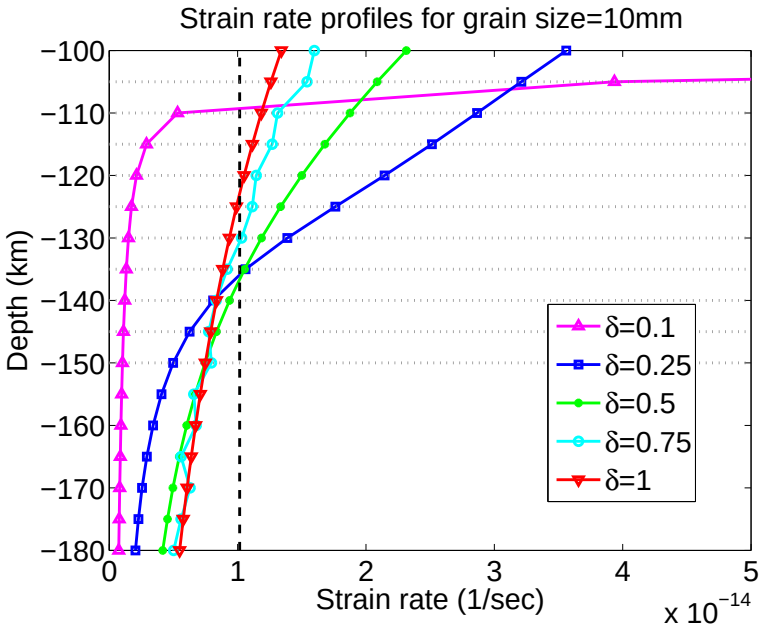

Figure 5-2: Strain rate profiles with depth for models with grain size $d = 10mm$. The vertical dashed line shows the cut-off criteria defining the zone with sufficient strain. The curves reveal the correlation between δ and the thickness of the zone of localized strain.

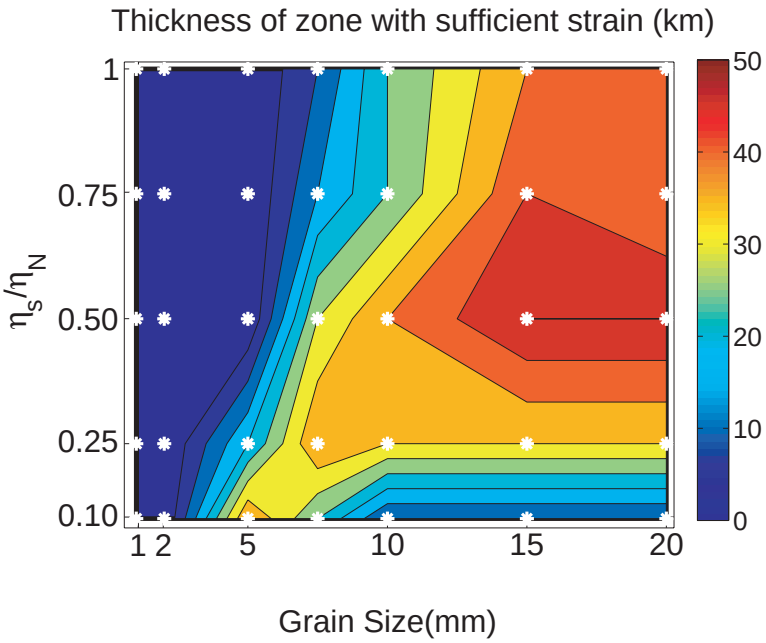

Figure 5-3: Thickness of the zone with sufficient as a function of the the grain size d and viscosity contrast δ. Areas in warm colors indicate thicknesses of 40 km or more, which are consistent with seismic observations. Cool colors indicate parameter values that give a layer that is either too thin (mostly for to low δ values) or that the strain rate is not high enough (grains too small).

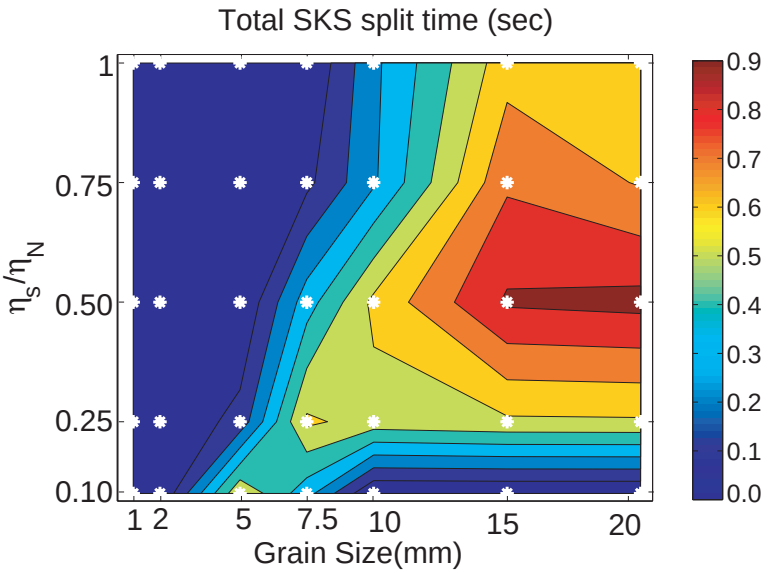

Figure 5-4: SKS delay times as a function of the the grain size d and viscosity contrast δ.

Chapter 6

Prediction of anisotropy from flow models – a comparison of three methods

6.1 abstract

Observations of anisotropy in the earth are used regularly as constraints for models of deformation, using various assumptions about the relationship between deformation and the resulting anisotropic fabric. We compare three methods for calculating fabric from velocity fields – tracking of finite strain ellipses, a kinematic crystallographic code, and the evolution of directors. We find that the use of the finite strain ellipse provides only limited prediction capabilities, as it cannot reproduce experimental observations that involve recrystallization. The crystallographic code we tested (a variant of the popular code D-Rex) provides a more complete fabric prediction, but at a much higher computational cost. The directors method provides an intermediate solution – while it does not include some of the more complex crystallographic processes that D-Rex does, the results of this method closely resemble those of D-Rex, at a lower computational cost. The directors are also capable of tracking anisotropy

[0]Published as: Lev, E. and B.H. Hager, Prediction of anisotropy from flow models a comparison of three methods, Geochem. Geophys. Geosys. 9 (2008), doi:10.1029/2008GC002032

at much larger strains than D-Rex. We conclude that when computation speed is important, for example in self-consistent geodynamic models with anisotropic rheology, the directors method provides an appropriate approximation.

6.2 Introduction

Understanding the way in which the lithosphere and the mantle deform is among the most fundamental goals of geodynamics. In recent years, observations of seismic anisotropy have been used extensively in attempts to constrain the deformation in Earth's interior at a wide range of tectonic settings and depths (e.g., Fischer and Wiens, 1996; Maupin et al., 2005; Fouch and Rondenay, 2006). The basic assumption made in this field of research is that deformation of geologic material results in the development of lattice preferred orientation (LPO), leading, in turn, to anisotropy of observables such as seismic wave speed and electrical conductivity.

The above assumption is supported by many natural examples of mantle rocks that exhibit strong textures (Ben-Ismail et al., 2001; Mehl et al., 2003), by laboratory experiments (Zhang and Karato, 1995; Jung and Karato, 2001) and by theoretical calculations (Kaminski and Ribe, 2001; Tommasi et al., 2000; Blackman et al., 2002) which exemplify the relationships between applied deformation and the development of preferred orientation. Usually these studies find an alignment of the LPO with the direction of shearing or extension, and this is commonly the form of anisotropy interpreted from flow models. However, both natural and laboratory samples display complexity, with dependence on volatile content, degree of melting, pressure and stress conditions (Jousselin and Mainprice, 1998; Jung and Karato, 2001).

Thanks to the increasing availability of measurements of seismic and conductive anisotropy in many regions of the earth (e.g. Montagner, 1998; Savage, 1999; Weiss et al., 1999; Simpson, 2002; Baba et al., 2006), it is becoming feasible to use them to constrain geodynamic models. Specifically, it may be possible to use anisotropy to distinguish between competing models based on the differences in the predicted anisotropy. It is thus clear that an accurate

technique for predicting anisotropy from a given geodynamic model is valuable, and that the differences between various prediction methods need to be identified. Additionally, it is important to track the anisotropy that develops during mantle flow as it can influence the deformation (Lev and Hager, 2008a). Mantle materials are often mechanically anisotropic (e.g., Durham and Goetze, 1977; Pouilloux et al., 2007), and knowing the texture is essential for modeling the flow accurately .

In this paper, we discuss three methods for predicting anisotropy from geodynamical flow models – the use of finite-strain ellipses, a kinematic crystallographic method (following Kaminski et al. (2004)), and tracking a set of directors (Mühlhaus et al., 2004). We begin by describing the details of each method, and then compare the fabrics that the three methods predict for several flows of increasing complexity. We then consider the computational cost of the methods, a factor that strongly affects their usefulness for integration with large-scale flow models.

6.3 Methods

In recent years, many studies have attempted to predict the anisotropic fabric that develops during deformation in the mantle. Two of the more popular techniques are the tracking of finite strain (e.g. McKenzie, 1979; Ribe, 1992; Hall et al., 2000; Becker et al., 2003; Long et al., 2007), and the employment of the kinematic crystallographic code D-Rex (Kaminski et al., 2004), for example, by Becker et al. (2006a,b) and Marquart et al. (2007). A third method we discuss here – the tracking of directors – was adopted from the field of liquid crystal physics for the purpose of including anisotropic viscosity in geodynamic flow models (Moresi et al., 2003). An additional method for predicting anisotropic fabric from flow models, which is not considered in this paper, is the polycrystal plasticity method (VPSC) (e.g. Wenk et al., 2006). VPSC is computationally intensive and thus it is not as readily available for straight-forward incorporation into flow models and is not discussed in this paper. The application of VPSC for predicting mantle anisotropy is discussed by Tommasi et al. (2000), who performed a detailed comparison between VPSC and an equilibrium-based

model (Chastel et al., 1993), as well as by Blackman et al. (2002).

The common input to all three methods we discuss here is a velocity field, calculated analytically or numerically, through which tracer particles ("aggregates") are propagated. The anisotropy is calculated in steps along the path, in the manners described below.

6.3.1 Tracking of the finite strain ellipse

The tracking of the long axis of the finite-strain ellipse (FSE) is a commonly used technique for predicting seismic anisotropy from flow models (Hall et al., 2000; Becker et al., 2003; Long et al., 2007). In these studies, the orientation of the major axis of the FSE is assumed to represent the orientation of the olivine a-axis and the direction of fast wave propagation. The stretched length of the FSE is taken as a proxy for the percentage of anisotropy.

In the calculation of the finite strain ellipse, we follow the formulation of McKenzie (1979), solving the following time-evolution equation:

$$\dot{F} = LF \tag{A1}$$

where F is the finite-strain tensor, $\dot{F}$ is its time-derivative, L is the velocity gradient tensor, and the finite-strain tensor at time $t = 0$ is the identity matrix I.

For simple cases, such as simple or pure shear, this equation can be solved analytically. For more complicated cases, this equation can be solved numerically using methods such as a time-centered scheme (McKenzie, 1979) or a fourth-order Runge-Kutta scheme.

For each step, we calculate the direction of the major axis of the finite strain ellipse and its magnitude using the inverse Cauchy strain tensor, C (Malvern, 1969):

$$C = (F^{-1})^T F^{-1} \tag{A2}$$

The major axis of the strain ellipse is oriented in the direction of the eigenvector associated with the largest eigenvalue of C.

6.3.2 FedRex, the Forward Evolution D-Rex

D-Rex (Kaminski et al., 2004) is a popular program for calculating seismic anisotropy resulting from the development of crystal lattice preferred orientation in response to a velocity field. It enables tracking of olivine and enstatite aggregates through a flow field, and supports texture evolution through plastic deformation and dynamic recrystallization by grain rotation and sliding. The equations controlling the time evolution of the texture are described by Kaminski and Ribe (2001, 2002), as well as Browaeys and Chevrot (2004). D-Rex was used recently in combination with flow models to predict global (Becker et al., 2006a) and regional (Becker et al., 2006b) seismic anisotropy. Because most observations of seismic anisotropy are interpreted in terms of hexagonal symmetry and the orientation of the olivine a-axis, the output of D-Rex we use here is the fast orientation resulting from reducing the full elastic tensor to its hexagonal symmetry projection.

For our purpose here we implemented a modification of D-Rex, named FedRex. In our modified code, particles are advected only forward in time, which makes the code faster than the publicly available version. The input velocity field to Fedex may change over time. Additionally, each particle may have a unique composition and crystallographic properties. In the future, our code can be easily extended to include the effects of local variations in temperature, pressure and volatile-content. As part of the development of FedRex, we made it fully three-dimensional, and added new features such as calculating the percentage of LPO contributed by various symmetries and the output of the grain Euler angles. FedRex uses the same crystallographic input parameters used in D-Rex – grain-boundary mobility (M) and grain boundary sliding threshold (χ).

One unique feature of D-Rex compared with other crystallographic codes and with the FSE method, is the consideration of recrystallization. Recrystallization causes LPO to adjust faster to a shear direction than the FSE axis. The implications of this difference were demonstrated previously by Marquart et al. (2007), who compared the predictions from the two methods for a model of a plume interacting with a mid-ocean ridge. They found significant deviations between the LPO predicted by FSE and by D-Rex. After comparing the predictions with observations of seismic anisotropy for Iceland they concluded that the

calculations using D-Rex agree with the data better than the FSE calculation.

6.3.3 Directors evolution

The "directors", a term adopted from material sciences and the study of liquid crystals, can be thought of as normal vectors to the planes of easy glide. Mühlhaus et al. (2002a) and Mühlhaus et al. (2004) discuss the application of the directors method to modeling anisotropic flow in the mantle, and the discussion here is based upon utilizing the tools they developed. The use of directors implicitly assumes a cubic or hexagonal symmetry. The directors define the axis of symmetry of the crystal, aggregate or parcel, which can then be used to determine the rotation of the elasticity or viscosity tensor. The relationship between the director and planes of easy-glide in olivine in the context of mantle flow is depicted in Figure 6-1.

The directors are advected in space similarly to particles. The orientation of each director, denoted by the vector $\mathbf{n}$, evolves in response to velocity gradients in the surroundings of the director:

$$\dot{n}_j = -L_{i,j} n_i \tag{A3}$$

where i, j relate to the coordinates, and $L_{i,j}$ is the (i, j) component of the velocity gradient tensor (Mühlhaus et al., 2004). The average orientation at a grid element is then calculated using averaging of the director orientations. To compare with the predictions of fast orientations resulting from FSE and FedRex, we assume here that the fast axis of each particle is perpendicular to the director. The strength of the anisotropy is calculated using the M-index (Skemer et al., 2005), an estimate of the mutual misorientation of the particles with each other. Section 6.5.3 describes in more detail the mapping between directors and seismic anisotropy, including the particular case of olivine.

In rocks, the process of dynamic recrystallization leads to rapid alignment of crystals with the direction of shear (Karato, 1988). To mimic this process, we added a forced realignment step to the basic directors method. We track the accumulated stretching of each

director, and after a prescribed threshold (denoted here by ξ) is reached, we realign the director to be normal to the local infinite strain axis (ISA). We calculate the ISA similarly to Kaminski and Ribe (2002) (appendix A), by taking the longest eigenvector of the matrix $U = F^T F = \exp(L\tau_\infty)^T \exp(L\tau_\infty)$ of the local velocity. In purely rotational parts of the flow, where the ISA is not defined, we use the orientation calculated by Eqn. 6.3.3. In the future, the realignment threshold, ξ, may be made sensitive to temperature, composition and other local conditions. The use of a discrete threshold and realignment to simulate the continuous process of recrystallization is valid when a large enough set of directors is being tracked together and averaged over. We find that in the flows examined here, a set of 40 directors per aggregate or finite-element was sufficient to give a smooth transition between a randomly oriented set to a fully aligned set.

We use the tests described below to calibrate the stretching threshold. After this realignment, the director is not stretched any further. Since the directors methods tracks a group of directors which orientations are then averaged to obtain the orientation of the aggregate, this realignment with the shear direction is gradual and smooth, similarly to recrystallization in natural rocks. Applying a similar realignment on an individual director or finite strain ellipse would lead to a sharp and unnatural transition.

One advantage of the directors method over crystallographic methods such as FedRex and VPSC is its ability to track very large strains. This makes the directors method more applicable for integration with mantle flow models, especially such that span long time periods.

6.4 Tests and Results

We compare the resulting fabric predicted by the three methods in three tests with increasing levels of complexity. Figure 6-2 illustrates schematically the test setups. We first calibrate the free parameters for each method using a two-dimensional (2D) plane strain simple-shear model. We continue with another steady-state model, of a 1x1 convection cell, starting with initially isotropic material throughout the model domain and then examining the fabric at

specified time intervals. Lastly, we look at a case of 2D time-dependent flow resulting from an instability of a dense material sinking into a more buoyant substratum (Figure 6-2c). The velocity field for this test was generated using the finite-element code Underworld (Moresi et al., 2003) assuming an isotropic, Newtonian rheology.

6.4.1 Simple Shear

The results of the simple shear tests are presented in Figure 6-3. We plot the orientation of the major axis of the finite-strain ellipse (cyan) and that of the average olivine a-axis (red is FedRex, blue and gray shades are directors) with respect to the direction of shearing (horizontal). For comparison, we also show the results of the laboratory experiments on olivine by Zhang et al. (2000). The input parameters to FedRex ($M = 125, \lambda = 5, \chi = 0.3$) are those found by Kaminski et al. (2004) to best fit experimental results.

We find, not surprisingly, that when no forced realignment occurs ($\xi = \infty$), the average of director A-axes follows the finite-strain ellipse. The directors closely agree with the results of FedRex and the lab experiments when the stretching threshold is set to approximately 1.5. Kaminski and Ribe (2001) find that a grain-boundary sliding threshold of $\frac{grain\ size}{initial\ grain\ size} = \chi = 0.3$ gives a good fit to experiments. We tested FedRex under simple shear conditions and found that this value of χ is reached after a stretching of 60% (natural strain = 0.47). This value compares well with the stretching threshold of $\xi = 1.5$ we find for the directors.

6.4.2 Steady-state 1x1 "convection cell"

The input velocity field used here is defined as:

$$\begin{aligned} V_x = &\quad \cos(\tfrac{\pi x}{2}) \sin(\tfrac{\pi z}{2}) \\ V_z = &\quad -\sin(\tfrac{\pi x}{2}) \cos(\tfrac{\pi z}{2}) \end{aligned} \tag{A4}$$

where x, z are the coordinates, both ranging from -1 to +1. Note that for this velocity field, the off-diagonal components of the velocity gradient tensor encountered by the particle along its path stay almost constant, while the diagonal components, associated with pure-shear,

change.

In Figure 6-4 we show the velocity field used in this test (red arrows), and the resulting fabric for one particle tracked along a complete round trip path. Yellow bars show the A-axis calculated by FedRex scaled by the percent of anisotropy (ranging from 1 to 14%). Black ellipses show the finite strain ellipses, and rose diagrams show the distribution of director A-axis orientations. It is clear that the fabrics from all three methods agree after the particle has turned the first corner and any original fabric is annealed.

6.4.3 Time-dependent layered-density instability

Many geodynamic studies predicting anisotropy assume steady-state flow. However, flow fields in the mantle are often not in steady state – plate geometry evolves with time, subduction initiates and ceases, continents collide and break apart and plumes and drips grow off unstable boundary layers. It is thus important to consider the effects of time-dependent flow fields on the evolving anisotropy. We examine this effect using a simple model of a "drip" – a Rayleigh-Taylor instability driven by the negative buoyancy of an overlaying layer. This process is intrinsically unstable and is not at steady state until a complete density overturn is reached. In Figure 6-5 we plot the paths of particles starting at the same point and advected by each of the varying velocity fields assuming that each field is kept constant; the paths are clearly different. We also plot the "real" path of a particle starting at this point and advected by the changing velocity field. This path is different from all the steady-state paths.

In this test, we analyze both the evolution of a single particle, and the evolution of the whole model domain, which we initialize as having no LPO. The input parameters for FedRex are those preferred by Kaminski and Ribe (2001), and the stretching threshold for the Directors is $\xi = 1.5$, following the results of section 6.4.1.

Figure 6-6 displays the evolution of olivine LPO – orientation and magnitude – calculated using FedRex (cyan, pink), Directors (blue) and the FSE (black) methods. There is usually good agreement between the predictions of three methods along the particle path, with some deviation at the beginning of the path.

In Figure 6-7 we show the anisotropy field calculated using directors as it evolves and develops over time. The LPO is calculated by averaging over a much coarser grid than the one used in the finite-elements calculation of the flow field (32x10 blocks vs 240x32 elements), to make it more comparable to the wavelength of seismic waves used to study mantle anisotropy (SKS, for example). This figure demonstrates how the directors method is readily capable of tracking the development of anisotropy within a region over time.

6.5 Discussion

6.5.1 Infinite Strain Axis vs. Directors

A variant of the FSE technique is the calculation of the Infinite Strain Axis (ISA), defined as the orientation of the FSE after being subjected to a constant velocity gradient for infinite time (Kaminski and Ribe, 2002). This technique gives a quick estimation of the anisotropy orientation, and it has been proven to approximate the prediction of the crystallographic technique of D-Rex well through most of the earth's mantle (Conrad et al., 2007). Unlike the tracking of the FSE, the ISA at a given time and place does not depend on the path, and therefore is not influenced by the assumed initial conditions. However, this method was shown to give poor results in regions of the earth that deform more slowly, such as the more rigid lithosphere, and thus cannot be used to estimate 'frozen-in' anisotropy (Conrad et al., 2007). Another limitation of the ISA technique is that in parts of the mantle where the velocity gradient changes rapidly along a streamline, or where the rotational component is larger than the straining component, the ISA might not be defined. Examples for such regions are places of strong downwelling or upwelling through the asthenosphere, such as active plate boundaries (subduction zones and mid-ocean ridges), as well as small-scale convection (e.g. Montagner, 2002; van Hunen et al., 2005). Since these regions are quite often the focus of geophysical interest, as well as the source of many of the observations of anisotropy, an alternative fabric prediction technique is required.

6.5.2 Computation cost and availability of the methods

The vast majority of the predictions of anisotropy come from mantle flow models that, in fact, assume isotropic rheology. Lev and Hager (2008a) showed that including anisotropic viscosity and allowing for mutual feedback between the deformation, the rheology and the anisotropy, change the flow. Such self-consistent modeling requires a texture prediction technique that is efficient and fast, as well as suitable for a straight-forward integration with geodynamic flow calculation codes. The computational cost of each of the methods is also important when long or time-dependent calculations are considered. We analyze here the computational cost involved with the directors method and compare it with that of FedRex.

Our measurements of *Underworld* runs (Figure 6-8), indicate that approximately 30% of the program execution time is spent on the time-integration of the director orientation and length parameters. This percentage is almost independent of the finite-element mesh size or the number of directors. The total number of directors strongly controls the overall duration of calculation, as the orientation calculation is the most time-consuming stage.

For a single particle, the calculation of the FSE takes 4 times longer than the director. However, we find that in order to obtain a meaningful average orientation for a set of directors, at least 10 are needed if realignment is not applied, and at least 30 are needed if realignment is applied. This makes the directors method 8 times slower than the FSE method. On the other hand, the use of a large set of directors facilitates the simulation of a continuous recrystallization process. To achieve this using FSEs would require averaging a set of ellipses, and would make the computational cost of the two methods comparable.

The computational cost of the Directors methods is still low compared with that of FedRex, as the Directors method is both faster and requires much less memory. At every time step, we advance the orientation of each director using equation 6.3.3 and a 2^{nd} order Runge-Kutta integration scheme. We compare the length of the new director and calculate the accumulated stretch, and, if needed, realign the director. This is a much simpler calculation than the calculation done in FedRex, where three vectors are rotated for each grain, and the energy of slip systems, as well as the change in the volume fraction of each grain, are calculated. Our tests reveal that *Underworld*'s execution time scales with the square root

of the number of directors (Figure 6-8), while FedRex scales linearly and quite strongly with both the grid size and the number of grains per aggregate (Figure 6-9). To obtain the same model resolution and accuracy with both methods, one would need a very large number of aggregates in FedRex, which would lead to a much longer execution time. It is also interesting to note that in the current implementation of FedRex, approximately 50% of the run time is spent on the time-integration phase, and over 50% of the run time is spent on calculating the Voigt average of grain orientations to obtain the complete tensor of the aggregate. The directors method uses a simpler, Finite-Element-style, averaging scheme and is thus faster in this stage as well. These differences make the directors method notably faster. Therefore, including a FedRex-like calculation in a flow code would increase its execution time significantly.

In addition, the memory that the directors method requires is smaller. Because of the assumption of hexagonal symmetry, each director is represented solely by a vector and an accumulated stretch value, a total of 4 numbers (3D) or 3 numbers (2D). FedRex, on the other, hand keeps a 9-element matrix of cosine angles (representing the orientation of the three crystallographic axes) for each grain, as well as a vector holding the fractional grain volumes, and matrices holding the derivatives of these matrices. We also find that an aggregate of less than 100 directors gives a stable solution that compares well with an aggregate of 1000 grains in FedRex.

One important factor for the modeling community is that the Directors method is implemented in the C language and is already embedded in the advanced geodynamics codes *Underworld* and *Gale*. D-Rex and FedRex are written in Fortran, which makes the integration with geodynamics codes, commonly written in C, less straightforward. This ease of integration is valuable for applications studying the effect of the development of anisotropy on flow models through feedback between deformation and rheology (Mühlhaus et al., 2004; Lev and Hager, 2008a).

6.5.3 Relating director orientations and olivine seismic anisotropy

The directors, by their very definition, imply a high symmetry of the tracked aggregates with respect to deformation and viscosity. The directors define an easy glide plane, representing a dominance of one family of easy slip systems that can be written as $(010) < h0\ell >$ (with the director set as the (010) b-axis). This kind of slip is common in minerals such as graphite, calcite, quartz and mica. In dry olivine, however, the dominant slip systems at relatively low stress, pressure and temperature conditions are (010)[100] and (001)[100], while the system (010)[001] is more resistant (e.g. Zhang and Karato, 1995; Tommasi, 1998). Under different temperature, water content and stress conditions the dominant slip system of olivine changes (Figure 6-10). Approximating olivine rheology with the layered type of rheology implied by the basic definition used by Mühlhaus et al. (2004) and Lev and Hager (2008a) means that the director orientation $\hat{n}_d$ is identified with the olivine b-axis and that the relative strength of the olivine slip systems is only partially accounted for. Nonetheless, the generality of the directors enables us to relate the predicted mantle seismic anisotropy to the developed orientation of easy glide planes by taking into account the local P, T and water conditions. We suggest assuming that the directors define the normal to the foliation planes. To choose the lineation direction, which is inherently non-unique by the definition of the directors, we use the projection of the local direction of maximum shear (based on the velocity gradient) onto the foliation plane. Figure 6-1 depicts the various orientations defined above.

The seismic velocities in different directions in olivine crystals depend mostly on the lattice structural density, and not on the dominant slip system. The a-axis is considered to always be the fast propagation direction (Babuška and Cara, 1992). The relationship between the seismically fast direction and the foliation/lineation system depends on which slip system is active, which, in turn, depends on the local conditions. For type-A olivine LPO, the seismically fast a-axis is oriented parallel to the lineation, and the b-axis is oriented normal to the foliation (thus parallel to the directors). In B-type olivine LPO, perhaps relevant to hydrated subduction zone conditions, the b-axis is still normal to the foliation and parallel to the director, but the a-axis is normal to the lineation (and the c-axis is parallel to the lineation). A more general algorithm would be to track the orientation of the

crystal axes, and infer the direction of the easy glide planes given the local conditions and the activity of the various slip systems they imply. The algorithm described above, however, would enable us to translate the orientation we track for the sake of rheological anisotropy to orientations relevant to crystal orientations and the seismic anisotropy quickly and cheaply, and using tested tools that already exist. To quickly deduce orientation and strength of the anisotropy represented by a set of closely-spaced directors, we take an angular averaging of their directions, and calculate the M-index (Skemer et al., 2005), as we demonstrated in Figure 6-7.

In the previous section we compared the directions of LPO axes predicted by the three methods and showed that the directors and the crystallographic code agree for all three test cases. However, the directors are only capable of representing cubic and hexagonal symmetries, while FedRex calculates the evolution of the full elastic tensor of the aggregates. It is thus important to determine how much of the anisotropy predicted by FedRex is due to hexagonal symmetry and can be reproduced safely by the directors, and how much requires a more sophisticated treatment. We added to FedRex an implementation of the method of Browaeys and Chevrot (2004), in which the full elastic tensor at every step of the flow is decomposed into its different symmetry components – isotropic, hexagonal, orthorhombic, tetrahedral, monoclinic and triclinic – in decreasing order of symmetry. We first tested a simple-shear case for two aggregate compositions – one made of 100% olivine and one of 70% olivine and 30% enstatite. We then propagated an olivine aggregate with initially random orientation through a Rayleigh-Taylor instability model and checked the patterns of crystallographic symmetry that develop.

The results, plotted in Figure 6-11, show clearly that for the cases tested, the hexagonal component of the symmetry describes the lion's share of the anisotropy (Note that although the flow is 2D plane strain, the initial random fabric is 3D, so the fabric retains a small component of orthorhombic symmetry). We conclude therefore that the approximation made by using directors may be valid in most cases relevant to the mantle.

6.6 Summary

We compare three methods for calculating fabric from a given velocity field – tracking of the finite strain ellipse, a kinematic crystallographic code, and the evolution of directors. We find that the use of finite strain ellipses can provide only limited accuracy for fabric evolution prediction, as it does not take into account the process of recrystallization. The kinematic code D-Rex, after some modification, provides a more complete method for fabric prediction, but its computational cost is significantly higher. This high computational cost, as well as its lower integrability, limits D-Rex's usefulness for large-scale geodynamical flow models. The directors provide a intermediate solution — while they inherently imply higher symmetry than the full crystal structure considered by D-Rex, as well as ignoring the physical basis of some of the more complex crystallographic processes D-Rex includes, the overall results of this method closely resemble those computed via D-Rex, at a lower computational cost. In conclusion, when computation speed is important, for example in self-consistent geodynamic flow models that incorporate anisotropy into the model rheology, the directors method provides an appropriate approximation.

Acknowledgements

We are thankful for helpful discussions with Jessica Warren, Nick Austin, Laurent Pouilloux and Andrea Tommasi. Reviews by Eduard Kaminski and an anonymous reviewer were greatly appreciated and helped improve this manuscript. The research presented here was supported by NSF grant EAR-0409564

6.7 Appendix – Codes used in this chapter

The codes used in this chapter are available online as electronic supplementary material on the journal's website.

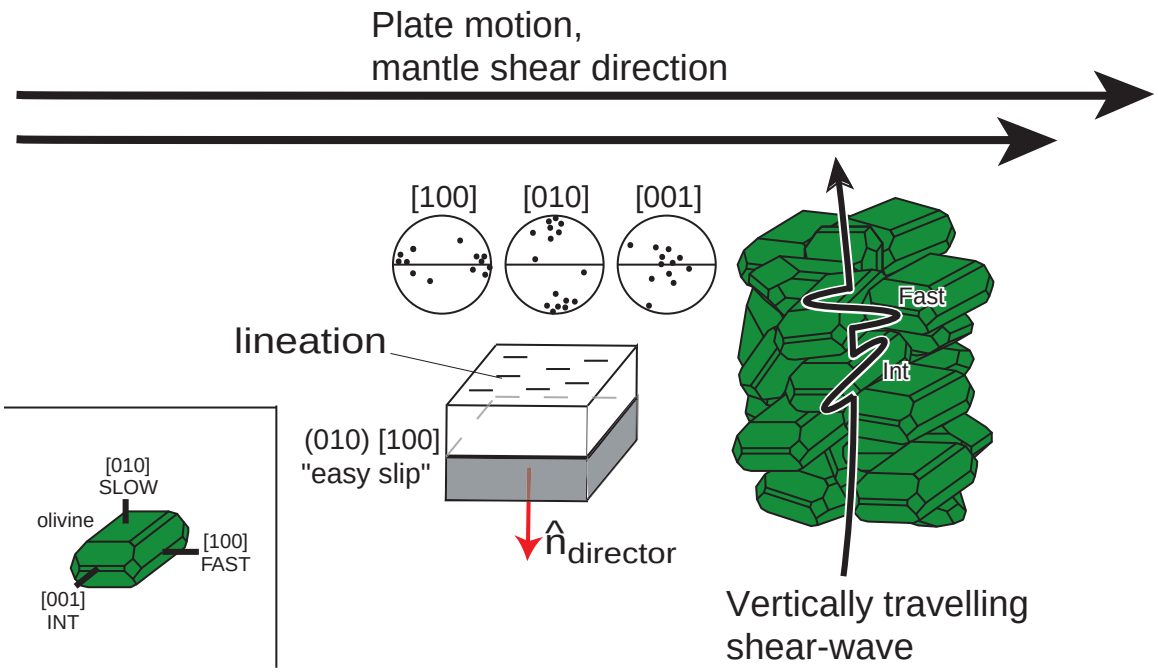

Figure 6-1: The relationship between directors, olivine LPO and seismic anisotropy. We show here olivine LPO type A, in which the dominant slip system is (010)[100]. The director is thus parallel to the b-axis, and the lineation, deduced from the local shear direction, parallels the a-axis. This 1-step mapping from directors to LPO allows for a rapid prediction of seismic anisotropy, represented here by the splitting of a vertically traveling shear-wave (e.g. SKS). The schematic pole figures illustrate the distribution of crystal orientations in the aggregate shown. The inset in the bottom left corner identifies the relative seismic wave speeds in association with olivine crystal axes. The original version of this figure was prepared by Luke Mehl and Jessica Warren.

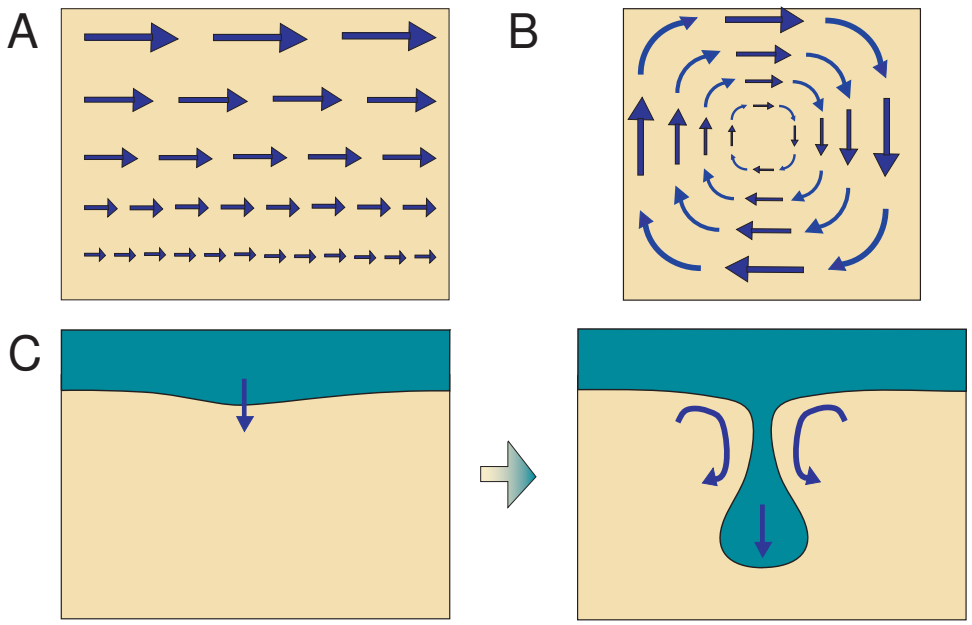

Figure 6-2: Schematic diagrams showing the flow fields in the three tests addressed in this paper. (A) Simple shear, used for validation of the calculations and for calibration of parameters; (B) 1x1 convection cell; (C) Rayleigh-Taylor instability, a sinking dense "drip".

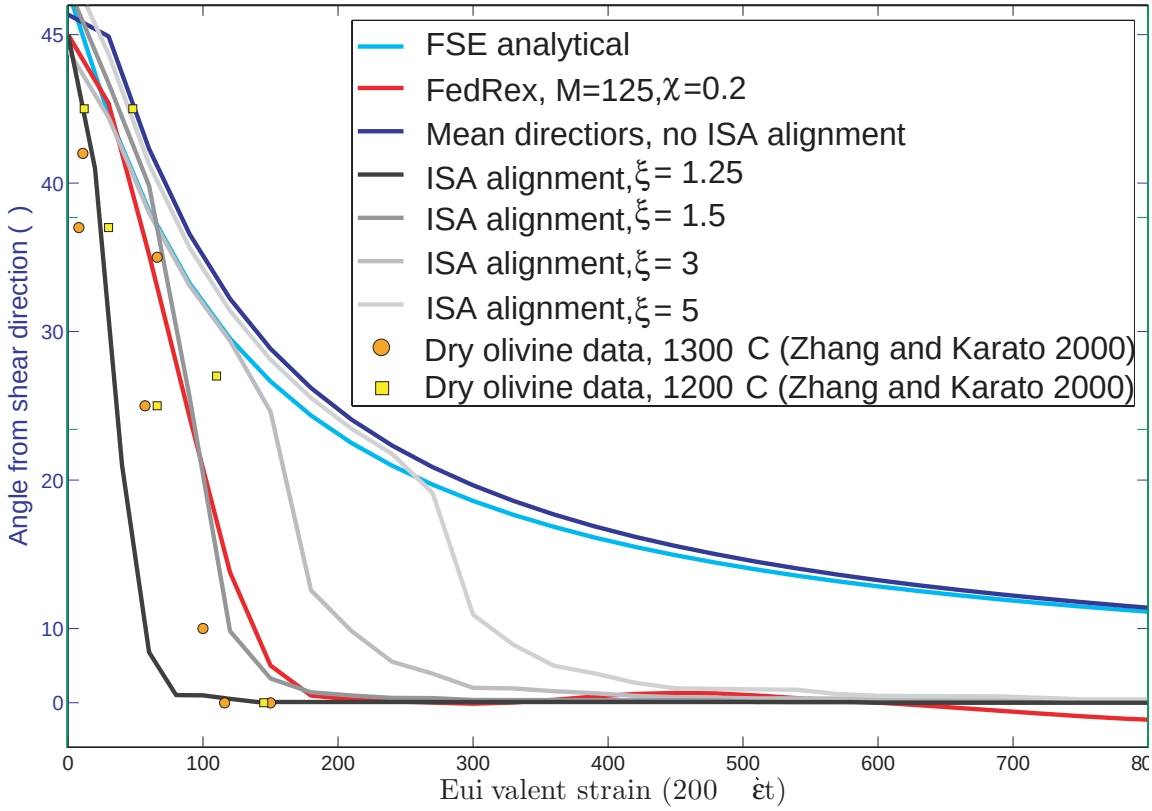

Figure 6-3: Results of the simple-shear test. Plotted are the inclination of the finite-strain ellipse and the A-axis of olivine calculated using the three methods. For FedRex, M is the grain boundary mobility, χ is the grain boundary sliding threshold. For the directors method with infinite strain axis (ISA) alignment, ξ is the stretching threshold for realignment. Also shown are laboratory experiment results from Zhang et al. (2000).

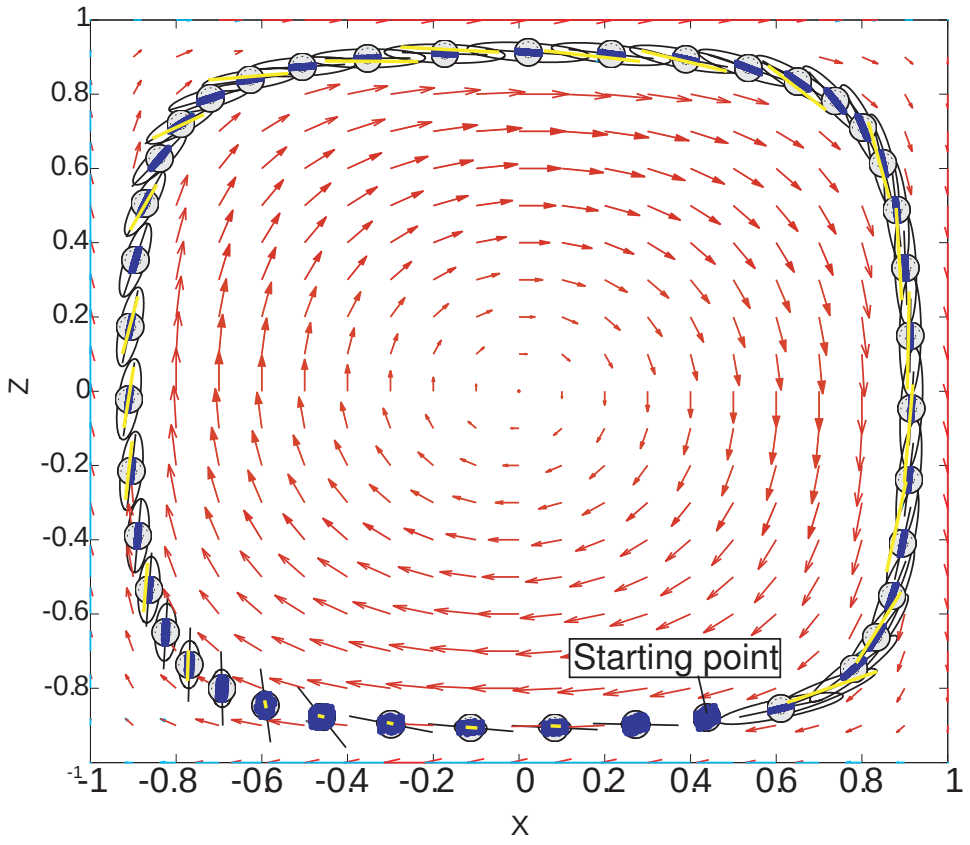

Figure 6-4: Results of a convection cell test – at each step we plot the finite strain ellipse (black ellipses) and its major axis, the A-axis orientation calculated by FedRex (yellow lines), and the distribution of A-axes using a set of directors (blue rose diagrams).Clearly, all methods agree with each other soon after the beginning of the path.

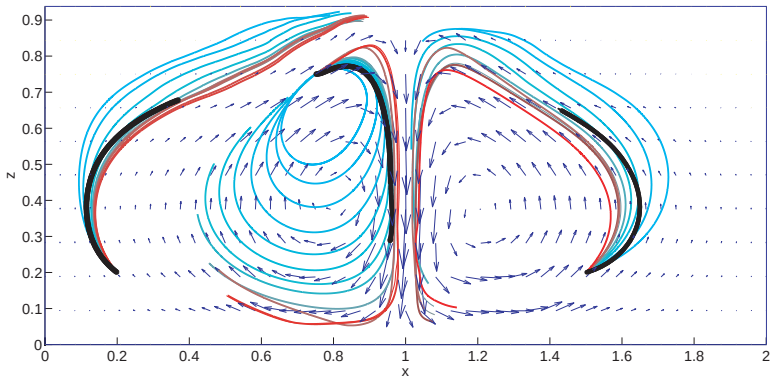

Figure 6-5: Changes in particle trajectories for a particle starting at the same spot and advected by the different velocity fields resulting from a sinking of a dense drip at different time steps (cyan – early steps, red – late steps). Plotted in black are the actual paths of the particles as they are advected at each time step by the instantaneous velocity field associated with that time step. The arrows sketch the velocities at a time step towards the end of the calculation.

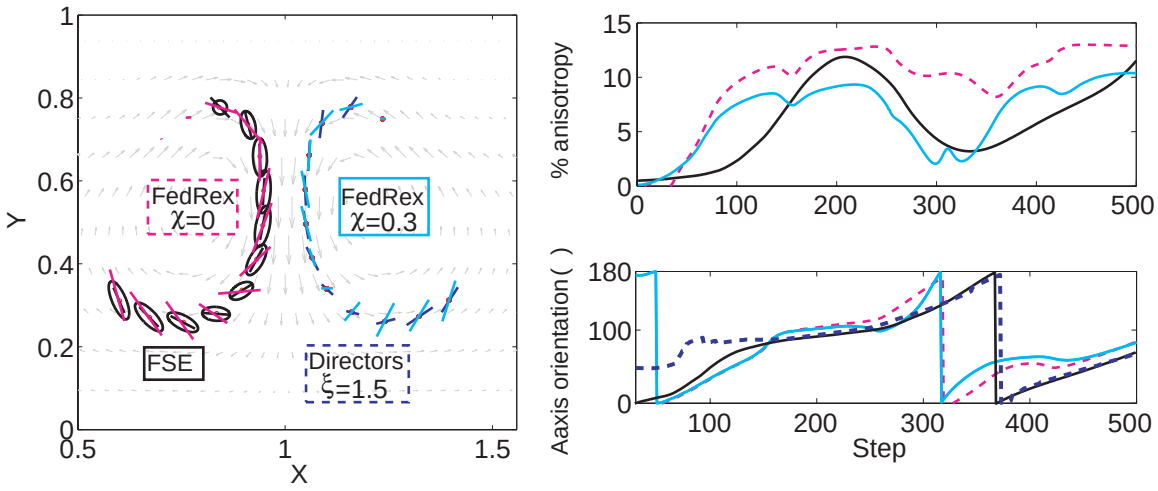

Figure 6-6: Results for a steady-state Rayleigh-Taylor instability test. We compare the orientation of the finite-strain ellipse major axis and the calculated A-axis for a single advected aggregate. The predictions made by the three methods methods are usually aligned with the direction of the flow and, for the most part, agree with each other. Left hand panel: the grey arrows in the background reflect the velocity field. Black ellipses and lines depict the finite strain ellipses and their major axes. Cyan and pink lines show results from FedRex, for $\chi = 0$ (pink) and $\chi = 0.3$ (cyan). Blue lines show the resulting A-axis orientation from advection of a set of 40 directors. Right hand side, with line colors matching the colors in the left panel: Top – the % of anisotropy estimated by the FedRex and FSE methods, calculated as $\frac{Vp1-Vp2}{Vp1+Vp2} \times 100$; Bottom – A-axis orientation (in degrees from the horizontal) for the three methods.

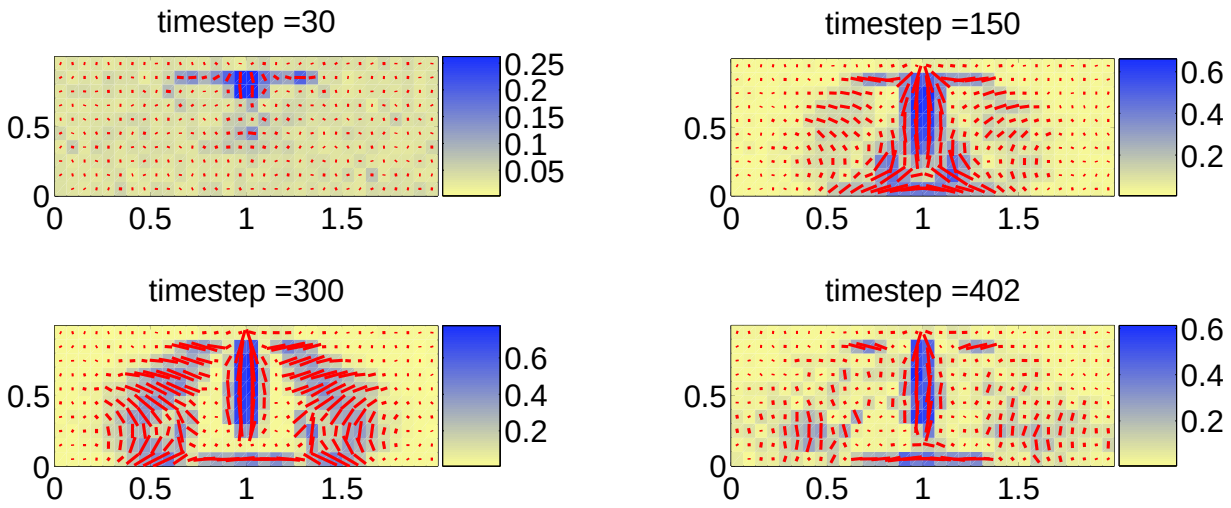

Figure 6-7: Time evolution of the anisotropy, calculated using the Directors method, in a model of a Rayleigh-Taylor instability driven by density layering. The background color of each panel shows the M-index, a metric of the strength of the anisotropy within that block. The range of M-index is zero (no LPO) to 1 (complete alignment). The red bars show the direction of the A-axis as calculated by averaging the orientations of the director within the block. Note that the element resolution of the initial finite-element calculation is much higher than the blocks used for the averaging presented here.

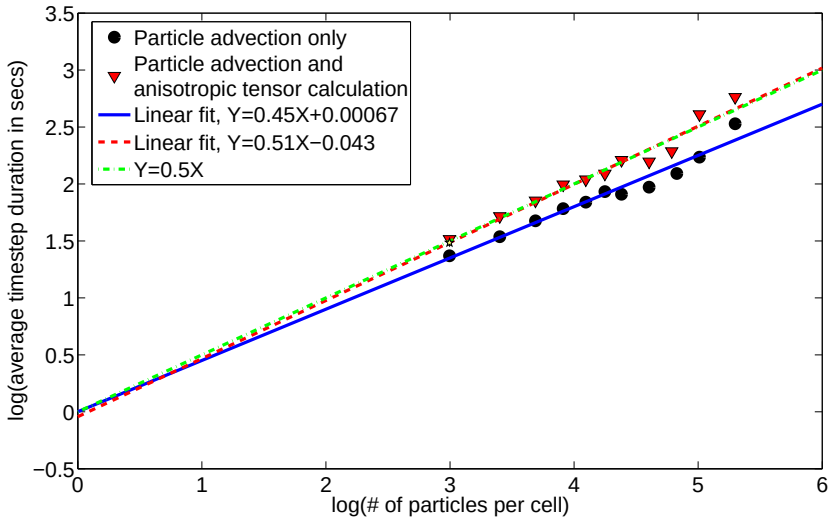

Figure 6-8: *Underworld* execution time (log) for a 2D model of Rayleigh-Taylor instability with a 64x64 elements grid, as a function of the number of directors per element (log). Circles, blue line – show the results for advection of isotropic particles (no tracking of orientation); Triangles, red line show the results for advection of directors, including tracking of orientation and length. The green dashed line has a slope of 0.5, underlining the observation that the execution time scales as the square root of the number of particles.

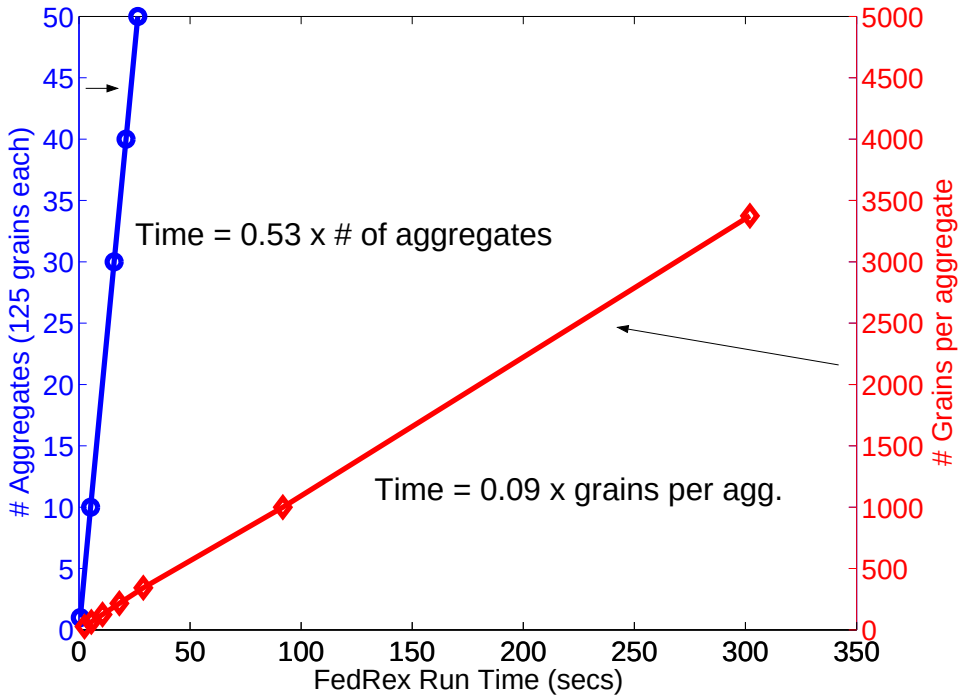

Figure 6-9: *FedRex* execution time plotted against the number of aggregates propagated through the model domain (blue, circles), and against the number of grains per aggregate (red, diamonds). The stronger dependence on the number of aggregates indicates that more time is spent on per-aggregate calculations such as Voigt averaging and propagation in space, compared to time spent on per-grain calculations. Specifically, our measurements reveal that the Voigt averaging is the time-consuming stage.

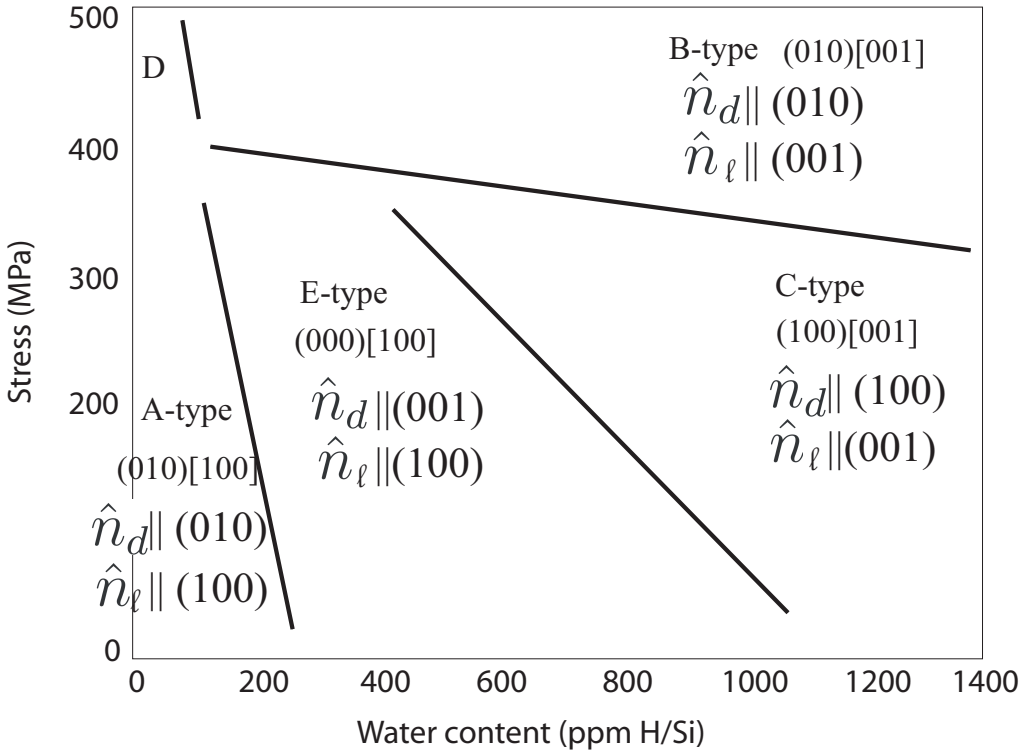

Figure 6-10: Types of olivine LPO as a function of water content and stress at temperature T = 1400 to 1570K. after Jung and Karato (2001) . For each type where the dominant slip system is known, we identify the relationship between the a-, b- and c- axes and the directors. $\hat{n}_d$ is the director orientation and n_ℓ is the lineation. This matching can help translate from a given orientation of directors and local model conditions (stress, water content, temperature, pressure) to predicted seismic anisotropy, keeping in mind the assumption about the relative wave speeds along the crystal axes.

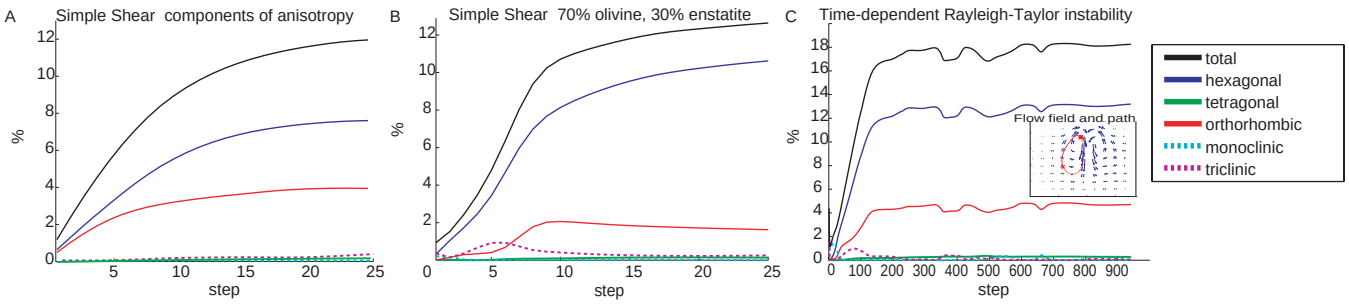

Figure 6-11: The proportions of the symmetry components in the total anisotropy of a deformed aggregate, as predicted by FedRex. (A) simple shear test with 100% olivine, (B) simple shear test with 70% olivine and 30% enstatite, (C) a drip flow model with 100% olivine. In all cases, and mostly for the more realistic composition of 70% olivine, the hexagonal component makes the predominant part of the anisotropy. For the simple shear test of a 100% olivine aggregate, the orthorhombic component is also somewhat large. The inset shows the velocity field and particle path used for this calculation. The hexagonal component again is responsible for most of the anisotropy. The insets show two views of the the velocity field and particle path used for this calculation. The red bars show the A-axis of the propagated aggregate.

Bibliography

D. Alsina and R. Snieder. Small-scale Sublithospheric Continental Mantle Deformation - Constraints from SKS Splitting Observations. *Geophys. J. Int*, 123:431–448, November 1995.

D. L. Anderson. Thermal State of the Upper Mantle; No Role for Mantle Plumes. *Geophys. Res. Lett.*, 27(22):3623–3626, November 2000.

P. Armienti and S. Tarquini. Power law olivine crystal size distributions in lithospheric mantle xenoliths. *Lithos*, 65(3-4):273 – 285, 2002. ISSN 0024-4937. doi: DOI: 10.1016/S0024-4937(02)00195-0.

N. J. Austin and B. Evans. Paleowattmeters: A scaling relation for dynamically recrystallized grain size. *Geology*, 35:343–347, April 2007. doi: 10.1130/G23244A.1.

K. Baba, A. D. Chave, R. L. Evans, G. Hirth, and R. L. Mackie. Mantle dynamics beneath the East Pacific Rise at 17S: Insights from the Mantle Electromagnetic and Tomography (MELT) experiment. *J. Geophys. Res.*, 111:B02101, 2006. doi: 10.1029/2004JB003598.

V. Babuška and M. Cara. *Seismic anisotropy in the earth*, volume 10 of *Modern approaches in geophysics*. Kluwer Academic Publisher, Dordrecht, The Netherlands, July 1992.

Q. Bai and D. L. Kohlstedt. High-temperature creep of olivine single crystals. II: Dislocation structures. *Tectonophysics*, 206(1-2):1–29, 1992.

G. Barruol and D. Mainprice. A quantitative evaluation of the contribution of crustal rocks to the shear-wave splitting of teleseismic SKS waves. *Phys. Earth Planet. Inter.*, 78:281–300, July 1993. doi: 10.1016/0031-9201(93)90161-2.

T. W. Becker, J. B. Kellogg, G. Ekström, and R. J. O'Connell. Comparison of azimuthal seismic anisotropy from surface waves and finite strain from global mantle-circulation models. *Geophys. J. Int.*, 155:696–714, November 2003.

T. W. Becker, S. Chevrot, V. Schulte-Pelkum, and D. K. Blackman. Statistical properties of seismic anisotropy predicted by upper mantle geodynamic models. *J. Geophys. Res.*, 111(B10):B08309, August 2006a. doi: 10.1029/2005JB004095.

T. W. Becker, V. Schulte-Pelkum, D. K. Blackman, J. B. Kellogg, and R. J. O'Connell. Mantle flow under the western United States from shear wave splitting. *Earth. Planet. Sci.Lett.*, 247:235–251, July 2006b. doi: 10.1016/j.epsl.2006.05.010.

C. Beghein, J. Trampert, and H. J. van Heijst. Radial anisotropy in seismic reference models of the mantle. *Journal of Geophysical Research (Solid Earth)*, 111:B2303, February 2006. doi: 10.1029/2005JB003728.

M. Behn, G. Hirth, and J. Eisenbeck. Implications of grain size evolution on the seismic structure of the oceanic upper mantle. *Earth. Planet. Sci. Lett.*, 282:178–189, 2009.

T. Belytschko, W. K. Liu, and B. Moran. *Non-linear finite elements for continua and structures*. John Wiley and Sons, LTD, Chichester, England, 2001.

W. Ben-Ismail, G. Barruol, and D. Mainprice. The Kaapvaal craton seismic anisotropy: Petrophysical analyses of upper mantle kimberlite nodules. *Geophys. Res. Lett.*, 28:2497–2500, July 2001.

H. Berckhemer, W. Kampfmann, E. Aulbach, and H. Schmeling. Shear modulus and Q of forsterite and dunite near partial melting from forced-oscillation experiments. *Phys. Earth. Planet. Int.*, 29:30–41, July 1982. doi: 10.1016/0031-9201(82)90135-2.

M. I. Billen and G. A. Houseman. Lithospheric instability in obliquely convergent margins: San Gabriel Mountains, southern California. *J. Geophys. Res.*, 109:B01404, January 2004. doi: 10.1029/2003JB002605.

M. I. Billen, M. Gurnis, and M. Simons. Multiscale dynamics of the Tonga-Kermadec subduction zone. *Geophysical Journal International*, 153:359–388, May 2003a.

M. I. Billen, G. Hirth, and P. B. Kelemen. Slab Dynamics and Non-Newtonian Rheology in the Upper Mantle. *AGU Fall Meeting Abstracts*, pages C244+, December 2003b.

D. K. Blackman, H.-R. Wenk, and J. M. Kendall. Seismic anisotropy of the upper mantle 1. Factors that affect mineral texture and effective elastic properties. *Geochemistry, Geophysics, Geosystems*, 3(9), September 2002. doi: 10.1029/2001GC000248.

J. T. Browaeys and S. Chevrot. Decomposition of the elastic tensor and geophysical applications. *Geophys. J. Int.*, 159:667–678, November 2004.

B. C. Burchfiel, Z. Chen, Y. Liu, and L. H. Royden. Tectonics of the Longmenshan and adjacent regions. *Int. Geol. Rev.*, 37:661–735, 1995.

O. Castelnau, D. K. Blackman, R. A. Lebensohn, and P. Ponte. Micromechanical modelling of the viscoplastic behavior of olivine. *Jour. Geophys. Res.*, 113, 2008.

Y. B. Chastel, P. R. Dawson, H.-R. Wenk, and K. Bennett. Anisotropic convection with implications for the upper mantle. *Jour. Geophys. Research*, 98:17,757–17,771, October 1993.

Z. Chen, B. C. Burchfiel, Y. Liu, R. W. King, L. H. Royden, W. Tang, E. Wang, J. Zhao, and X. Zhang. Global Positioning System measurements from eastern Tibet and their implications for India/Eurasia intercontinental deformation. *J. Geophys. Res.*, 105:16215–16228, 2000.

S. Chevrot. Multichannel analysis of shear wave splitting. *J. Geophys. Res.*, 105:21579–21590, September 2000.

S. Chevrot and R. D. van der Hilst. On the effects of a dipping axis of symmetry on shear wave splitting measurements in a transversely isotropic medium. *Geophysical Journal International*, 152:497–505, February 2003. doi: 10.1046/j.1365-246X.2003.01865.x.

U. Christensen. Some geodynamical effects of anisotropic viscosity. *Geophys. J. R. Astr. Soc.*, 91:711–736, 1987.

C. P. Conrad and P. Molnar. The growth of Rayleigh-Taylor-type instabilities in the lithosphere for various rhelogicial and density structures. *Geophys. J. Int.*, 129:95–112, October 1997.

C. P. Conrad and P. Molnar. Convective instability of a boundary layer with temperature- and strain-rate-dependent viscosity in terms of 'available buoyancy'. *Geophys. J. Int.*, 139: 51–68, October 1999.

C. P. Conrad, M. D. Behn, and P. G. Silver. Global mantle flow and the development of seismic anisotropy: Differences between the oceanic and continental upper mantle,. *J. Geophys. Res.*, 112:B07317, August 2007. doi: 10.1029/2006JB004608.

S. Crampin. Seismic-waves propagating through a cracked solid: polarization as a possible dilatancy diagnostic. *Geophys J. R. Astr. Soc.*, 53:467–496, 1978.

E. Debayle, B. Kennett, and K. Priestly. Global azimuthal seismic anisotropy and the unique plate-motion deformation in AUstralia. *Nature*, 433:509–512, 2005.

C. DeMets, R. G. Gordon, D. F. Argus, and S. Stein. Effect of recent revisions to the geomagnetic reversal timescale on estimates of current plate motions. *Geophys. Res. Lett.*, 21:2191–2194, 1994.

A. H. Dijkstra, M. R. Drury, and R. M. Frijhoff. Microstructures and lattice fabrics in the Hilti mantle section (Oman Ophiolite): Evidence for shear localization and melt weakening in the crust-mantle transition zone? *Journal of Geophysical Research (Solid Earth)*, 107: 2270–2288, November 2002. doi: 10.1029/2001JB000458.

M. R. Drury and J. D. FitzGerlad. Mantle rheology: Insight from laboratory studies of deformation and phase transition. In I. Jackson, editor, *The Earth's Mantle*, chapter 11. Cambridge University Press, 2000.

M. R. Drury, R. L. M. Vissers, D. van der Wal, and E. H. Hoogerduijn Strating. Shear localisation in upper mantle peridotites. *Pure and Applied Geophysics*, 137:439–460, December 1991. doi: 10.1007/BF00879044.

W. B. Durham and C. Goetze. Plastic flow of oriented single crystals of olivine 1. Mechanical data. *Jour. Geophys. Res.*, 82:5737–5754, 1977.

A. M. Dziewonski and D. L. Anderson. Preliminary reference Earth model. *Physics of the Earth and Planetary Interiors*, 25:297–356, June 1981.

J. Eisenbeck. Influence of grain size evolution and water content on the seismic structure of the oceanic upper mantle. M.sc., MIT, 2009.

L. T. Elkins-Tanton and B. H. Hager. Melt intrusion as a trigger for lithospheric foundering and the eruption of the Siberian flood basalts. *Geophys. Res. Lett.*, 27:3937–3940, 2000. doi: 10.1029/2000GL011751.

L. T. Elkins-Tanton and B. H. Hager. Giant meteoroid impacts can cause volcanism. *Earth and Planetary Science Letters*, 239:219–232, 2005. doi: 10.1016/j.epsl.2005.07.029.

P. England and G. Houseman. Finite strain calculations of continental deformation 2. Comparison with the India-Asia collision zone. *J. Geophys. Res.*, 91(10):3664–3676, March 1986.

P. England and G. Houseman. Extension during continental convergence, with application to the Tibetan Plateau. *Jour. Geophys. Res.*, 94:17561–17579, December 1989.

W. M. Fan, H. F. Zhang, J. Baker, K. E. Jarvis, P. RD. Mason, and Menzies.M. A. On and off the North China Craton; where is the Archaean keel? in In commemoration of Keith Gordon Cox, 1933-1998. *Journal of Petrology*, 41:933–950, July 2000.

K. M. Fischer and D.A. Wiens. The depth distribution of mantle anisotropy beneath the Tonga subduction zone. *Earth. Planet. Sci. Lett.*, 142:253–260, 1996.

M. P. Flanagan and D. A. Wiens. Radial upper mantle attenuation structure of inactive back arc basins from differential shear wave measurements. *Jour. Geophys. Res.*, 99: 15,469–15,485, August 1994. doi: 10.1029/94JB00804.

L. M. Flesch, W. E. Holt, P. G. Silver, M. Stephenson, C.-Y. Wang, and W. W. Chan. Constraining the extent of crust-mantle coupling in central Asia using GPS, geologic, and shear wave splitting data [rapid communication]. *Earth Planet. Sci. Lett.*, 238:248–268, September 2005. doi: 10.1016/j.epsl.2005.06.023.

T. F. Fliervoet and P. N. Drury, M. R. Chopra. Crystallographic preferred orientations and misorientations in some olivine rocks deformed by diffusion or dislocation creep. *Tectonophysics*, 303(1-4):1 – 27, 1999. doi: DOI: 10.1016/S0040-1951(98)00250-9.

M. J. Fouch and S. Rondenay. Seismic anisotropy beneath stable continental interiors. *Phys. Earth Planet. Int.*, 158:292–320, October 2006. doi: 10.1016/j.pepi.2006.03.024.

Y. Fukao. Evidence from Core-Reflected Shear Waves for Anisotropy in the Earth's Mantle. *Nature*, 309:695–698, 1984.

T. T. Gribb and R. F. Cooper. The effect of an equilibrated melt phase on the shear creep and attenuation behavior of polycrystalline olivine. *Geopys. Res. Lett.*, 27:2341–2344, August 2000. doi: 10.1029/2000GL011443.

D. Griot, J. Montagner, and P. Tapponnier. Confrontation of mantle seismic anisotropy with two extreme models of strain, in Central Asia. *Geophys. Res. Lett.*, 25:1447–1450, May 1998.

T. L. Grove, N. Chatterjee, Parman S. W., and Médard. E. The influence of h2o on mantle wedge melting. *Earth Planet. Sci. Lett.*, 249(1-2):74 – 89, 2006. doi: DOI: 10.1016/j.epsl.2006.06.043.

T. L. Grove, C. Till, E. Lev, E. Médard, and N. Chatterjee. Do kinematic variable and H2O transport control the formation and location of arc volcanoes? *Nature*, accepted(in press), 2009.

Y. Gung, M. Panning, and B. Romanowicz. Global anisotropy and the thickness of continents. *Nature*, 422:707–711, April 2003.

M. Gurnis. Phanerozoic marine inundation of continents driven by dynamic topography above subducting slabs. *Nature*, 364:589–593, November 1993.

B. H. Hager. Mantle viscosity - A comparison of models from postglacial rebound and from the geoid, plate driving forces, and advected heat flux. In R. Sabadini, K. Lambeck, and E. Boscni, editors, *Glacial isostasy, sea level and mantle rheology. Dordrecht, Netherlands, Kluwer Academic Publishers, 1991, 21 p.* Kluwer Academic Publishers, 1991.

B. H. Hager and R. J. O'Connell. A simple global model of plate dynamics and mantle convection. *Jour. Geophys. Res.*, 86:4843–4867, June 1981.

C. E. Hall and E. M. Parmentier. Influence of grain size evolution on convective instability. *Geochemistry, Geophysics, Geosystems*, page 1, March 2003.

C. E. Hall, K. M. Fischer, E. M. Parmentier, and D. K. Blackman. The influence of plate motions on three-dimensional back arc mantle flow and shear wave splitting. *J. Geophys. Res.*, 105:28009–28034, 2000.

W. C. Hammond and E. D. Humphreys. Upper mantle seismic wave attenuation: Effects of realistic partial melt distribution. *Jour. Geophys. Res.*, 105:10987–11000, 2000. doi: 10.1029/2000JB900042.

E. H. Hearn, E. D. Humphreys, M. Chai, and M. Brown. Effect of anisotropy on oceanic mantle temperatures, structure and dynamics. *Jour. Geophys. Res.*, 102:11,943–11,956, 1997.

H. Hess. Seismic anisotropy of the uppermost mantle under oceans. *Nature*, 203(4945): 629–631, 1964.

G. Hirth. Laboratory Constraints on the Rheology of the Upper Mantle. *Reviews in Mineralogy and Geochemistry*, 51(1):97–120, 2002. doi: 10.2138/gsrmg.51.1.97.

G. Hirth and D. Kohlstedt. Rheology of the upper mantle and the mantle wedge: a view from the experimentalists. *in: Inside the Subduction Factory*, AGU Monograph:83–105, 2003. doi: 10.1029/138GM06.

W. S. Holbrook, D. Lizarralde, S. McGeary, N. Bangs, and J. Diebold. Structure and composition of the Aleutian island arc and implications for continental crustal growth. *Geology*, 27:31–34, January 1999.

W. E. Holt, N. Chamot-Rooke, X. L. Pichon, A. J. Haines, B. Shen-Tu, and J. Ren. Velocity field in Asia inferred from Quaternary fault slip rates and Global Positioning System observations. *J. Geophys. Res.*, 105:19185–19210, August 2000.

B. K. Holtzman, D. L. Kohlstedt, M. E. Zimmerman, F. Heidelbach, T. Hiraga, and J. Hustoft. Melt Segregation and Strain Partitioning: Implications for Seismic Anisotropy and Mantle Flow. *Science*, 301:1227–1230, August 2003.

S. Honda. Strong anisotroic flow in a finely layered asthenosphere. *Geophys. Res. Lett.*, 13: 1454–1457, December 1986.

G. A. Houseman and P. Molnar. Gravitational Rayleigh-Taylor instability of a layer with nonlinear viscosity and convective thinning of continental lithosphere. *Geophys. J. Int.*, 128:125–150, 1997.

G. A. Houseman, D. P. McKenzie, and P. Molnar. Convective instability of a thickened boundary layer and its relevance for the thermal evolution of continental convergent belts. *Jour. Geophys. Res.*, 86:6115–6132, July 1981.

W. Huang, J. F. Ni, F. Tilmann, D. Nelson, J. Guo, W. Zhao, J. Mechie, R. Kind, J. Saul, R. Rapine, and T. M. Hearn. Seismic polarization anisotropy beneath the central Tibetan Plateau. *J. Geophys. Res.*, 105:27979–27990, 2000.

E. D. Humphreys and R. W. Clayton. Tomographic image of the Southern California mantle. *Jour. Geophys. Res.*, 95:19725–19746, November 1990.

E. D. Humphreys and B. H. Hager. A kinematic model for the late Cenozoic development of southern California crust and upper mantle. *Jour. Geophys. Res.*, 95:19747–19762, November 1990.

H. Iwamori and D. P. Zhao. Melting and seismic structure beneath the northeast Japan arc. *Geophys. Res. Lett.*, 27:425–428, 2000.

I. Jackson, M. S. Paterson, and J. D. FitzGerald. Seismic wave dispersion and attenuation in Åheim dunite: an experimental study. *Geophys. Jour. Int.*, 108:517–534, February 1992. doi: 10.1111/j.1365-246X.1992.tb04633.x.

D. Jousselin and D. Mainprice. Melt topology and seismic anisotropy in mantle peridotites of the oman ophiolite. *Earth Planet. Sci. Lett.*, 164:553–568, December 1998.

H. Jung and S. Karato. Water-Induced Fabric Transitions in olivine. *Science*, 293:1460–1463, August 2001.

É. Kaminski and N. M. Ribe. A kinematic model for recrystallization and texture development in olivine polycrystals. *Earth Planet. Sci. Lett.*, 189:253–267, July 2001.

É. Kaminski and N. M. Ribe. Timescales for the evolution of seismic anisotropy in mantle flow. *Geochem., Geophys., Geosyst.*, page 1051, August 2002. doi: 10.1029/2001GC000222.

É. Kaminski, N. M. Ribe, and J. T. Browaeys. D-Rex, a program for calculation of seismic anisotropy due to crystal lattice preferred orientation in the convective upper mantle. *Geophys. J. Int.*, 158:744–752, August 2004.

S. Karato. Low Q zone at the base of the mantle: Evidence for lower mantle convection? *Physics of the Earth and Planetary Interiors*, 22:155–161, May 1980.

S. Karato. The role of recrystallization in the preferred orientation of olivine. *Phys. Earth Planet. Inter.*, 51:107–122, June 1988.

S. Karato, S. Zhang, M. E. Zimmerman, M. J. Daines, and D. L. Kohlstedt. Experimental Studies of Shear Deformation of Mantle Materials: Towards Structural Geology of the Mantle. *Pure and Applied Geophysics*, 151:589–603, 1998.

S. Karato, M. R. Riedel, and D. A. Yuen. Rheological structure and deformation of subducted slabs in the mantle transition zone: implications for mantle circulation and deep earthquakes. *Physics of the Earth and Planetary Interiors*, 127:83–108, December 2001.

S.-I. Karato, S. Zhang, and H.-R. Wenk. Superplasticity in the Earth's lower mantle: Evidence from seismic anisotropy and rock physics. *Science*, 270:458–461, October 1995.

T. Katagi, S. Yoshioka, and M. Hashimoto. Influence of temperature- and depth-dependent viscosity structures on postseismic deformation predictions for the large 1946 Nankai subduction zone earthquake. *Tectonophysics*, 454:1–4, June 2008.

I. Katayama. Thin anisotropic layer in the mantle wedge beneath northeast Japan. *Geology*, 37(3):211–214, March 2009.

S. M. Kay, B. Coira, and J. Viramonte. Young mafic back arc volcanic rocks as indicators of continental lithospheric delamination beneath the Argentine Puna plateau, central Andes. *Jour. Geophys. Res.*, 99:24,323–24,339, December 1994.

P. B. Kelemen, J. L. Rilling, E M. Parmentier, L. Mehl, and B. R. Hacker. Thermal structure due to solid-state flow in the mantle wedge beneath arcs. *in Inside the Subduction Factory*, AGU Monograph 138:293–311, 2003.

D. V. Kemp. A model for the subduction mechanics of flexible lithosphere and its viscous coupling to the mantle using power-law rheologies. *Ph.D. Thesis*, 1992.

R. W. King, F. Shen, B. C. Burchfiel, L. H. Royden, E. Wang, Z. Chen, Y. Liu, X. Zhang, J. Zhao, and Y. Li. Geodetic Ceasurement of Crustal Motion in Southwest China. *Geology*, 25:179–182, February 1997.

E. A. Kneller, M. D. Long, and P. E. van Keken. Olivine fabric transitions and shear wave anisotropy in the Ryukyu subduction system. *Earth and Planetary Science Letters*, 268: 268–282, April 2008. doi: 10.1016/j.epsl.2008.01.004.

M. D. Kohler. Lithospheric deformation beneath the San Gabriel Mountains in the southern California Transverse Ranges. *Jour. Geophys. Res.*, 104:15025–15042, 1999. doi: 10.1029/1999JB900141.

J. Korenaga and S.-I. Karato. A new analysis of experimental data on olivine rheology. *Jour. Geophys. Res.*, 113:2403–2425, February 2008. doi: 10.1029/2007JB005100.

B. Kustowski, G. Ekström, and A. M. Dziewonski. Anisotropic shear-wave velocity structure of the Earth's mantle: A global model. *Journal of Geophysical Research (Solid Earth)*, 113:6306–6330, June 2008. doi: 10.1029/2007JB005169.

P. C. Leary, S. Crampin, and T. V. McEvilly. Seismic fracture anisotropy in the Earth's Crust: An overview. *J. Geophys. Res.*, 95:11105–11114, July 1990.

J.-F. Lebrun, G. Lamarche, and J.-Y. Collot. Subduction initiation at a strike-slip plate boundary: The Cenozoic Pacific-Australian plate boundary, south of New Zealand. *Journal of Geophysical Research (Solid Earth)*, 108, September 2003. doi: 10.1029/2002JB002041.

E. Lev and B. H. Hager. Anisotropic viscosity in geodynamical flow models - Rayleigh-Taylor instabilities as a test example. *AGU Fall Meeting Abstracts*, page B7, December 2007.

E. Lev and B. H. Hager. Rayleigh-Taylor instabilities with anisotropic lithospheric viscosity. *Geophysical Journal International*, 173:806–814, June 2008a. doi: 10.1111/j.1365-246X.2008.03731.x.

E. Lev and B. H. Hager. Prediction of anisotropy from flow models: A comparison of three methods. *Geochemistry, Geophysics, Geosystems*, 9:7014–7028, July 2008b. doi: 10.1029/2008GC002032.

V. Levin and J. Park. P-SH Conversions in Layered Media with Hexagonally Symmetric Anisotropy: A CookBook. *Pure and Applied Geophysics*, 151:669–697, 1998.

V. Levin, W. Menke, and J. Park. Shear-wave splitting in the Appalacians and the Urals: A case for multilayered anisotropy. *J. Geophys. Res.*, 104:17975–17993, 1999.

V. Levin, D. Droznin, J. Park, and E. Gordeev. Detailed mapping of seismic anisotropy with local shear waves in southeastern Kamchatka. *Geophys. J. Int.*, 158:1009–1023, September 2004.

D. Lizarralde, W. S. Holbrook, S. McGeary, N. L. Bangs, and J. B. Diebold. Crustal construction of a volcanic arc, wide-angle seismic results from the western Alaska Peninsula. *Jour. Geophys. Res.*, 107(8):2164, August 2002. doi: 10.1029/2001JB000230.

M. D. Long and P. G. Silver. The Subduction Zone Flow Field from Seismic Anisotropy: A Global View. *Science*, 319(5861):315–318, 2008. doi: 10.1126/science.1150809.

M. D. Long and R. D. van der Hilst. Upper mantle anisotropy beneath Japan from shear wave splitting. *Phys. Earth Planet. Inter.*, 151:206–222, 2005. doi: 10.1016/j.pepi.2005.03.003.

M. D. Long, B. H. Hager, M. V. de Hoop, and R. D. van der Hilst. Two-dimensional modelling of subduction zone anisotropy with application to southwestern Japan. *Geophysical Journal International*, 170:839–856, May 2007. doi: 10.1111/j.1365-246X.2007.03464.x.

L. E. Malvern. *Introduction to the Mechanics of a Continous Media*. Prentice-Hall, Englewood Cliffs, NJ, 1969.

N. Mandal, C. Chakraborty, and S. K. Samanta. An analysis of anisotropy of rocks containing shape fabric of rigid inclusions. *Jour. of Struct. Geol.*, 22:831–839, 2000.

G. Marquart, H. Schmelling, and O. Čadek. Dynamic models for mantle flow and seismic anisotropy in the North Atlantic region and comparison with observations. *Geochem. Geophys. Geosyst.*, page Q02008, February 2007. doi: 10.1029/2006GC001359.

V. Maupin, E. J. Garnero, T. Lay, and M. J. Fouch. Azimuthal anisotropy in the D" layer beneath the Caribbean. *J. Geophys. Res.*, 110(B9):B08301, August 2005. doi: 10.1029/2004JB003506.

D. McKenzie. Finite deformation during fluid flow. *Geophys. J. Int.*, 58(3):689–715, 1979. doi: 10.1111/j.1365-246X.1979.tb04803.x.

D. McKenzie, J. Jackson, and K. Priestley. Thermal structure of oceanic and continental lithosphere. *Earth Planet. Sci. Lett.*, 233(3-4):337 – 349, 2005. doi: DOI: 10.1016/j.epsl.2005.02.005.

D. E. McNamara, T. J. Owens, P. G Silver, and F. T. Wu. Shear wave anisotropy beneath the Tibetan Plateau. *J. Geophys. Res.*, 99:13655–65, 1994.

D. E. McNamara, W. R. Walter, T. J. Owens, and C. J. Ammon. Upper mantle velocity structure beneath the Tibetan Plateau from Pn travel time tomography. *J. Geophys. Res.*, 102:493–506, 1997.

L. Mehl, B. R. Hacker, G. Hirth, and P. B. Kelemen. Arc-parallel flow within the mantle wedge: Evidence from the accreted Talkeetna arc, south central Alaska. *J. Geophys. Res.*, 108(B8):2375, August 2003. doi: 10.1029/2002JB002233.

J. C. C. Mercier and A Nicolas. Textures and Fabrics of Upper-Mantle Peridotites as Illustrated by Xenoliths from Basalts. *Jour. Petrology*, 16(1):454–487, 1975.

K. Michibayashi and D. Mainprice. The role of pre-existing mechanical anisotropy on shear zone development within oceanic mantle lithosphere: an example from the Oman ophiolite. *Jour. of Petrol.*, 45(2):405–414, 2004.

P. Molnar and P. Tapponnier. Cenozoic Tectonics of Asia: Effects of a Continental Collision. *Science*, 189:419–426, August 1975.

P. Molnar and P. Tapponnier. Active tectonics of Tibet. *J. Geophys. Res.*, 83:5361–5376, November 1978.

P. Molnar, G. A. Houseman, and C. P. Conrad. Rayleigh-Taylor instability and convective thinning of mechanically thickened lithosphere: effects of non-linear viscosity decreasing exponentially with depth and of horizontal shortening of the layer. *Geophysical Journal International*, 133:568–584, June 1998. doi: 10.1046/j.1365-246X.1998.00510.x.

J. Montagner. Where can seismic anisotropy be detected in the Earth's mantle? in boundary layers. *Pure Appl. Geophys.*, 151:223–256, 1998.

J.-P. Montagner. Upper mantle low anisotropy channels below the Pacific Plate. *Earth Planet. Sci. Lett.*, 202:263–274, September 2002.

J.-P. Montagner and H.-C. Nataf. A simple method for inverting the aziumthal anisotropy of surface waves. *J.. Geophys. Res.*, 91(10):511–520, March 1986.

L. Moresi, F. Dufour, and H.-B. Mühlhaus. Mantle Convection Modeling with Viscoelastic/Brittle Lithosphere: Numerical Methodology and Plate Tectonic Modeling. *Pure Appl. Geophys.*, 159:2335–2356, 2002.

L. Moresi, F. Dufour, and H.-B. Mühlhaus. A Lagrangian integration point finite element method for large deformation modeling of viscoelastic geomaterials. *Jour. Computational Physics*, 184:476–497, January 2003.

L. Moresi, S. Quenette, V. Lemiale, C. Mériaux, B. Appelbe, and H.-B. Mühlhaus. Computational approaches to studying non-linear dynamics of the crust and mantle. *Phys. Earth. Planet. Int.*, 163:69–82, August 2007. doi: 10.1016/j.pepi.2007.06.009.

H.-B. Mühlhaus, F. Dufour, L. Moresi, and B. Hobbs. A director theory for visco-elastic folding instabilities in multilayered rock. *Int. Jour. Solids. Struct.*, 39:3675–3691, 2002a.

H.-B. Mühlhaus, L. Moresi, B. Hobbs, and F. Dufour. Large Amplitude Folding in Finely Layered Viscoelastic Rock Structures. *Pure Appl. Geophys.*, 159:2311–2333, 2002b.

H.-B. Mühlhaus, L. Moresi, and M. Cada. Emergent anisotropy and flow alignment in viscous rock. *Pure Appl. Geophys.*, 161:2451–2463, December 2004. doi: 10.1007/s00024-004-2575-5.

J. B. Murphy, C. R. van Staal, and J. D. Keppie. Middle to late Paleozoic Acadian orogeny in the northern Appalachians: A Laramide-style plumemodified orogeny? *Geology*, 27: 653–656, 1999.

M. Nettles and A. M. Dziewonski. Radially anisotropic shear velocity structure of the upper mantle globally and beneath North America. *Journal of Geophysical Research (Solid Earth)*, 113(B12):B2303, February 2008. doi: 10.1029/2006JB004819.

A. A. Ozacar and G. Zandt. Crustal seismic anisotropy in central Tibet: Implications for deformational style and flow in the crust. *Geophys. Res. Lett.*, 31, 2004. doi: 10.1029/2004GL021096.

Simon M. Peacock and Kelin Wang. Seismic Consequences of Warm Versus Cool Subduction Metamorphism: Examples from Southwest and Northeast Japan. *Science*, 286(5441):937–939, 1999. doi: 10.1126/science.286.5441.937.

Z. Peng and Y. Ben-Zion. Systematic analysis of crustal anisotropy along the Karadere-Düzce branch of the North Anatolian fault. *Geophys. J. Int.*, 159:253–274, October 2004.

L. Pouilloux, E. Kaminski, and S. Labrosse. Anisotropic rheology of a cubic medium and the implications for geologic materials. *Geophys. Jour. Int.*, 170:876–885, 2007. doi: 10.1111/j.1365-246X.2007.03461.x.

J. Reinecker, O. Heidbach, M. Tingay, , P. Connolly, and B. Müller. The 2004 release of the World Stress Map, 2004. URL `www.world-stress-map.org`.

J. Revenaugh and T. H. Jordan. Mantle layering from ScS reverberations. 3. The upper mantle. *Jour. Geophys. Res.*, 96:19781–19810, November 1991. doi: 10.1029/91JB01487.

A. Reymer and G. Schubert. Phanerozoic Addition Rates to the Continental Crust and Crustal Growth. *Tectonics*, 3:63–77, 1984. doi: 10.1029/TC003i001p00063.

N. M. Ribe. On the relation between seismic anisotropy and finite strain. *J. Geophys. Res.*, 97:8737–8747, June 1992.

F. M. Richter and S. F. Daly. Convection models having a multiplicy of large horizontal scales. *Jour. Geophys. Res.*, 83:4951–4956, 1978.

M. R. Riedel and S.-I. Karato. Grain-size evolution in subducted oceanic lithosphere associated with the olivine-spinel transformation and its effects on rheology. *Earth. Planet. Sci. Lett.*, 148:27–43, February 1997. doi: 10.1016/S0012-821X(97)00016-2.

P. Robinson. Acadian magmatism and metamorphism in New England: A product of mantlelithosphere delamination in front of an east-dipping subduction zone? *Geological Society of America Abstracts with Programs*, 25(6):Abs. 179, 1993.

L. Royden, B. C. Burchfiel, R. W. King, Z. Chen, F. Shen, and Y. Liu. Surface deformation and lower crustal flow in eastern Tibet. *Science*, 276:788–790, August 1997.

G. Rumpker and P. G. Silver. Apparent shear-wave splitting parameters in the presence of vertically varying anisotropy. *Geophys. J. Int.*, 135:790–800, April 1998.

M. Saito and Y. Abe. Consequences of anisotropic viscosity in the Earth's mantle (in Japanese, with English abstrat). *Zisin*, 37:237–245, 1984.

J. Saleeby and Z. Forster. Topographic response to mantle lithosphere removal in the southern Sierra Nevada region, California. *Geology*, 32:245–248, 2004. doi: 10.1130/G19958.1.

M. K. Savage. Seismic anisotropy and mantle deformation: What have we learned from shear wave splitting? *Reviews of Geophysics*, 37:65–106, 1999.

M. K. Savage and P. G. Silver. Mantle deformation and tectonics: constraints from seismic anisotropy in the western United States. *Phys. Earth Planet. Inter.*, 78:207–227, July 1993.

H. Schmeling. Numerical models on the influence of partial melt on elastic, anelastic and electric properties of rocks. Part I: elasticity and anelasticity. *Physics of the Earth and Planetary Interiors*, 41:34–57, December 1985. doi: 10.1016/0031-9201(85)90100-1.

G. Schubert, D. L. Turcotte, and P. Olson. *Mantle Convection in the Earth and Planets*. pp. 956, ISBN 052135367X, Cambridge, UK: Cambridge University Press, September, September 2001. ISBN 052135367X.

N. M. Shapiro, M. H. Ritzwoller, P. Molnar, and V. Levin. Thinning and Flow of Tibetan Crust Constrained bySeismic Anisotropy. *Science*, 305:233–236, July 2004.

P. G. Silver and W. W. Chan. Shear wave splitting and subcontinental mantle deformation. *J. Geophys. Res.*, 96(15):16429–16454, September 1991.

P. G. Silver and M. K. Savage. The interpretation of shear-wave splitting parameters in the presence of two anisotropic layers. *Geophys. J. Int.*, 119:949–963, 1994.

F. J. Simons and R. D. van der Hilst. Seismic and mechanical anisotropy and the past and present deformation of the Australian lithosphere. *Earth Planet. Sci. Lett.*, 211:271–286, June 2003.

F. Simpson. Intensity and direction of lattice-preferred orientation of olivine: Are electrical and seismic anisotropies of the Australian mantle reconcilable? *Earth Planet. Sci. Lett.*, 203:535–547, October 2002.

P. Skemer, I. Katayama, Z. Jiang, and S. is. Karato. The misorientation index: Development of a new method for calculating the strength of lattice-preferred orientation. *Tectonophysics*, 411:157–167, December 2005.

D. B. Smith, M. H. Ritzwoller, and N. M. Shapiro. Stratification of anisotropy in the Pacific upper mantle. *Jour. Geophys. Res.*, 109:11309–11330, November 2004. doi: 10.1029/2004JB003200.

S. Sol, A. Meltzer, B. Zurek, P. Zeitler, and X. Zhang. Clockwise Rotation of Upper-Mantle Strain and Crust-Mantle Coupling Beneath the Eastern Syntaxis Tibet. *Eos Trans., AGU Fall Meeting Abstracts*, 86(52):T41A–1280, December 2005.

C. Stein, J. Schmalzl, and U. Hansen. The effect of rheological parameters on plate behaviour in a self-consistent model of mantle convection. *Physics of the Earth and Planetary Interiors*, 142:225–255, May 2004.

A. Taira, S. Saito, K. Aoike, S. Morita, Tokuyama H., K. Suyehiro, N. Takahashi, M. Shinohara, S. Kiyokawa, J. Naka, and A. Klaus. Nature and growth rate of the Northern IzuBonin (Ogasawara) arc crust and their implications for continental crust formation. *Island Arc*, 7:395–407, 2004.

T. Takenami, S. I. Sacks, and A. Hasegawa. Attenuation structure beneath the volcanic front in northeastern Japan from broad-band seiseismograms. *Phys. Earth Planet. Inter.*, 121:339–357, 2000.

C. B. Till, L. T. Elkins-Tanton, and K. M. Fischer. Low-extent melt at the lithosphere-asthenosphere boundary, eastern North America. *Geophys. Geochem. Geosys.*, Submitted, 2009.

A. Tommasi. Forward modeling of the development of seismic anisotropy in the upper mantle. *Earth Planet. Sci. Lett.*, 160:1–2, July 1998.

A. Tommasi, D. Mainprice, G. Canova, and Y. Chastel. Viscoplastic self-consistent and equilibrium-based modeling of olivine lattice preferred orientations: Implications for the upper mantle seismic anisotropy. *J. Geophys. Res.*, 105:7893–7908, 2000.

Y. Torii and S. Yoshioka. Physical conditions producing slab stagnation: Constraints of the Clapeyron slope, mantle viscosity, trench retreat, and dip angles. *Tectonophysics*, 445: 200–209, December 2007. doi: 10.1016/j.tecto.2007.08.003.

S. H. Treagus. Viscous anisotropy of two-phase composites, and applications to rocks and structures. *Tectonophysics*, 372:121–133, September 2003.

D. L. Turcotte and G. Schubert. *Geodynamics*. Cambridge University Press, England/New York, Cambridge University Press, 2002, 456 p., 2002.

J. van Hunen, S Zhong, N. M. Shapiro, and M. H. Ritzwoller. New evidence for dislocation creep from 3-D geodynamic modeling of the Pacific upper mantle structure. *Earth. Planet. Sci. Lett.*, 238:146–155, August 2005.

P. van Keken, B. Kiefer, and S. Peacock. High resolution models of subduction zones: Implications for mineral dehydration reactions and the transport of water into the deep mantle. *Geochem., Geophys., Geosyst.*, 3(10):1056, 2002. doi: 10.1029/2001GC000256.

P. E. van Keken. The structure and dynamics of the mantle wedge. *Earth Planet. Sci. Lett.*, 215:323–338, October 2003.

P. E. van Keken, C. Currie, King S. D., M. D. Behn, A. Cagnioncle, J. He, R. F. Katz, S. Lin, E. M. Parmentier, M. Spiegelman, and K. Wang. A community benchmark for subduction zone modeling. *Phys.Earth Planet. Int.*, 171(1-4):187–197, 2008. doi: 10.1016/j.pepi.2008.04.015.

A. Vauchez, G. Barruol, and A. Tommasi. Why do continents break-up parallel to ancient orogenic belts? *Terra Nova*, 6:62–66, 1997.

A. Vauchez, A. Tomassi, and G. Barroul. Rheological heterogeneity, mechanical anisotropy and deformation of the continental lithosphere. *Tectonophysics*, 296:61–86, August 1998.

J. Wahr and D. Han. Predictions of Crustal Deformation Caused by Changing Polar Ice on a Viscoelastic Earth. *Surveys in Geophysics*, 18:303–312, 1997.

E. Wang and B. C. Burchfiel. Interpretations of Cenozoic tectonics in the right-lateral accomodation zone between the Ailo Shan shear zone and the Eastern Hymalayan syntaxis. *Int. Geol. Rev.*, 39:191–219, 1997.

E. Wang, B. C Burchfiel, L. H. Royden, C. Liangzhong, C. Jishen, L. Wenxin, and C. Zhiliang. Late Cenozoic Xianshuihe-Xiaojiang, Red River and Dali Fault Systems of Southwestern Sichuan and Central Yunnan, China. *Geological Society of America - Special Paper*, 327:188 pp., 1998.

J. M. Warren and G. Hirth. Grain size sensitive deformation mechanisms in naturally deformed peridotites. *Earth Planet. Sci. Lett.*, 248(1-2):438–450, 2006.

J. M. Warren, G. Hirth, and P. B. Kelemen. Evolution of olivine lattice preferred orientation during simple shear in the mantle. *Earth and Planetary Science Letters*, 272:501–512, August 2008. doi: 10.1016/j.epsl.2008.03.063.

R. Weijermars. Progressive deformation in anisotropic rocks. *Jour. of Struct. Geol.*, 14: 723–742, 1992.

T. Weiss, S. Siegesmund, W. Rabbel, T. Bohlen, and M. Pohl. Seismic Velocities and Anisotropy of the Lower Continental Crust: A Review. *Pure and Applied Geophysics*, 156:97–122, 1999.

A. S. Wendt, D. Mainprice, E. Rutter, and R. Wirth. A joint study of experimental deformation and experimentally induced microstructures of pretextured peridotites. *Jour. Geophys. Res.*, 103:18205–18222, August 1998. doi: 10.1029/98JB01555.

H.-R. Wenk, S. Speziale, A. K. McNamara, and E. J. Garnero. Modeling lower mantle anisotropy development in a subducting slab. *Earth. Planet. Sci.Lett.*, 245:302–314, May 2006. doi: 10.1016/j.epsl.2006.02.028.

T. Wenzel, D. F. Mertz, R. Oberhänsli, T. Becker, and P. R. Renne. Age, geodynamic setting, and mantle enrichment processes of a K-rich intrusion from the Meissen massif (northern Bohemian massif) and implications for related occurrences from the mid-European Hercynian. *International Journal of Earth Sciences*, 86:556–570, 1997.

J. A. Whitehead. Buoyancy-driven instabilities of low-viscosity zones as models of magma-rich zones. *Jour. Geophys. Res.*, 91:9303–9314, August 1986.

D. A. Wiens and J. A. Conder. The Seismic Structure and Dynamics of the Mantle Wedge. *Ann. Rev. Earth. Planet. Sci.*, 36:421–455, May 2008. doi: 10.1146/annurev.earth.33.092203.122633.

F.-Y. Wu, J.-Q. Lin, S. A. Wilde, X. Zhang, and J.-H. Yang. Nature and significance of the Early Cretaceous giant igneous event in eastern China. *Earth and Planetary Science Letters*, 233:103–119, April 2005. doi: 10.1016/j.epsl.2005.02.019.

Y. Yang and D. W. Forsyth. Rayleigh wave phase velocities, small-scale convection, and azimuthal anisotropy beneath southern California. *Jour. Geophys. Res.*, 111(B10):B07306, July 2006. doi: 10.1029/2005JB004180.

H. Yao, R. D. van der Hilst, and M. V. de Hoop. Surface-wave array tomography in SE Tibet from ambient seismic noise and two-station analysis: I - Phase velocity maps. *Geophys. J. Int.*, 166:732–744, 2006. doi: 10.1111/j.1365-246X.2006.03028.x.

P. Z. Zhang, Z. Shen, M. Wang, Gan W., R. Burgmann, P. Molnar, Z. Niu, J. Sun, J. Wu, H. Sun, and X. You. Continuous deformation of the Tibetan Plateau from global positioning data. *Geology*, 32:809–812, 2004. doi: 10.1130/G20554.1.

Z. Zhang and S. I. Karato. Lattice prefered orientation in olivine aggregates deformed in simple shear. *Nature*, 375:774–777, 1995.

Z. Zhang, S. I. Karato, U. H. Gerald, and Y. Zhou. Simple shear deformation of olivine aggregates, Tectonophysics. *Tectonophysics*, 316:133–152, 2000.